Magnetoresistance Effects in Multilayer Graphene as Grown on Nickel

by

Srikrishna Chanakya Bodepudi

A thesis submitted in partial fulfillment of the requirements for the degree of

Doctor of Philosophy

in

Microsystems and Nanodevices

Department of Electrical and Computer Engineering

University of Alberta

Abstract

Magnetoresistance (MR), the change in electrical resistance of a solid-state system due to an external magnetic field, is a key effect in condensed matter physics, both for fundamental understanding of charge transport phenomena, as well as immense commercial implications. Artificial layered structures often exhibit strong magnetoresistance (MR) effects that are exploited in various data storage and magnetic field sensing technologies. Graphite is a naturally occurring layered structure in which single graphitic layers (or "graphene") are stacked up on each other. Magnetoresistance (MR) in graphitic systems (single to few layers of graphene and bulk graphite) has drawn significant attention in recent years. It has been theoretically predicted that multilayer graphene (MLG) on Ni can potentially exhibit large magnetoresistance values due to spin filtering effect. However, experimental work in this area is rare. The purpose of this work is to explore various magnetoresistance effects in MLG/Ni systems.

Multilayer graphene (MLG) stacks with various thicknesses have been grown on polycrystalline Ni substrates using a standard chemical vapor deposition (CVD) recipe. These samples exhibit a large, negative MR effect in current-perpendicular-to-plane (CPP) geometry with the magnetic field normal to the plane. A negative magnetoresistance effect ~ 10^4% has been observed, which persists even at room temperature. The observed magnetoresistance is extremely high as compared to other known materials systems for similar temperature and field range. This effect is correlated with the shape of the 2*D* peak as well as with the absence of *D* peak in the Raman spectrum. The observed data is qualitatively consistent with the

"interlayer magnetoresistance" (ILMR) mechanism in which interlayer charge transfer occurs between the zero mode Landau levels of weakly coupled graphene layers. To further understand ILMR effect, angle and thickness dependent studies have been performed in as-grown MLG on Ni samples.

Angular dependences of ILMR effect in as-grown MLG agree well with theory. However, the angular response is sharper than expected and is related to the additional sources of positive MR present in the system. In addition, the ILMR effect persists and becomes stronger as thickness of MLG is increased. Interestingly, for larger thickness samples, magnitude of the MR effect is relatively insensitive to temperature. To further verify this, CPP MR measurements have been performed in as-grown MLG samples with different thicknesses. In the next stage of this thesis, as-grown MLG samples have been tested in spin valve configuration in order to investigate spin-related magnetoresistance effects and its implications for graphene spin filters. However these devices only show weak localization and ILMR but no spin filtering.

Based on above observations, we are planning to explore the following subprojects in future: (1) MR effects in as-grown MLG on cobalt (Co), (2) MR effects in functionalized graphene/Ni (111) and exploring spin filtering effect in this system, and (3) MR effects in transferred MLG on flexible substrates.

Due to large MR value and its persistence at room temperature, this ILMR effect in as-grown MLG samples is expected to have commercial implications and encourage further research on MLG physics and MLG growth mechanisms on

ferromagnetic substrate. Further, intrinsic compatibility of MLG with flexible electronics and sensorics makes ILMR an exciting platform for future magnetic sensing and data storage technologies.

Preface

This thesis work is performed in Electrical and Computer Engineering Research Facilities (ECERF) and Nanofab facilities located in University of Alberta, and also in on-campus National Institute for Nanotechnology (NINT). In Chapter 1, Figures 1.1 (c), 1.4, 1.6, 1,7 are used with permission from applicable sources. Parts of Chapters 2 and 3 in this thesis have been published in *Nano Letters* [S. C. Bodepudi, A. P. Singh, and S. Pramanik, Nano Lett., Apr. 2014] and *Electronics* (invited paper in *Carbon Nanoelectronics*) [S. C. Bodepudi, A. P. Singh, and S. Pramanik, Electronics, vol. 2, no. 3, pp. 315–331, Sep. 2013]. I was responsible for the data collection, analysis as well as the manuscript preparation. The second co-author, A.P.Singh, was involved in data collection and manuscript edits. Sandipan Pramanik was the supervisory author and was involved with concept formation and manuscript composition.

Results described in Chapters 4 and 5 have been submitted for publication and currently under review [S. C. Bodepudi, W. Xiao, S. Pramanik, Submitted to J. Appl. Phys. (JR15-6621R) and S. C. Bodepudi, W. Xiao, S. Pramanik, Submitted to Carbon (CARBON-D-15-02297)]. I was responsible for the data collection, analysis as well as the majority of manuscript composition. W. Xiao was assisted in concept formation and manuscript edits. Sandipan Pramanik was the supervisory author and was involved with concept formation and manuscript composition. Parts of Chapter 6 have been published in a conference proceeding [S. C. Bodepudi, Abhay Singh, and S. Pramanik, in *Proceedings of the 14th IEEE International Conference on Nanotechnology*, Toronto, 2014, vol. 14th IEEE-Nano]. I was responsible for the majority of data collection and manuscript preparation. A.P.Singh was assisted in data collection and manuscript edits. Sandipan Pramanik was the supervisory author and was involved with concept formation and manuscript composition. Corey Ma was assisted in sample preparation and data collection for MLG on flexible substrate samples presented in Figure 7.3 (Chapter 7). LabVIEW data acquisition used for magnetoresistance measurements performed in this thesis is designed by myself.

Table of Contents

1 INTRODUCTION.....1
1.1 Graphene Basics..... 4
1.2 Graphene in Magnetic Field..... 5
1.3 Multilayer Graphene (MLG) and CVD Growth 8
1.4 Magnetoresistance in Graphene Based Systems..... 11
1.4.1 Weak Localization 12
1.4.2 Classical and Quantum Linear MR..... 13
1.4.3 Field Induced Metal-Insulator Transition 15
1.4.4 Interlayer Magnetoresistance (ILMR) 15
1.4.5 Bright's Model 16
1.5 Graphene Synthesis..... 16
1.6 Raman Spectroscopy of Graphitic Systems..... 18
1.7 Metal-Graphene Interface 21
1.8 Motivation of This Thesis..... 22
1.9 Summary of Contributions..... 23
1.10 Future Directions 24
2 CVD GROWTH OF MULTILAYER GRAPHENE (MLG) AND CHARACTERIZATION 26
2.1 INTRODUCTION 26
2.1.1 CVD Growth of Multilayer Graphene (MLG) on Ni..... 28
2.1.2 Oxygen Plasma Etching of MLG and Device Patterning 29
2.1.3 Transfer of MLG on SiO_2/Si..... 30
2.2 Raman Characterization of Synthesized MLG 33

2.2.1 Raman Spectra of MLG on Ni 35

2.2.2 Transferred MLG on SiO_2/Si 38

2.2.3 CVD-grown MLG on Cu 40

3 MAGNETORESISTANCE (MR) MEASUREMENTS ON CVD-GROWN MLG 43

3.1 CPP-MR of CVD-grown MLG on Ni 44

3.1.1 Case 1: CPP-MR of Thicker MLG (~200 nm) Showing Symmetric Raman 2*D* Band and no *D* Band 44

3.1.2 Case 2: Thicker MLG (~ 200 nm) Showing Distorted Raman 2*D* Band and no *D* Band 50

3.1.3 Case 3: Thinner MLG (~15 – 20 nm) Showing Presence of Raman *D* Band and Symmetric 2*D* Band 50

3.2 Anisotropic Magnetoresistance (AMR) of Ni Foil 51

3.3 Ag/MLG Contact Resistance 52

3.4 CPP-MR of CVD-Grown MLG on Cu 54

3.5 Discussion 55

3.6 Conclusion 65

4 ANGLE DEPENDENT INTERLAYER MAGNETORESISTANCE (ILMR) IN CVD-GROWN MLG 67

4.1 Angle Dependent Interlayer Magnetoresistance (ILMR) 70

4.2 Device Fabrication and Characterization 74

4.3 Angle Dependent CPP MR in CVD grown MLG on Ni 79

4.4 In-plane Electrical Characterization of Transferred MLG 85

4.4.1 Sheet Resistance and Contact Resistance Measurements. 87

4.4.2 In-plane MR Characterization of Transferred MLG – Weak Localization 89

4.4.3 Shubnikov-deHaas Oscillations in the in-plane MR Measurements. ……..90

4.5 Conclusion 92

5 THICKNESS DEPENDENT INTERLAYER MAGNETORESISTANCE (ILMR) IN CVD GROWN MLG 95

5.1 Fabrication and Characterization 95

5.2 Thickness Dependent CPP MR in CVD grown MLG on Ni 97

5.3 Discussion 103

5.4 Conclusion 106

6 CPP MR STUDIES ON NI/MLG/NI SPIN VALVES 107

6.1 Fabrication and Characterization 109

6.2 CPP MR Measurements 110

6.3 Discussion and Conclusion 112

7 RECOMMENDATIONS FOR THE FUTURE 117

7.1 Subproject 1: CPP-MR Effects in As-Grown MLG on Cobalt..... 117

7.1.1 Preliminary Results 118

7.1.2 Proposed Methodology 118

7.2 Subproject 2: MR in Functionalized MLG/Ni Interface and Studies on Spin Filtering 119

7.2.1 Proposed Methodology 119

7.3 Subproject 3: MR effects in MLG Transferred on Flexible Substrates .. 121

7.3.1 Preliminary Results 122

7.3.2 Proposed Methodology 122

References 124

List of Figures

Figure 1.1 Honeycomb lattice and band structure of graphene. (a) Interpenetrating triangular sub lattices (A, B) of graphene are represented by dashed and solid lines respectively; (b) σ bonds between carbon atoms in the hexagonal arrangement and π bonds between $2p_z$ orbitals oriented perpendicular to the graphene plane; (c) Zero band gap and linear energy dispersion of graphene close to the Dirac points (adopted from ref. [40]). 5

Figure 1.2 A 2D electron gas material with parabolic energy dispersion, in presence of a uniform and static magnetic field applied normal to the plane. (a) Electron in cyclotron orbital, (b) Electrons in cyclotron orbitals with centre at $-y_0$ and quantized radii, (c) Energy levels (Landau levels) in presence of magnetic field. Note that Landau levels are equally spaced and the spacing between neighbouring Landau levels is $\hbar\omega_c$ (adopted from [45]). 9

Figure 1.3 Density of states (DOS) of graphene for $B = 0$ and for $B \neq 0$. For $B \neq 0$, the linear DOS of graphene condenses into quantized, unequally spaced Landau levels (LLs). A schematic description is shown above. The zero mode Landau level (LL_0) is located at Fermi level (E_F), which coincides with the Dirac point. 10

Figure 1.4 Stacking sequence and electronic bands of MLG. (a) and (b) panels show Bernal and rhombohedral stacking sequence respectively (taken from ref.[46]). (c) Electronic bands of trilayer graphene with Bernal stacking. (d) Electronic bands of trilayer graphene with rhombohedral stacking (taken from ref. [44]). 11

Figure 1.5 Weak localization effect. Diffusion paths of a conduction electron in both directions (full and dashed lines) between scattering centres (impurities or defects). Weak localization occurs when a conduction electron finishes a closed trajectory and reaches the origin or the starting point (adopted from [5]). 13

Figure 1.6 Graphene growth on Ni substrate by CVD. Medium cooling rate during carbon segregation provides uniform and large area MLG (taken from ref.[30]). 18

Figure 1.7 $2D$ band of Raman spectra taken with laser energy of 2.41 eV for (a) 1-layer, (b) 2-layer, (c) 3-layer, (d) 4-layer and (e) HOPG (taken from ref.[34]). 20

Figure 2.1 Schematic description of the fabrication process. The CVD growth of MLG on Ni; oxygen plasma etching of graphene on the bottom surface; transfer of MLG on SiO_2/Si are depicted in the schematic. Typical XRD spectrum of the polycrystalline Ni substrate used in this work is presented in the *inset*..... 30
Figure 2.2 Optical microscope images of CVD-grown MLG on Ni. (a) Thick (~ 200 nm) as-grown MLG on 25 μm thick Ni foil. (b) Thinner (15 – 20 nm) as-grown MLG on ~ 600 nm Ni thin film. 31
Figure 2.3 Atomic Force Microscopic (AFM) image of CVD-grown MLG-on-Ni. 31
Figure 2.4 Thicker MLG transferred on SiO_2/Si. Step height measurement of transferred MLG on SiO_2/Si using profilometer (Alphastep-200). Average thickness of transferred MLG is ~ 200 nm. *Insets* show optical image of transferred MLG on SiO_2/Si..... 33
Figure 2.5 Thinner MLG transferred on SiO_2/Si. Step height measurement of transferred MLG on SiO_2/Si using Atomic Force Microscope (AFM). Average thickness of transferred MLG is ~ 15 – 20 nm. 34
Figure 2.6 Raman spectrum of HOPG (SPI supplies, SPI-1 grade). The Raman 2D (2718 cm^{-1}) is asymmetric and consists of two shifted Lorentzian components (red and green lines in *inset*). The higher intensity component (red line) appears at higher frequency side..... 35
Figure 2.7 Raman Spectrum of CVD-grown MLG on Ni Sample in Case1. The Raman spectra have been taken from three representative areas of the MLG on Ni sample. The 2*D* bands do not show HOPG-like "shoulder" peak or any significant splitting. The *D* peak is not present anywhere. The top Raman spectrum (black line) is most commonly observed, with few occurrences of the other two (blue and red). 36
Figure 2.8 Raman spectra of CVD-grown MLG on Ni Samples in Case 2. MLG thickness is ~ 200 nm (Figure (a)) and ~ 100 nm (Figure (b)). (a) Raman spectrum of HOPG-like sample CVD-grown on Ni. The *2D* band in the Raman spectrum shows a shoulder peak (*inset*). (b) Raman characteristics of commercial MLG/Ni

samples (from Graphene Supermarket). The 2*D* band in the Raman spectra shows pronounced splitting..... 39
Figure 2.9 Raman Spectrum of CVD-grown MLG (~ 15 – 20 nm) on Ni Thin Film (~ 600 nm) Sample in Case 3. A clear *D* peak can be observed at ~ 1350 cm^{-1}, which was not present in thicker specimens..... 40
Figure 2.10 Raman Spectra of MLG Transferred on SiO_2/Si. A HOPG-type distorted 2*D* band is observed..... 42
Figure 2.11 Raman Characteristics of CVD-grown MLG (~ 8 layer) on Copper (ACS Materials). The 2*D* peak is symmetric and can be fitted with a single Lorentzian (*inset*). The bottom scan (red line) is taken from the grain boundary (GB) region, which shows a significant defect (*D*) peak at ~1360 cm^{-1}..... 42
Figure 3.1 Device Schematic and Magnetoresistance (MR) Measurement Setup. (a) Measurement geometry. The MLG (*xy* plane) is grown on the bottom Ni substrate by CVD. (b) Sample is mounted on the sample stick for low temperature measurements. Magnetic field is generated by the electromagnet as shown in figure. 45
Figure 3.2 Magnetic Field Dependence of CPP Resistance (R_{zz}) in the Temperature Range 10 – 300*K* for MLG/Ni Samples in Case 1. For each temperature two orientations of the magnetic field have been considered: (i) $B \parallel I$ ($\theta = 0$) and (ii) $B \perp I$ ($\theta = \pi/2$). Giant negative magnetoresistance is observed in $B \parallel I$ configuration whereas in $B \perp I$ geometry weak positive magnetoresistance is recorded (insets), which becomes less pronounced at higher temperatures. Both scan directions are shown in each plot, indicating absence of any hysteresis. Each resistance value is the average of 50 readings. For $B \parallel I$, minimum resistance (occurring at high fields) is ~2 – 4 Ω as shown later in Figure 3.3. In all cases, bias current is 1mA dc. 47
Figure 3.3 CPP Charge Transport Characteristics of Samples in Case 1. R_{zz} (T) at zero field and high field (11kG) indicate insulating behavior and absence of any field induced metal-insulator transition. 48
Figure 3.4 $I - V$ Characteristics of Samples in Case 1. (a) $I - V$ characteristics of MLG/Ni samples at four different temperatures, indicating bias independence of

the CPP-MR in ±1 mV range. For zero magnetic field, current is ~ few μA at 1mV bias. (b) A zoomed-in image of the zero-field $I - V$ data is presented. 49
Figure 3.5 CPP MR of MLG Transferred on Au and Ni Electrodes. (a) CPP-MR of MLG (Ni-grown) transferred on Au contact and (b) CPP-MR of MLG (Ni-grown) transferred on Ni contact. Unlike as-grown MLG, the transferred MLG exhibits shoulder peak in Raman 2*D* band (Figure 2.10). 49
Figure 3.6 CPP-MR of samples in Case 2. (a) R_{zz} vs. B in the $B \parallel I$ geometry. A metal-insulator transition is observed near ~1kG. (b) CPP-MR of commercial MLG/Ni samples (from Graphene Supermarket). 51
Figure 3.7 Charge Transport Characteristics of Samples in Case 3. (a) CPP-MR of thinner (~15-20 nm) MLG samples. (b) Metallic temperature dependence of CPP resistance (R_{zz})..... 51
Figure 3.8 AMR of Ni Foil Substrate. (a)-(d) Typical AMR response of Ni foil for the temperature range 10–200 *K*. Triangular symbols indicate scans in $B \| I$ geometry and circular symbols indicate scans in $B \perp I$ geometry. 53
Figure 3.9 In-plane Measurements. (a) Four point measurement geometry and digital image of the device. (b) In-plane four-point MR of transferred (Ni-grown) MLG. (c) Two-point and four-point in-plane resistance at zero magnetic field. Contact resistance has been estimated as half of the difference between two-point and four-point data. (d) In-plane two-point resistance vs. channel length (i.e. distance between the two contacts). Closed symbols and solid line fits correspond to zero magnetic field case whereas open symbols and dashed line fits correspond to the case when 11kG out-of-plane magnetic field is present. The linear trends extrapolated to zero channel length limit provide an estimate of the Ag paste/MLG contact resistance. 55
Figure 3.10 Charge Transport Characteristics of MLG/copper Sample. (a) CPP-MR of MLG/copper showing weak localization at low field in the temperature range 10 K– 50 K, which disappears at higher temperature. (b) Linear current-voltage (*I-V*) characteristics indicate bias independence of observed negative MR. 57

Figure 3.11 Inverse of CPP resistance (R_{zz}) as a function of out-of-plane magnetic field (B) in the vicinity of the switching field of ~ 2 kG. A linear trend is observed at all temperatures. 64
Figure 3.12 Switching magnetic field as a function of temperature. 65
Figure 4.1 Schematic description of the ILMR effect. (a) Applied magnetic field (B) = 0 and an out of plane electrical bias drives the interlayer current. Weak interlayer coupling ensures that Dirac cone dispersion is preserved for individual layers. Carrier transport occurs via tunneling between the states in the vicinity of the (quasi) Fermi level E_F (or Dirac point). Due to the dearth of available states (and hence available carriers) and weak interlayer coupling, interlayer current is weak. (b) Out of plane magnetic field is applied ($B \neq 0$) and a zero mode Landau level ($n = 0$) forms at the Dirac point, which coincides with the quasi Fermi level E_F. Each Landau level has a finite broadening due to disorder and thermal effects. Density of states (DOS) and carrier concentration of zero mode is proportional to B. Since interlayer transport occurs via zero mode, large interlayer current is observed due to large number of carriers participating from each layer. (c) Inter Landau Level mixing effect (dotted lines), which is dominant when inter Landau level separation is small (such as small B, large T etc.). Dashed lines show typical ILMR mechanism, without any mixing. In this case E_F is located away from the Dirac point. 72
Figure 4.2 Device schematic and optical images of as-grown and transferred MLG. (a) Device structure and measurement geometry. The "tilt angle" θ is measured with respect to the out of plane direction. MLG grown on bottom Ni substrate consists of a "defective" region at the interface and a "defect-free" region at the top. The defect free region consists of weakly coupled graphene layers. Silver paste contact is placed at the centre of the top MLG surface to achieve uniform current distribution. (b) (main image) Optical micrograph of as-grown MLG on Ni. Top left inset shows the transferred MLG on SiO_2/Si. The histogram in the main image shows typical thickness distribution in the wrinkle free areas of transferred MLG. Average MLG thickness in the wrinkle free area is ~ 60 nm. In the optical images,

the dark lines represent wrinkles (or regions of larger thickness) in the MLG layer. 77

Figure 4.3 Raman studies on as-grown and transferred MLG. (a) Raman spectra from three representative areas of as-grown MLG on Ni (i.e. *before* transfer). The top plot (blue) is most commonly observed (~ 80% area). The 2*D* band is symmetric in all cases and can be fitted with single Lorentzian (*insets*). (b) Raman spectrum taken from the Ni/MLG interface after removing the Ni. Clear *D* peak is present, which confirms defective nature of this region. The inset shows schematic of graphene growth on Ni. Regions marked "A" (near Ni/MLG interface) are truncated by Ni grain boundaries and significant interfacial hybridization occurs in this region, which are the origins of defects in this region. But regions marked "B" (away from Ni/MLG interface) have continuous graphene layers covering the underlying layers. These layers are relatively defect free. (c) Typical Raman spectra of MLG (top layers) transferred on SiO_2/Si, from three representative regions. In all cases either splitting or shoulder in 2*D* band has been observed. No defect (*D*) peak has been observed in both as-grown and transferred MLG. Since the penetration depth of the Raman laser (2.33 eV) is ~ 50nm and average sample thickness is ~ 60 nm, the Raman signal originates from the "defect free" region as described in Figure 4.3(a). 80

Figure 4.4 CPP MR characterization for out of plane ($\theta = 0^o, 180^o$) and in-plane ($\theta = 90^o, 270^o$) magnetic fields**.** (a) Temperature (T) dependence of CPP resistance $R_{zz}(T)$ in MLG/Ni samples at zero magnetic field and at 8kG (out of plane) over the temperature range 15 – 270 K. Insulating behaviour is observed at both temperatures, along with a magnetoresistance effect. (b) Normalized CPP resistance ($R_{zz}(B)/R_{zz}(B = 0)$) at various measurement temperatures for $\theta = 0^o, 180^o$. A negative MR effect is observed. This effect weakens and MR curves broaden as temperature is increased. Critical field B_{cr} is the field value at which device resistance starts to drop significantly. (c) Normalized MR ($R_{zz}(B)/R_{zz}(B = 0)$) at various measurement temperatures for $\theta = 90^o, 270^o$. A positive MR is observed in this case. As before, MR effect weakens and MR characteristics broaden as

temperature is increased. (d) Inverse of normalized CPP resistance ($R_{zz}(B)/R_{zz}(B = 0))^{-1}$ as a function of out-of-plane magnetic field (B) in the range where negative MR is most prominent. Clear linear fit is observed in all cases. The inset shows variation of B_{cr} as a function of T^2. A clear linear fit is observed..... 82

Figure 4.5 Angle dependence of CPP MR. (a), (b) Normalized CPP resistance ($R_{zz}(B)/R_{zz}(B = 0)$) of as-grown MLG on Ni at various orientations of the magnetic field (θ) at two different temperatures (15K and 220K). The negative MR gradually decreases as tilt angle θ is increased. (c) Critical field (B_{cr}) as a function of θ at 15K and 220K. Critical field is higher at higher temperature and increases with the tilt angle..... 86

Figure 4.6 Angular dependence of CPP resistance $R_{zz}(\theta)$ at various field strengths. (a), (b) Data at 15K and 220K respectively. Three different field values are chosen, which are higher than B_{cr}. For a given field strength (B), device resistance at angle θ is normalized by the resistance value at $\theta = 0^o$, which also coincides with the resistance value at $\theta = 180^o$. As the tilt angle is increased with respect to 0^o (or 180^o), device resistance increases and ultimately saturates for $\theta > 10^o$. (c) Experimental data (black line with data points) shows sharper angular dependence compared to theory (red, smooth curve). The data corresponds to $B = 5.7$ kG. ... 88

Figure 4.7 Electrical characterization of MLG transferred on SiO_2/Si. (a), (i) Typical van der Pauw geometry and (ii) TLM geometry. (b) TLM data, from which Ag/MLG contact resistance (R_c) and MLG sheet resistance (R_s) have been extracted..... 90

Figure 4.8 In-plane MR characterizations. (a) In-plane MR from MLG (top surface), transferred on SiO_2/Si, at various temperatures. Positive MR has been observed at all temperatures. No negative MR due to weak localization effect has been observed near $B = 0$. (b) In-plane MR from 8-layer transferred graphene (Cu-grown). Clear negative MR due to weak localization effect has been observed near $B = 0$. As expected, this effect disappears as temperature is increased. (c) Typical Raman data from 8-layer, Cu-grown graphene. Defect induced Raman peak (*D*-

peak) is present, which originates from the grain boundaries. Weak localization effect observed in (b) is due to these grain boundaries. 91

Figure 4.9 Shubnikov-deHaas oscillations in in-plane MR of Ni-grown MLG transferred on SiO_2/Si. (a) Typical MR plot at 12K (black line) and smooth monotonic background (red line). (b) MR at various temperatures after removing the smooth background. MR oscillations have been observed, which increase in amplitude as B is increased. Also, oscillation amplitude decreases as T is increased. 94

Figure 5.1 Typical Raman spectra of as-grown MLG (taken from the top surface i.e. from the "defect free region") with nominal thicknesses of (a) ~ 60 nm (batch S1), (b) ~ 200 nm (batch S2) and (c) ~ 300 nm (batch S3). (d) Typical Raman spectra of layers at the MLG/Ni interface ("defective region"). As seen from figures (a)-(c), defect (*D*) peak at 1350 cm^{-1} is absent in all these cases. The Raman 2*D* band of each batch is symmetric and can be fitted with a single Lorentzian as shown in the *insets* of figures (a), (b) and (c). In figure (d) strong *D* peak is observed from the transferred MLG sample, taken from the bottom surface. This confirms the defective nature of the interfacial layers. This is consistent with the previous observation in Figure 4.3(b). 99

Figure 5.2 Thickness dependent zero field CPP resistance $R_{zz}(0)$ and optical images of transferred MLG. (a) Zero field resistance R_{zz} (0) vs. MLG thickness. R_{zz} (0) increases with increasing MLG thickness. This indicates that the overall resistance of the device is dominated by the "bulk", not the interfaces, and the contacts. The inset shows device schematic and an equivalent circuit model of the device. As discussed in text, the combination of contact resistance and defective region resistance ($R_{cont} + R_{def}$) of all three sets of samples is < 10Ω, and shows metallic temperature dependence. The overall device, however, shows semiconducting temperature dependence. This proves that $R_{cont} + R_{def}$ does not play a dominant role in the CPP measurements. Optical images of the three transferred MLG samples are presented in Figures (b) 60 nm (batch S1), (c) 200 nm (batch S2) and (d) 350 nm (batch S3). *Insets* show typical thickness variations in these samples. 100

Figure 5.3 Interlayer magnetoresistance observed in weakly coupled MLG samples with various thicknesses. Data from (a) ~ 60 nm (S1), (b) ~ 200 nm (S2) and (c) ~ 300 nm (S3) thick samples are shown. At 50K (Figure 5.3(a)), CPP resistance sharply drops with increasing magnetic field above B_{sw} ~ 4kG and exhibits negative MR of ~ 40%. The negative MR effect becomes weaker as temperature is increased. For thicker MLG sample (Figure 5.3(b)), the negative MR is stronger, ~ 92% at 50K. For samples with even larger thickness (Figure 5.3(c)), $R_{zz}(0)$ often exceeds the upper limit (100 MΩ) of the measurement apparatus, behaving as a virtual open circuit. However as the perpendicular magnetic field is increased, resistance drops drastically by several orders of magnitude, resulting in a giant magnetoresistance that reaches theoretical maximum of ~ 100%. For all three set of samples, average of both scan directions is presented at each temperature and no hysteresis has been observed. Each resistance value is the average of 50 readings. A constant DC current of 1mA is applied to perform all MR measurements. The top inset in Figure 5.3(c) shows magnetic field dependent switching of the *I-V* characteristics at various temperatures for the 300 nm sample. (d) MR ratio ($\Delta R_{zz}/R_{zz}(0) = |R_{zz}(B) - R_{zz}(0)| / R_{zz}(0)$) as a function of MLG thickness of as-grown MLG on Ni samples at 50K. The magnetoresistance ratio increases with the thickness of MLG stack and almost reaches theoretical maximum (~1) for thickness larger than 300nm. Bottom inset shows data from a 300nm thick sample which exhibits measurable finite $R_{zz}(0)$ of ~10^7Ω. The MR data point corresponding to 300 nm thickness value in the main image is taken from this plot. The top inset shows B_{sw} vs T for the three batches..... 104

Figure 6.1 (a) Device schematic of e-beam evaporated Ni thinfilm (~ 80nm) on as-grown MLG (~ 200nm) on Ni. The deposited Ni particles penetrate in to MLG stack and modify the band structure of graphene layers. These penetrated Ni particles reduce the effective thickness of the weakly coupled MLG stack. (b) Raman spectra of before (bottom black line) and after (top red line) Ni thinfilm deposition on as-grown MLG. The as-grown MLG shows almost negligible defect peak (*D*-peak). Defects induced by Ni deposition are manifested as a strong defect peak (*D*-peak) at 1350 cm^{-1} in the Raman spectra (top red line). Except strong *D*-peak, shape and

positions of *G* and 2*D* bands are almost identical to the pre-deposition sample. Figure 1(b) inset shows XRD of bottom Ni foil (top black line) and Ni thinfilm (bottom red line). The XRD features are identical and are mainly dominated by Ni(111) grains with very low population of Ni(100) grains. (c) Device geometry of $Ni/Al_2O_3/MLG/Ni$ structure. Polycrystalline Alumina (Al_2O_3) is deposited using e-beam evaporation (0.5Å/sec, 6.5kV) followed by Ni thinfilm deposition (0.5Å/sec, 7.5kV) on as-grown MLG on Ni. (d) Raman spectrum of as-grown MLG on Ni is unchanged even after alumina (Al_2O_3) deposition (bottom black line). No defect peak at 1350cm^{-1} is observed even after e-beam evaporation of Ni on alumina coated MLG surface (top red line). 111

Figure 6.2 (a) Normalized CPP MR ($r = R_{zz}(B)/R_{zz}(0)$) of Ni/MLG/Ni for 10 – 250*K*. MR response is symmetric with field direction and no hysteresis has been observed. At 10K, low-field negative MR of ~ 4% and universal conductance fluctuations (UCF) are observed in the field range 0 – 3*kG* and a high-field negative MR of ~ 12% is observed between 4 – 8kG. These effects get weaker with increase in temperature and a positive MR of ~ 7% within 8kG is detected at 250K. (b) R_{zz}(T) at three different field values (0kG, 5kG and 10kG) for 10 – 250*K*. R_{zz} *(T)* shows insulator-like temperature dependence upto 200*K*. *Inset* shows the inverse normalized CPP resistance (r^{-1}) as a function of out-of-plane magnetic field (*B*) for the field range 4 – 8kG. The slope of $r^{-1}(B)$ curves clearly decreases with increase in temperature and this is consistent with the interlayer magnetoresistance (ILMR) model. Constant DC current bias of 1mA is used for all MR measurements. (c) Normalized CPP MR of $Ni/Al_2O_3/MLG/Ni$ structure for 15 – 125K. A large negative MR of ~ 10^3% is observed in the low-field range (< 3kG). Above 3kG, a strong and sharp positive MR (~10^9%) is observed upto 70K. This strong positive MR is gradually decreases with increase in temperature and is completely suppressed above 70K. MR response is symmetric with field direction and no hysteresis has been observed. Figure 6.2(c) *inset* displays a linear fitting for lnR_{zz} *vs. 1/kT* at a fixed field (6kG) where R_{zz} becomes constant and show plateau-like field dependence. (d) Inverse normalized CPP MR (r^{-1}) is fitted with a straight line in the low-field range at different temperatures. The decrease in slope of $r^{-1}(B)$

curve with increasing temperature clearly suggests that the low-field negative MR is due to interlayer magnetoresistance (ILMR) effect. Constant DC current bias of 1mA is used for all MR measurements. 114

Figure 7.1 Raman Spectrum and CPP MR Characteristics of MLG Samples As Grown on Co. In this sample MLG thickness is ~ 30 nm. Raman 2*D* peak is symmetric and does not show any HOPG-like shoulder peak (top image). No defect (*D*) peak has been observed in this case. Negative CPP MR has been observed in these samples for certain temperatures. 120

Figure 7.2 Schematic description of the graphene-based MTJ, which can potentially show spin filtering. The MLG is grown on the left Ni contact by CVD. 121

Figure 7.3 Magnetoresistance (MR) Study of Transferred MLG (~ 8L) on Flexible Substrates. (a) In-plane MR in transferred MLG on flexible substrate (Graphene thermal tape) with no strain introduced by substrate bending as shown in top left *inset*. Negative MR of ~1.6% is observed up to 130K. This is consistent with weak localization (WL) effect and also similar to WL effect observed in as-grown MLG (8L) displayed in Figure 3.10 (Chapter 3). (b) In-plane MR in transferred MLG with ~ 6.1mm of bending radius of substrate as displayed in top left *inset*. According to ref.[169], strain introduced on graphene layers at this bending radius is ~ 16% and a negative MR of ~ 1.2% is observed at 13K. 123

List of Tables

Table 1 Contact and sheet resistances (Rc and Rs) using TLM and van der Pauw methods……..89

List of Acronyms

2DEG

two-dimensional (2D) electron gas 5

CIP

Current-in-plane 2

CMR

Colossal Magnetoresistance 2

CPP

Current-perpendicular-to-plane 2

CVD

Chemical Vapor Deposition 2

FWHM

full-width-half-maximum 98

GMR

Giant Magnetoresistance 1

HOPG

highly oriented pyrolytic graphite 16

ILMR

Interlayer Magnetoresistance 3

MLG

Multilayer Graphene 2

MR

Magnetoresistance 1

OMAR

Organic Magnetoresistance 2

OMR

Ordinary Magnetoresistance 1

PMMA

polymethyl methacrylate 29

SdH

Shubnikov-deHaas 99

XRD

X-ray diffraction 28

1 INTRODUCTION

Magnetoresistance (MR), the change in electrical resistance of a solid-state system due to an external magnetic field [1], is a key effect in condensed matter physics, both for fundamental understanding of charge transport phenomena, as well as immense commercial implications [2]. Electrical resistance of a material originates as a result of scattering of conduction electrons from various sources such as lattice phonons, lattice defects and impurities, other electrons etc.[1]. In its simplest incarnation, MR effect originates as a result of bending of electron trajectory due to Lorentz force $\left[q\left(\vec{B} \times \vec{v}\right)\right]$, where q is electronic charge, B is external magnetic field and v is electron velocity. Lorentz force causes the electrons to move in cyclotron orbits and this change in trajectory increases overall scattering rate experienced by an electron. Thus resistance increases with increase in magnetic field, resulting in a positive magnetoresistance. This effect is generally weak (< 1%) and is known as ordinary MR (OMR) [3]. The OMR effect has been reported in many materials such as Au, Ag, Cu, Al, Na, In, Ga etc. [3].

More complex magnetoresistance effects with other physical origins have been observed in metals, semiconductors and artificial layered structures [3]–[7]. Transition metals (Ni, Fe, Co etc.) and their alloys such as Ni-Fe and Ni-Co often show anisotropic MR that originates from spin-dependent scattering of electrons due to spin-orbit interactions [4]. Metals and semiconductors also exhibit more exotic MR at low temperatures that originate from quantum effects, such as weak localization and anti-localization [5]. A physical explanation of these effects has been discussed later in this chapter. Spin-dependent scattering in ferromagnet/non-magnet multilayered structures is responsible for giant magnetoresistance (GMR) effect [2]. Such devices are ubiquitous in state-of-the-art read heads and magnetic random access memories [2]. Large MR values have also been reported in perovskite compounds such as $LaMnO_3$ and $CaMnO_3$. This effect is associated with a magnetic field assisted phase transition from paramagnetic insulator state to

ferromagnetic metallic state and is dubbed colossal magnetoresistance (CMR) [6]. Large MR values have been reported in polymers and small-molecular organics as well, and this effect is known as organic MR (OMAR) [7]. The origin of this effect is still under debate and is not adequately described by any MR effect known to date [7].

Graphite is a naturally occurring layered structure in which single graphitic layers (or "graphene") are stacked up on each other. MR in graphitic systems (single to few layers of graphene and bulk graphite) has drawn significant attention in recent years. Both current-in-plane (CIP) and current-perpendicular-to-plane (CPP) geometries have been studied extensively [8]–[13]. MR effects, such as weak localization, metal-insulator transition, linear MR, quantum Hall effect etc. have been reported in graphitic samples [8]–[14]. An overview of some of these effects has been provided later in this chapter. Layer thickness, sample quality, interaction between neighbouring graphene layers etc. play crucial role in the observed magnetoresistance effects [8]. In this thesis our focus is on multilayer graphene (MLG) epitaxially grown on ferromagnetic Ni substrate and exploration of its MR properties in current-perpendicular-to-plane (CPP) geometry.

There are different methods to produce graphene: (1) mechanical exfoliation from bulk graphite [15], [16], (2) liquid-phase exfoliation (ultrasound treatment in solution) [17], (3) epitaxial growth on SiC [18]–[20], and (4) chemical vapor deposition (CVD) on catalytic metal substrates [21]–[28]. CVD-growth of graphene on catalytic Ni or Cu substrates is a commercially viable synthesis method and is also suitable for large scale production and subsequent device fabrication [24], [28]–[30]. Additionally, several studies have indicated that the interface of epitaxially grown graphene on ferromagnet has rich underlying physics and can give rise to novel effects, such as perfect spin filtering [31], and giant Rashba splitting [32]. Band alignment at nickel-graphene interface promotes transmission of only minority spins and presence of multiple graphene layers (~ 3−4 or more) quenches majority spin conductance and leads to perfect spin filtering [31], [33].

Hybridization between π orbitals of graphene and 3*d* orbitals of nickel causes asymmetric charge distribution at nickel-graphene interface that induces a strong interfacial electric field. This electric field causes giant Rashba splitting in graphene [32]. In addition, graphene layers in CVD-grown multilayer graphene (MLG) generally show "turbostraticity" [28], [34]–[36], in which graphene layers are weakly coupled and hence these MLG samples can be viewed as a stack of two dimensional massless Dirac electron systems [37]. Based on the previous studies on similar systems [38], [39], a large negative interlayer MR (ILMR) can be expected in the current-perpendicular-to-plane (CPP) geometry, which is often dubbed interlayer magnetoresistance or ILMR. Experimental studies on these effects are rare and in this thesis, our goal is to systematically study magnetoresistance effects in CVD-grown MLG on Ni and understand its CPP-MR properties.

This thesis is divided into seven chapters. In this introductory chapter, we present some essential graphene basics and a brief overview of some of the MR effects that have been reported so far in graphitic systems[1]. Chapter 2 describes the fabrication processes and Raman characterizations that have been performed in this work. Current perpendicular to plane (CPP) MR measurements on as-grown MLG on catalytic substrates and control experiments have been presented in Chapter 3. An elaborate discussion on the observed magnetoresistance effects and their physical origin is also presented in Chapter 3. To further understand the observed CPP MR in as-grown MLG, we have performed angle and thickness dependent magnetotransport studies, which are reported in Chapter 4 and Chapter 5 respectively. In Chapter 6, we investigated spin dependent magnetoresistance effects in as-grown MLG samples using ferromagnetic metal electrodes. This allows us to understand whether spin-dependent or spin-independent MR effect is

[1] Significant work has been done on these topics in recent years. In this chapter we only provide a physical understanding of these topics. Further details are available in the references cited in this chapter.

dominant in our graphene based spin valve structures. Finally, we conclude in Chapter 7 by providing an outline of the future work plan.

1.1 Graphene Basics

Graphene is a single atomic layer of carbon atoms arranged in a two-dimensional honeycomb lattice (Figure 1.1(a)). In graphene, 2*s* and 2*p* orbitals of each carbon atom participate in sp^2 hybridization. This hybridization results in a trigonal planar structure with σ bonds between three neighbouring carbon atoms and nearest neighbour distance (a_{c-c}) of 1.42 Å (Figure 1.1(b)). Due to structural rigidity of σ bonds, these electrons are bound to the C atoms and do not participate in electrical conduction [40], [41]. The $2p_z$ orbital from each carbon atom is perpendicular to this trigonal planar structure (Figure 1.1(b)) and form bonding (π) and anti-bonding (π^*) bands in the electronic structure of graphene. The unique electronic dispersion of graphene originates from these $2p_z$ orbitals [41].

The theoretical description of graphene band structure was first proposed by Wallace in 1947 [42]. Graphene honeycomb lattice can be viewed as a combination of two equivalent but independent triangular sub-lattices (A and B as shown in Figure 1.1a) [40], [42] and the electronic dispersion of monolayer graphene [42] can be described by the relation $E(k) = \hbar v_F|k|$, where E represents carrier energy, k is the two dimensional wavevector, $\hbar$ is the reduced Plank's constant and v_F is band velocity or Fermi velocity (~ 10^6 m/s) [40]. The reciprocal lattice of graphene is a hexagon (Figure 1.1(c)) with six corners of the Brillouin zone alternatively represented by K and K'. The conduction and valence bands of graphene meet at K and K' points known as Dirac points [40]. Most of the exciting physics observed in graphene occur around these Dirac points [15], [16], [40], [43]. Charge particles in this linear energy dispersion act like relativistic massless particles [15], [40]. In intrinsic graphene, Fermi level is located at the Dirac point and the density of states (DOS) is zero at the Dirac point [40], [41], [44]. External magnetic field applied normal to the graphene plane can significantly affect the graphene band structure. This magnetic field effect is discussed in the next section.

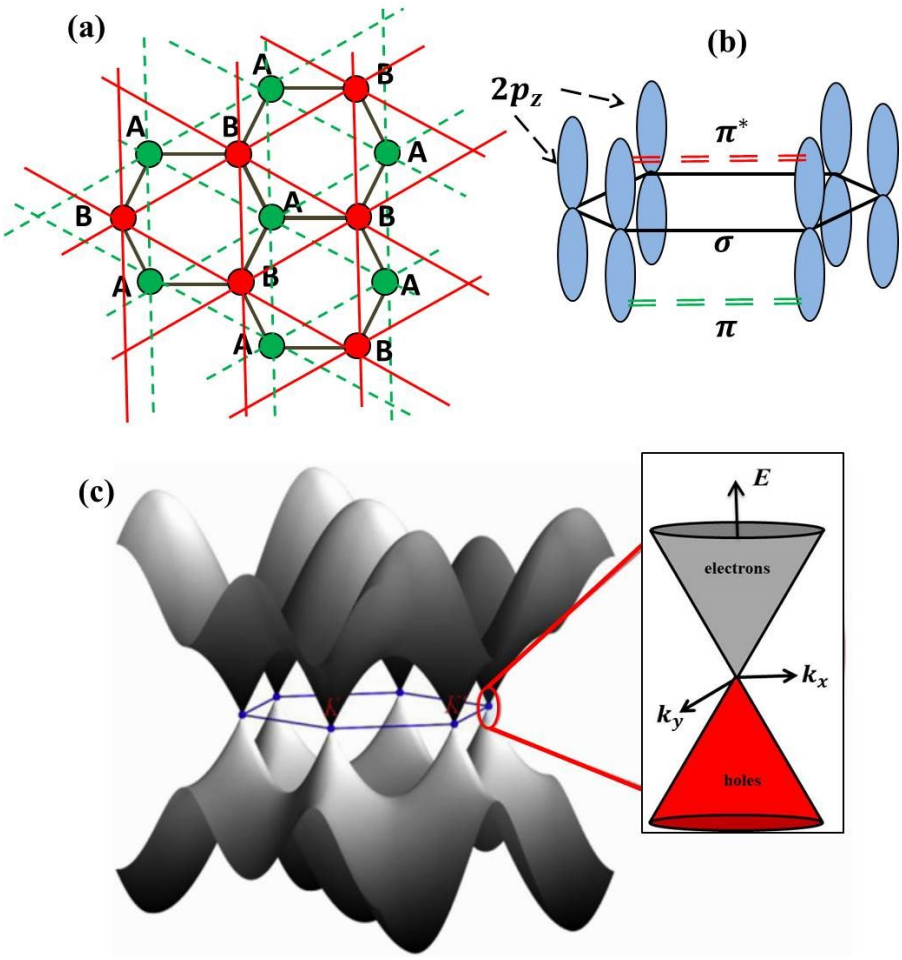

Figure 1.1 Honeycomb lattice and band structure of graphene. (a) Interpenetrating triangular sub lattices (A, B) of graphene are represented by dashed and solid lines respectively; (b) σ bonds between carbon atoms in the hexagonal arrangement and π bonds between $2p_z$ orbitals oriented perpendicular to the graphene plane; (c) Zero band gap and linear energy dispersion of graphene close to the Dirac points (adopted from ref. [40]).

1.2 Graphene in Magnetic Field

As mentioned before, graphene is a single atomic layer of two-dimensional (2D) electron gas (2DEG) with linear electronic dispersion. To understand graphene

band structure under an external magnetic field, it is useful to consider the conventional 2D electron gas system with parabolic energy dispersion[2].

In the presence of an external magnetic field (B) applied normal to the plane, the classical Lorentz force causes electrons to rotate in a circular trajectory at cyclotron frequency ($\omega_c = qB/m_c^*$). Here, q is the electronic charge and m_c^* is electron's effective cyclotron mass. These circular orbits are known as cyclotron or Landau orbits (Figure 1.2) and the electrons in these orbits have zero translational velocity. Quantum mechanically, electron wave functions can be considered to be confined within the radii of these cyclotron or Landau orbits. This system is analogous to the electron in an infinite potential well in which case quantized discrete energy values are observed as a result of confinement. Since the electrons are "confined" in Landau orbits, their energies are expected to be quantized as well.

The energy of the Landau orbits can be estimated as follows. We equate the circumferences of the Landau orbits with the integral multiple of de Broglie wavelength (λ):

$$2\pi R_c = n\lambda \Rightarrow 2\pi R_c = n\left(\frac{h}{p}\right) \Rightarrow R_c = n\left(\frac{h/2\pi}{p}\right) = n\left(\frac{\hbar}{p}\right) \quad (1)$$

where R_c is the cyclotron radius, p is the momentum of electron in cyclotron orbit and n is the quantization index [45].

Electron rotating in a cyclotron orbit experiences a centrifugal force of magnitude $(m^*v^2)\ /\ R_c$ where m^* is the effective mass of electron, v is the velocity of electron in cyclotron orbit. As mentioned before, electrons in cyclotron orbits also experiences Lorentz force $\left[q\left(\vec{B} \times \vec{v}\right)\right]$. Since both forces are radial and there is no radial acceleration therefore,

$$qBv = {m^*v^2}/{R_c} \Rightarrow R_c = {m^*v}/{qB} = {p}/{qB} \quad (2)$$

Eliminating R_c from equations (1) & (2), we can obtain the Landau level energy as $E_n = \frac{1}{2}n\hbar\omega_c$. By eliminating p from equations (1) & (2), we can obtain $R_c =$

[2] Full quantum mechanical analysis of this problem is available in ref.[45]. In this section, however, we provide a qualitative picture in order to obtain a physical understanding of this problem.

$\sqrt{\frac{n\hbar}{qB}}$. An exact quantum mechanical analysis of the electrons in Landau orbits shows that Landau level energies can be expressed as, $E_n = \hbar\omega_c(n + 1/2),\ n = 0, 1, 2,..$ (Figure 1.2 (c)) [45]. Discrete energy (Landau level) description is more appropriate at low temperatures (and/or high magnetic fields) where the separation between Landau levels ($\hbar\omega_c$) is larger than the thermal broadening ($k_B T$) [45]. Here k_B is Boltzmann constant and *T* is temperature. In addition, disorders and impurities in the lattice structure also induce some Landau level broadening. In presence of high impurity concentration and defects, formation of distinct Landau levels is suppressed by Landau level broadening.

In the classical interpretation described above, at a fixed magnetic field, electrons in cyclotron orbits with different radii correspond to different Landau levels. For a given Landau level (say n = 1 or any fixed value), the number of allowed states (N) or degeneracy can be estimated as the number of cyclotron orbits with same radius (R_c) that can be fitted within the boundaries of the 2DEG system. This can be expressed as,

$$N\pi R_c^2 = Area\ of\ 2DEG\ (W \times L)$$

From above expression, degeneracy (N) of Landau level (n = 1) can be obtained as,

$$N = \frac{WL}{\pi R_c^2} = \frac{WL}{\pi\left(\sqrt{\frac{\hbar}{qB}}\right)^2} = \frac{WLqB}{h} \qquad (3)$$

As shown in equation (3), degeneracy (N) of a Landau level is proportional to the magnetic field (B). Thus, more states will be available for each Landau level at higher magnetic field strength. Therefore, each Landau level can accommodate more electrons with increase in magnetic field. As the number of electrons in the 2DEG is fixed, the number of fully filled Landau levels decreases with increase in field strength (Figure 1.2 (c)) [45].

Unlike 2DEG with parabolic dispersion, electronic dispersion of graphene is linear. For such 2D massless Dirac electron system, Landau levels show square root dependence on both field (B) and Landau level index (n), which can be described by the relation $E_n = \pm\sqrt{2q\hbar v_F^2|n||B|}$ (Figure 1.3) [40], [44]. Here $n = 0, \pm1, \pm2, ...$ are the Landau quantization indices. In presence of a magnetic field normal to the graphene plane, the continuum of density of states condenses into discrete Landau levels (Figure 1.3) At Dirac point, a field independent state called "zero-mode Landau level" ($n = 0$) appears, which is one of the unique characteristics of 2D massless Dirac electron system [15], [40], [44]. For intrinsic graphene, the zero-mode Landu level (LL_0) at the Dirac point coincides with the Fermi level (E_F). As the Fermi distribution function is always $1/2$ at E_F, half of the Landau states at zero-mode (LL_0) are occupied.

1.3 Multilayer Graphene (MLG) and CVD Growth

The electronic properties of graphene change with increasing layer number because interlayer coupling between the constituent layers significantly affect the band structure [34], [44]. The way the graphene layers are stacked on each other plays a crucial role in determining the interlayer coupling and hence electronic band structure of multilayer graphene (MLG). Stacking of graphene layers is generally represented by three different arrangements (A, B and C) based on layer projection on x-y (basal) plane (Figure 1.4). Common stacking sequences of multilayer graphene samples are hexagonal (AAA stacking), Bernal (ABAB stacking) and rhombohedral (ABC stacking) [46]–[48]. These stacking sequences have been observed in MLG samples extracted from highly ordered pyrolytic graphite (HOPG) [46]–[48]. In hexagonal (AAA) stacking order, the graphene layers are stacked exactly on top of each other. Bernal and rhomdohedral stacking sequences are most common in HOPG samples compared to hexagonal stacking [46], [47]. Schematic representations of Bernal and rhombohedral stacking are shown in Figure 1.4. For Bernal stacked MLG, alternate layers have the same projection on the basal plane (Figure 1.4(a)). Whereas in rhombohedral stacking, second and third layers are shifted with respect to the first layer and the fourth layer shows similar

projection on the basal plane as the first layer (Figure 1.4 (b)). The interlayer spacing of the rhombohedral stacking is 3.37 Å, which is comparatively higher than Bernal stacking (3.35 Å) [34]. For both Bernal and rhombohedral stacking orders, valance and conduction bands at the Femi level are very complex and the dispersion relation is parabolic rather than linear (Figure 1.4) (c) and (d)).

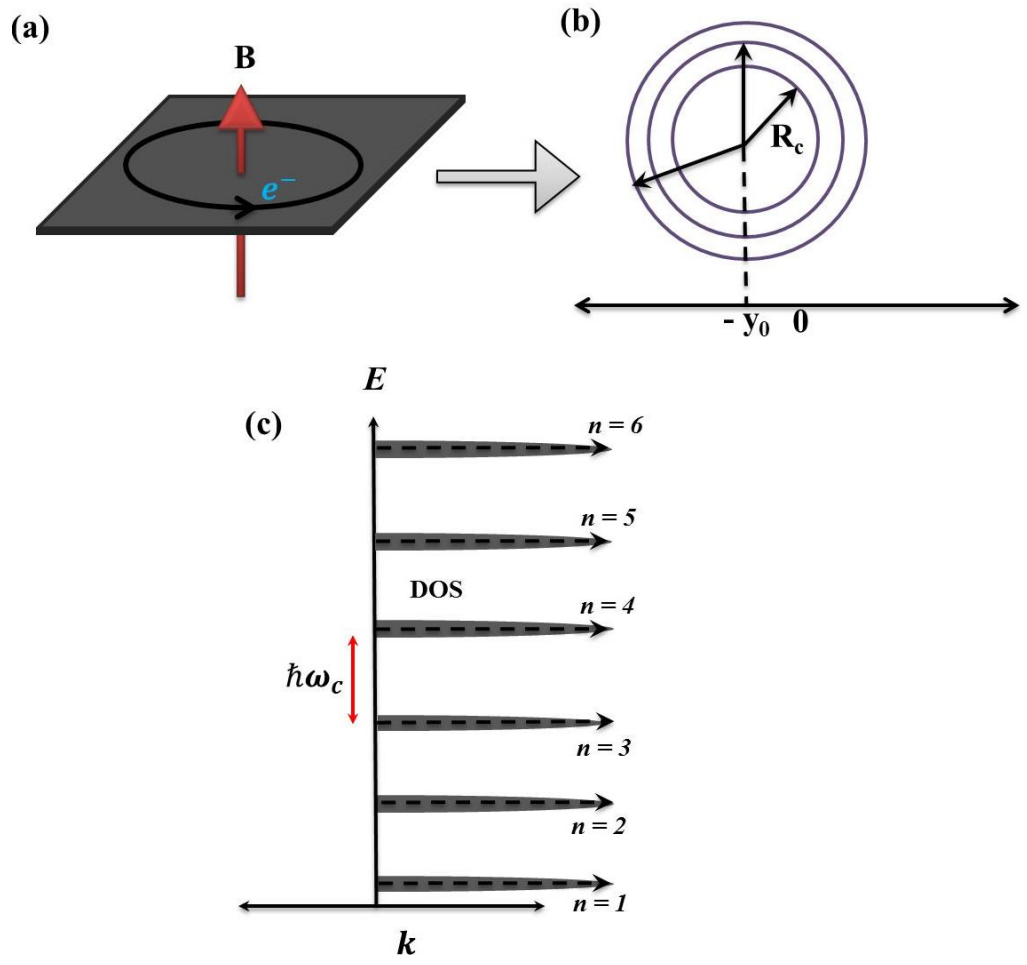

Figure 1.2 A 2D electron gas material with parabolic energy dispersion, in presence of a uniform and static magnetic field applied normal to the plane. (a) Electron in cyclotron orbital, (b) Electrons in cyclotron orbitals with centre at $-y_0$ and quantized radii, (c) Energy levels (Landau levels) in presence of magnetic field. Note that Landau levels are equally spaced and the spacing between neighbouring Landau levels is $\hbar\omega_c$ (adopted from [45]).

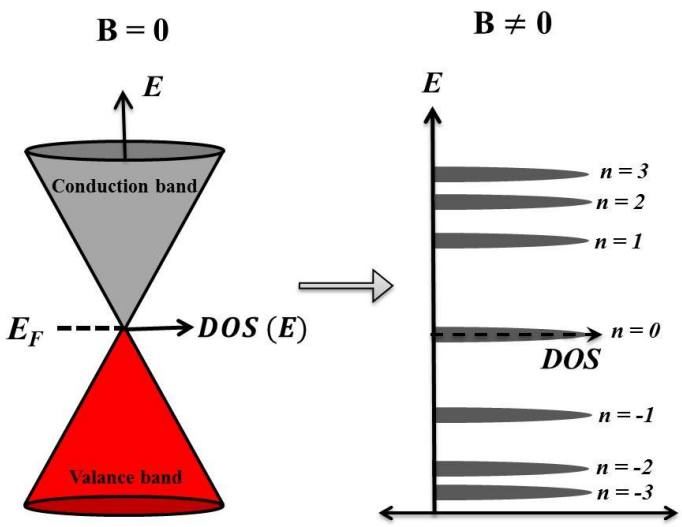

Figure 1.3 Density of states (DOS) of graphene for $B = 0$ and for $B \neq 0$. For $B \neq 0$, the linear DOS of graphene condenses into quantized, unequally spaced Landau levels (LLs). A schematic description is shown above. The zero mode Landau level (LL_0) is located at Fermi level (E_F), which coincides with the Dirac point.

For instance, valance and conduction bands of Bernal stacked trilayer graphene split into multiple bands due to interlayer coupling, even with zero energy gaps (Figure 1.4(c)) [34], [44]. The change in electronic structure is significant up to few layers of graphene and becomes smaller for thicker graphite. Interlayer interaction therefore plays crucial role in modifying band structure of MLG. CVD-grown MLG however shows contrasting features compared to MLG mechanically exfoliated from HOPG. Bernal and rhombohedral stacking orders are not very common in CVD-grown or epitaxial graphene. Graphene layers in epitaxially grown MLG on SiC are randomly oriented with weak interlayer coupling [19], [49]. Similarly, CVD-grown MLG on metallic substrates (e.g. Cu or Ni) also exhibit random orientation of stacked graphene layers without any specific angle [28], [36]. This kind of MLG with randomly oriented graphene planes is known as "turbostratic graphite". The adjacent layers in turbostratic graphite are parallel to each other, but randomly oriented relative to each other [28], [50]. This rotational disorder decouples adjacent graphene layers and re-establishes the linear energy dispersion of the monolayer graphene near the Fermi level. Due to this reason, despite the presence of adjacent layers in turbostratic graphite, the 2D electronic properties of monolayer graphene are preserved [37], [50] and turbostratic graphite can be

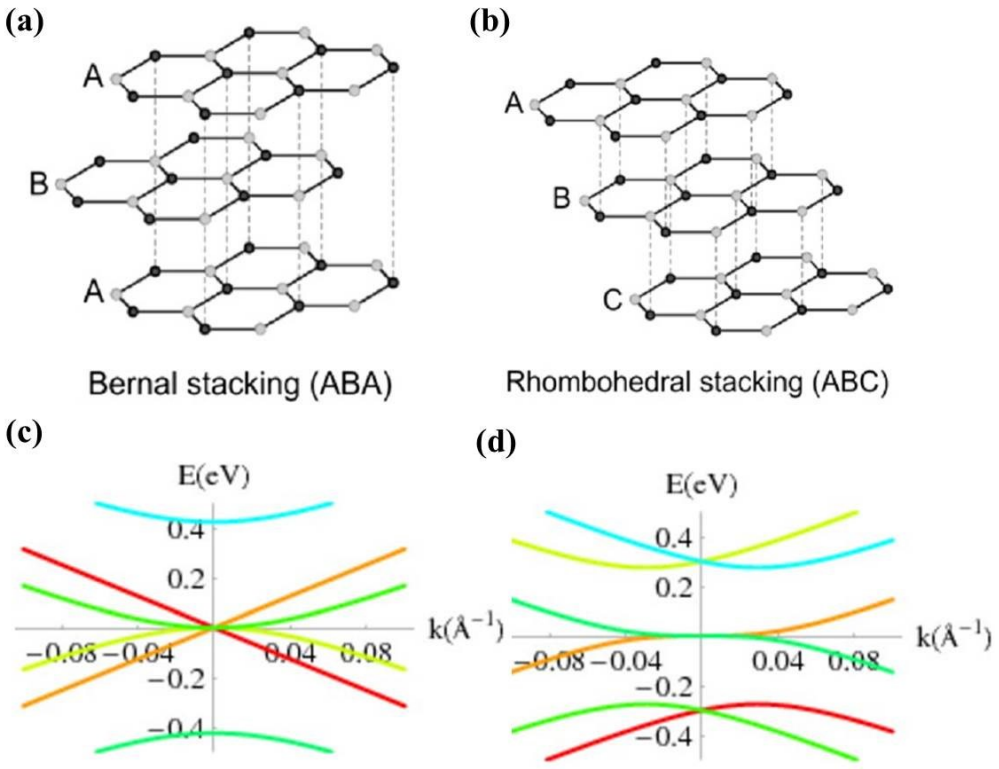

Figure 1.4 Stacking sequence and electronic bands of MLG. (a) and (b) panels show Bernal and rhombohedral stacking sequence respectively (taken from ref.[46]). (c) Electronic bands of trilayer graphene with Bernal stacking. (d) Electronic bands of trilayer graphene with rhombohedral stacking (taken from ref. [44]).

viewed as a stack of two-dimensional Dirac electron systems instead of three-dimensional bulk graphite.

1.4 Magnetoresistance in Graphene Based Systems

MR effects in graphitic systems have been studied extensively in recent years with different device geometries under various orientations of the external magnetic field. As mentioned earlier, layer thickness, stacking order and defects can significantly influence MR effects in graphitic systems [8], [10], [12], [51]. Some of the prominent magnetoresistance effects observed in graphitic systems are: (a) weak localization [10], [12], [13], (b) linear MR [8], [52], [53], and (c) metal-insulator transition [9], [54]. A brief overview of these effects is provided below. Detailed description of these effects are available in the cited references.

1.4.1 Weak Localization

The wave nature of an electron in a material typically manifests via quantum interference effects at low temperatures [1]. Weak localization is such a quantum interference effect that occurs in impure conductive materials and results in negative MR. In any impure conductive material, conduction electrons diffuse through various impurities or defects with a finite mean free path. There is a finite probability for the conduction electrons to diffuse in a closed trajectory through multiple scattering centres and reach the starting point or origin (Figure 1.5, solid line) [5]. Due to electron's wave nature, there will be another (dotted line in Figure 1.5) diffusion path in opposite direction [3], [5]. These partial waves return to the origin with the same phase and amplitude, which results in a constructive interference. This constructive interference increases electron's tendency to remain at origin (starting point) and causes a slight decrease in intrinsic conductivity of the material [5]. This phenomenon is known as "weak localization". Application of an external magnetic field normal to the plane adds an extra phase between these two partial waves and the constructive interference is either reduced or destroyed [5]. This loss of phase coherence between the partial waves is proportional to the magnetic field strength. This effect can be observed as a gradual drop of material resistance with increasing magnetic field strength, and hence a negative MR effect [5]. This negative MR due to weak localization effect is generally observed at low temperatures where the wave nature of electron is preserved and phase breaking events due to phonons are rare. Weak localization effect manifests in any conductive material in spite of its dimensionality. However, the two dimensional (2D) case is most favourable for an experimental observation of this effect [5].

For monolayer graphene, due to chiral nature of the charge particles, an additional phase of π adds between electron waves traveling in a closed trajectory. This additional phase, also known Berry's phase, destroys the constructive interference between electron waves and supresses the weak localization effect [13]. For this system, presence of an external magnetic field re-establishes the phase coherence between electron waves and exhibits a positive magnetoresistance [8], [55].

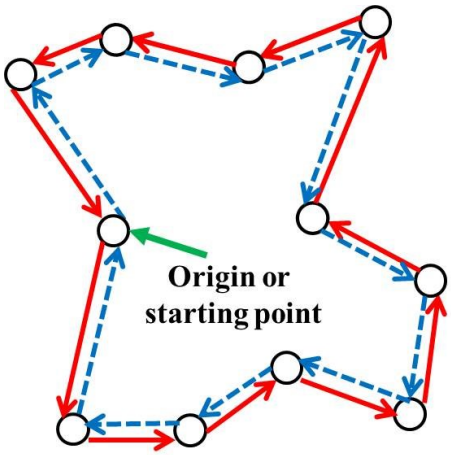

Figure 1.5 Weak localization effect. Diffusion paths of a conduction electron in both directions (full and dashed lines) between scattering centres (impurities or defects). Weak localization occurs when a conduction electron finishes a closed trajectory and reaches the origin or the starting point (adopted from [5]).

This effect is known as weak anti-localization [8], [55]. In case of multilayer graphene, in current-perpendicular-to-plane (CPP) geometry conduction electrons scatter at graphene/graphene interface due to grain boundaries and defects [8]. Many such scattering events in a stack of MLG provide some finite probability for conduction electrons to diffuse in a closed trajectory. As described above, weak localization effect can be observed in this case as the conduction electrons diffuse in a closed trajectory and has a finite probability to reach the starting point or origin. We have observed such weak localization effect in our devices as well, which is consistent with literature [8]. These results are discussed in Chapter 3. Such weak localization effects have also been reported for current-in-plane (CIP) geometry. In this case main source of scattering is from the grain boundaries [56].

1.4.2 Classical and Quantum Linear MR

Generally, conducting materials exhibit quadratic magnetoresistance dependence ($R \propto H^2$) at low field values [3], [53], [57]. This MR is relatively small in magnitude ($< 1\%$) and typically saturates at higher field values [3]. However, in some disordered thin films such as doped silver chalcogenides ($Ag_{x+2}Se$), a non-saturating linear MR has been observed [58]. This behavior can be interpreted classical and quantum mechanical terms.

A classical theory of linear MR has been given by Parish and Littlewood [58]. This theory is mainly based on the inhomogeneity of the material, which was modeled as a random array of resistive disks [58]. For magnetic field applied normal to the plane, Lorentz force causes charge carriers to rotate in circular trajectories (cyclotron orbits) in each individual disk. This induces a transverse voltage called Hall voltage in the direction perpendicular to both magnetic field and bias direction. Since Hall voltage increases linearly with magnetic field, the resultant MR in the bias direction also exhibits a linear response. However, Hall voltage alone cannot completely describe this large, non-saturating MR effect. As mentioned above, in this model, the inhomogeneity of materials has been modeled as the random arrangement of resistive disks. Such randomness can generate multiple current paths in various directions in addition to the direction of applied bias. These random current paths collectively contribute to the large linear MR values [58].

The quantum mechanical theory of linear MR is more suitable for a 2D electron gas system. As discussed in section 1.2, in a 2D electron gas system, discrete energy levels (Landau levels) appear when a magnetic field is applied normal to the plane [52], [53]. The quantum linear MR is noticeable when these Landau levels are distinct enough ($\hbar\omega_c > k_B T$) [1], [53] and only one Landau level is available for the charge transport at the Fermi level [53]. Such situation is known as the "extreme quantum limit" [53], [57]. In this case, the in-plane conductivity is mainly due to hopping of charge carriers between quantized Landau orbits [53]. This hopping is mainly activated by scattering centers in the system [53]. Therefore, in these materials, increase in impurity concentration also increases the electrical conductivity. The linear response of magnetoresistance in this model originates from the degeneracy of Landau level. This theory is mostly applicable to metals that have small carrier density and low effective mass [53]. In graphitic systems, such a situation occurs in CIP geometry when the Fermi level is located at the zero-mode Landau level [53], [59].

1.4.3 Field Induced Metal-Insulator Transition

In multilayer graphene, metal-insulator transition has been reported in both CIP and CPP geometries when a magnetic field is applied normal to the plane (c-axis) [9], [60]. In presence of this perpendicular magnetic field, formation of electron-hole pairs or excitons occurs in each graphene layer, when the Coulomb interaction is strong [54]. Therefore, the Coulomb interaction effectively increases fermionic dynamical mass. As a result, massless linear energy dispersion of graphene converts into parabolic. This interaction also breaks the chiral symmetry and opens a band gap (Δ) [54]. Thus in presence of magnetic field graphene transforms from a metallic state with zero gap to an insulating state with finite band gap [54]. This field induced metal-insulator transition results in a positive magnetoresistance effect [9]. The excitonic gap (Δ) deteriorates at higher temperatures ($k_B T \geq \Delta$) or at higher charge densities [60]. This magnetic field induced insulator state disappears when the magnetic field is parallel to the plane [9], [60].

1.4.4 Interlayer Magnetoresistance (ILMR)

Negative MR in the CPP geometry can also arise from an interlayer tunneling mechanism, which is often dubbed "interlayer magnetoresistance" or ILMR [38], [39], [61], [62]. This effect is observed in a stack of two-dimensional (2D) massless Dirac electron systems. The interlayer coupling between these 2D layers should be sufficiently weak so that the entire system can be viewed as a stack of 2D systems instead of a bulk 3D material. In such systems out-of-plane charge transport occurs via interlayer tunneling. Such interlayer current can be tuned by a large factor by applying an out-of-plane magnetic field. The physical origin of this ILMR effect is described below.

As mentioned before, for a stack of weakly coupled 2D massless Dirac electron system in absence of any magnetic field, electronic dispersion of each layer can be modeled by a linear E-k spectrum (or "Dirac cone dispersion") with Fermi level located at the Dirac point [44]. Density of states (DOS) is small at the vicinity of the Dirac point, since it depends linearly on energy measured from the Dirac point

[44]. When an out-of-plane electrical bias is applied, carriers tunnel from one layer to the next. In this case, small interlayer current is expected due to low DOS near the (quasi) Fermi levels.

As explained in Section 1.2, when an out-of-plane magnetic field is applied, linear E-k dispersion of each layer converts into a series of Landau levels, with a (zero mode) Landau level located at the Dirac point [44]. Out-of-plane charge transport will now occur via interlayer tunneling between the zero mode Landau levels. The degeneracy of the Landau levels increases with magnetic field. Thus with increasing magnetic field, degeneracy of the zero mode Landau level will increase, giving rise to larger tunneling current. This is the origin of negative MR and is dubbed ILMR.

1.4.5 Bright's Model

Bright's model also discussed negative MR in disordered carbon, which is characterized by a two-dimensional band structure and density of states [63]. Negative MR originates because of magnetic field-induced changes in the density of states, which leads to increased carrier concentration with the field and a concomitant suppression of device resistance. This is very similar to the ILMR effect described above. However Bright's model differs from above explained ILMR model with two features: (1) the presence of shallow acceptor levels, due to defects, and (2) the presence of extra density-of-states at the zero mode Landau level, due to partial three-dimensional ordering of the constituent graphene layers. Due to these differences, Bright's model predicts significantly smaller negative MR, approximately 2% at low temperatures [63].

1.5 Graphene Synthesis

Graphene can be prepared by micro-mechanical exfoliation from natural graphite or highly oriented pyrolytic graphite (HOPG) [16]. High quality, electronic grade graphene can be prepared by simply peeling-off few layers of graphene from thicker graphitic samples using scotch tape [16], [64]. However, this method only produces small-scale graphene samples with random dimensions and therefore this

method is not suitable for large-scale production. Large area graphene can be grown on metal surfaces by surface segregation of dissolved carbon atoms or by the decomposition of hydrocarbons in the chemical vapor deposition (CVD) process [27], [28], [29], [65]. Studies on CVD-grown graphene have mainly used Ni and Cu as catalysts in the CVD process [27]–[30], [65], [66]. Recently, large area epitaxial graphene has been grown on single crystal SiC wafers by annealing at high temperatures (> 1300℃) [67]. Graphene grown on SiC exhibit high mobility ($> 4 \times 10^{12} \frac{cm^2}{V.S}$) and good quality, but it is difficult to transfer on arbitrary substrates and therefore limits the device fabrication to SiC substrate only [68]. Graphene, CVD-grown on Ni or Cu, is easy to transfer, transfer process is compatible with SiO_2, and is suitable for fabrication of electronic devices.

CVD growth of graphene on Ni consists of following steps: (a) introduction of carbon precursor at high temperature, (b) diffusion and mixing of carbon precursor with bulk Ni, (c) segregation of dissolved carbon at Ni surface and formation of graphene on Ni surface during cooling of the Ni substrate [28], [30], [69]. For the first step, temperatures higher than 900 ℃ are required to dissolve and diffuse carbon into bulk Ni. As solubility of carbon is high in Ni, large amount of carbon diffuses into bulk Ni. Therefore, controlling cooling rate during carbon segregation is essential to obtain required thickness of MLG [29], [69], [70]. Under optimum cooling rate of Ni substrate, uniform and large area graphene layers are obtained (Figure 1.6). Unlike Ni, carbon solubility in Cu is almost negligible [71] and graphene growth takes place only by surface adsorption of carbon atoms [29]. A detailed description of CVD process flow and process parameters is provided in Chapter 2.

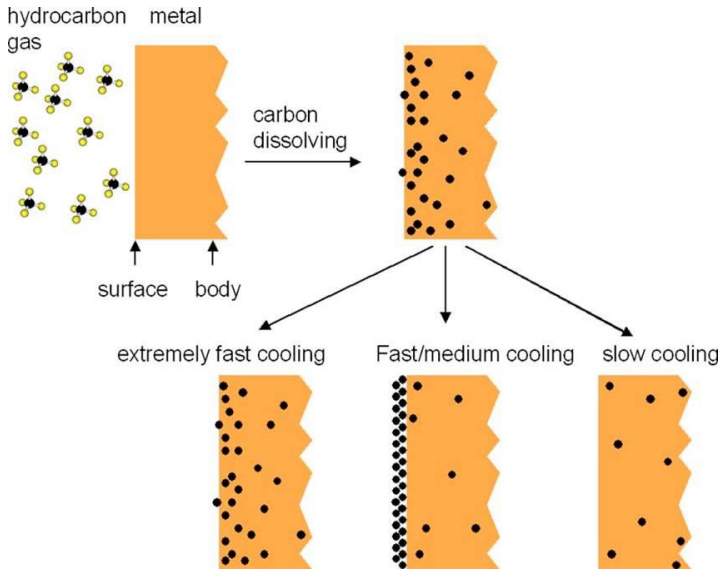

Figure 1.6 Graphene growth on Ni substrate by CVD. Medium cooling rate during carbon segregation provides uniform and large area MLG (taken from ref.[30]).

1.6 Raman Spectroscopy of Graphitic Systems

Raman spectroscopy [72] is a non-destructive characterization tool that is instrumental for characterizing structural and electronic properties of graphene [34], [73], [74]. Two types of scattering occur when a material is illuminated by light: Rayleigh scattering and Raman scattering [74]. Rayleigh scattering is an elastic scattering and most of the scattered photons undergo this process. In Rayleigh scattering, the scattered photon comes out with the same frequency as incident photon. The nuclei of the molecule are undisturbed in Rayleigh scattering as the interaction is only between photon and the electron cloud of the molecule [75]. Rayleigh scattering has been widely used to count number of graphene layers when placed on an optimized substrate (300nm SiO_2/Si) [76]. However, this method does not provide any electronic or structural property of graphene.

Raman scattering, on the other hand, is an inelastic scattering process and can provide more details about structural and electronic properties of graphene. Raman scattering only occurs for roughly one out of ten million photons [75]. In this process, the scattered photon shows a frequency shift with respect to the frequency of the incident photon [75]. Thus in Raman spectroscopy, the vibrational frequency of the molecule is represented as frequency shift [75]. Again, based on this

frequency shift, Raman scattering is divided into two categories: Stokes and anti-Stokes [74]. In Stokes process, the incident photon loses part of its energy and comes out with a lower energy. Whereas, in anti-Stokes, the scattered photon gains some energy as the sample is already in an excited state before incoming photon strikes. Generally, anti-Stokes process is weaker and harder to detect than Stokes. Hence, Stokes is most widely used to report Raman spectra of graphene.

Graphitic systems are generally affected by various processing steps during device fabrication [64], [68]. Raman spectroscopy is able to identify any structural change and presence of defects that are introduced during processing and transfer steps [77], [78]. To properly interpret Raman spectra, it is important to understand phonon dispersion in graphene. As mentioned before, the unit cell of graphene consists of two carbon atoms (A and B), which results in six phonon modes. Three of these phonon modes are acoustic (*A*) and the remaining three are optical (*O*) [34]. Based on atomic vibrations parallel or perpendicular to the plane of graphene, phonon modes are categorized into in-plane (*i*) and out-of-plane (*o*) modes. Based on the direction of nearest carbon-carbon atoms, the direction of vibration can be classified into transverse (T) and longitudinal (L). Raman spectra of graphene consist of three optical phonon modes (LO, *i*TO, *o*TO) and two acoustic phonon (LA, *i*TA) modes [34], [74]. Raman peaks correspond to acoustic phonon (LA, *i*TA) modes are generally very weak [79], [80] and rarely used to analyze structural properties of graphene [74], [80], [81]. Such analysis is beyond the scope of this work and therefore not included in this report. Most prominent peaks in the Raman spectra of graphene are labeled as G, G' $(2D)$ and D. These peaks mainly involve optical phonon modes. *G* peak appears at 1580 cm^{-1} and corresponds to the in-plane optical phonon mode (LO and *i*TO). It indicates presence of hexagonal lattice of carbon atoms.

The *2D* band in the Raman spectrum of (monolayer) graphene originates due to a 2^{nd} order, two-phonon, "double resonance" process, which has been analyzed extensively by various theoretical and experimental techniques [34], [73], [81]–[83].

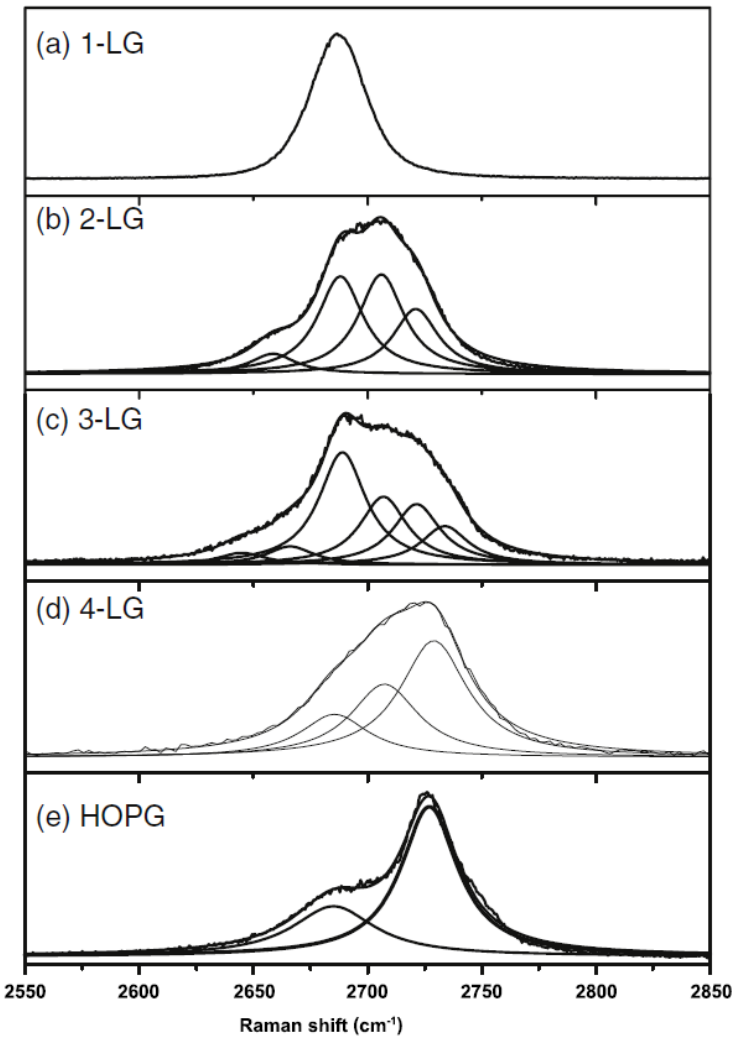

Figure 1.7 2*D* band of Raman spectra taken with laser energy of 2.41 *eV* for (a) 1-layer, (b) 2-layer, (c) 3-layer, (d) 4-layer and (e) HOPG (taken from ref.[34]).

In this process, first an electron-hole pair is created around *K* valley by an incident laser photon. Next, the electron is scattered by an (*i*TO) phonon to *K'* valley. Then the electron is scattered back to the *K* valley by another *i*TO phonon. This electron then recombines with a hole and emits a photon. For monolayer graphene this process leads to a single Lorentzian 2*D* peak in the Raman spectrum (Figure 1.7(a)).

The 2*D* band of monolayer graphene exhibits a single Lorentzian peak with a full width at half maximum (FWHM) of ~ 24 cm^{-1} [34] (Figure 1.7 (a)). Now, for bilayer/trilayer graphene or graphite the single electronic dispersion curve of monolayer graphene is split into multiple branches due to interlayer coupling

(Figure 1.7). As a result, above-mentioned double-resonance scattering processes can take place between various branches, resulting in multiple slightly-shifted Lorentzian peaks. The resultant 2*D* band is a combination of all these Lorentzians and therefore loses its symmetrical shape and becomes significantly asymmetrical (Figure 1.7 b-e). In particular, for bilayer graphene four double-resonance processes can occur resulting in four Lorentzians in the vicinity of ~ 2700 cm^{-1}. The resultant 2*D* band is the combination of these four components and no longer represents a Lorentzian. Similarly, for trilayer graphene fifteen different transitions are possible and the 2*D* band consists of fifteen Lorentzians in the vicinity of ~ 2700 cm^{-1} [84]. However, splitting in Raman 2*D* band is negligible if the interlayer coupling between constituent graphene layers is weak. Such weak interlayer coupling and absence of splitting in the 2*D* Raman band have been reported by many groups in the past in CVD-grown MLGs and turbostratic graphite [28], [34]–[37]. The position of the 2*D* band slightly varies with the change in incident laser energy. For instance, laser energy of 2.41eV is used to generate the Raman spectrum in Figure 1.7.

Another prominent band in the Raman spectra of graphene is the defect (*D*) band that appears at 1350 cm^{-1}. The *D* band in the Raman spectra also originates from double resonance process. In this case, first, an electron-hole pair is created around *K* valley by the incident laser photon. Next, the electron is scattered by a defect to the *K'* valley. Next, the electron is scattered back to the *K* valley by an *i*TO phonon. This electron recombines with a hole and emits a photon [34]. The *D* band therefore sheds light on the amount of structural defects present in the sample.

1.7 Metal-Graphene Interface

Since in the CVD process, graphene is grown on a metal catalyst, it is important to understand the nature of interaction at metal-graphene interface. These interfaces play a crucial role in the operation of graphene based electronic devices. Depending on the nature of the interaction, graphene-metal interfaces can be broadly classified into two categories: physisorption interface and chemisorption interface [85]–[88]. Metals such as Al, Cu, Ag, Au and Pt, typically form “physisorption interface” with

graphene [85]–[88]. For physisorption interfaces, the electronic structure of interfacial graphene remains essentially unperturbed, and hence such metal contacts are ideal for probing the (magneto-) transport properties of pristine graphene [87], [89], [90]. "Chemisorption interface", on the other hand, is characterized by a strong chemical bond between interfacial graphene and metal (Co, Ni). This bond modifies the electronic structure of pristine graphene, including elimination of the Dirac point, band gap opening and creation of metal-graphene hybrid localized states in the gap [85]–[88].

Graphene epitaxially grown on (111) Ni [28], [30], [65], [66], [91] generally forms chemisorption interface. This chemisorption interface forms due to strong overlap between $3d$ states of Ni and $2p_z$ states of carbon. In spite of the detrimental effect on the graphene electronic structure, chemisorption interfaces can potentially exhibit interesting properties such as perfect spin filtering [33] and giant Rashba splitting [32]. For example, energy-level alignment at the (111) Ni-graphene interface promotes transmission of only minority spins, resulting in perfect spin filtering [33], [92]. Further, chemisorption interfaces enhance spin-orbit effects at the interface, and magnetization can be induced to the carbon atoms [93]. These areas are still underexplored to date.

1.8 Motivation of This Thesis

MR in graphitic systems (single to few layers of graphene and bulk graphite) has drawn significant attention in recent years. Both current-in-plane (CIP) and current-perpendicular-to-plane (CPP) geometries have been studied with various orientations of the external magnetic field and various MR effects (as described before) have been reported [8], [9], [11], [52], [94]. However, CVD-grown graphene exhibits several unconventional properties that are not observed in HOPG-derived graphene. As mentioned previously, for CVD-grown MLG on Ni, hybridized Ni/graphene interface can potentially show intriguing properties such as perfect spin filtering [33], and giant Rashba splitting [32]. At the same time, CVD-grown MLG on Ni shows weak coupling between constituent graphene layers

(turbostratic graphite) [28], and presence of two-dimensional massless carriers in these layers has been confirmed by Landau level spectroscopy [37]. Thus this system can potentially exhibit large interlayer magnetoresistance (ILMR) in the current-perpendicular-to-plane (CPP) geometry [38]. However, experimental work in this area is very rare (if any). In this work, we have systematically studied magnetoresistance effects in CVD-grown MLG and have explored the roles of "turbostraticity" and the "hybridized nickel-graphene interface" in the observed MR effects. To pursue this, we have grown turbostratic MLG on Ni substrate using CVD process [65], [95], and then studied MR effects in CPP geometry. Temperature dependent measurements and various control experiments have been performed to identify the dominant MR effect.

1.9 Summary of Contributions

The original contributions throughout the different stages of this thesis are highlighted below.

1. In the first stage of this thesis, we have successfully grown defect-free, turbostratic multilayer graphene (MLG) on nickel foil using CVD process. The MLG samples have been extensively characterized by Raman spectroscopy and electrical measurements. These samples exhibit a novel large, negative MR effect in CPP geometry with the magnetic field normal to the plane. A negative MR effect of ~10^4% has been observed, which persists even at room temperature. The observed negative MR disappears when the Ni-grown MLG is transferred on a separate electrode. Fabrication and characterization of these devices have been described in Chapter 2 of this thesis. CPP-MR data has been presented in Chapter 3.

2. In the second stage of this work, we have investigated the underlying reason behind the large negative CPP-MR by designing and performing multiple control experiments. We found that the observed negative CPP-MR effect is correlated with the shape of the 2*D* band as well as with the absence of *D* peak in the Raman spectrum. The observed data has been found to be consistent with the "interlayer

magnetoresistance" (ILMR) mechanism in which interlayer charge transfer occurs between the zero mode Landau levels of weakly coupled two-dimensional massless Dirac electron systems. Due to large MR value and its persistence at room temperature, this effect is expected to have commercial implications and encourage further research on MLG physics and MLG growth mechanisms on ferromagnetic substrates. Detailed discussion of the control experiments and interpretation of the experimental results are provided in Chapter 3 of this thesis.

3. In the third stage of this thesis, the effects of temperature, field direction and MLG-thickness on the observed interlayer magnetoresistance (ILMR) are investigated (Chapter 4 and Chapter 5). This provides further understanding of ILMR in as-grown MLG and allows us to explore different parameters to control this effect in as-grown MLG stacks.

4. In the final stage (Chapter 6), we investigated spin polarized transport in as-grown MLG samples using ferromagnetic metal electrodes. This allows us to understand whether spin filtering effect or ILMR effect is dominant in MLG based spin valve devices.

Parts of chapters 2, 3 and 4 have been published in [96]–[98]. Results reported in Chapters 5 have been submitted for publication [99]. Parts of Chapter 6 have been published in a conference paper [100] and a detailed journal paper on this topic is under preparation.

1.10 Future Directions

Based on the above-mentioned work, we are planning to explore the following subprojects in the future: (1) MR effects in as-grown MLG on cobalt, (2) MR effects in functionalized graphene/Ni(111) interface and studies on spin filtering, and (3) MR effects in MLG transferred on flexible substrates. The first subproject aims to study the MR effects in as-grown MLG on Co, which is very similar to the MLG on Ni system. Thus, strong CPP-MR effects can be expected in as-grown MLG on Co samples as well. In the next subproject, we are planning to reduce the degree of hybridization at graphene/Ni interface by functionalizing with potassium

(K) ions [101]. After that, a detailed MR study will be performed on the functionalized MLG/Ni system. The MR effect may be tunable by such functionalization process and allow us to study spin filtering effect [33], [92] in graphene based magnetic tunnel junctions (MTJs). In the final subproject, we are planning to study magnetoresistance effects in MLG transferred on various flexible substrates.

More details on these future projects are presented in Chapter 7.

2 CVD GROWTH OF MULTILAYER GRAPHENE (MLG) AND CHARACTERIZATION[3]

2.1 INTRODUCTION

As mentioned in the previous chapter, one of the key motivations of this work is to explore CPP-MR of weakly coupled multilayer graphene since this system can potentially give rise to large interlayer magnetoresistance (ILMR), and this effect has not been reported to date in graphene-based systems. According to previous studies, stack of weakly coupled graphene layers can be synthesized by chemical vapor deposition (CVD) on catalytic substrates [28], [35], [36]. During CVD growth, graphene layers arrange in a randomly oriented fashion with weak interlayer coupling. As a result, the intrinsic electronic properties of individual graphene layers remain undisturbed [37]. This weakly coupled MLG is also known as turbostratic graphite. However, CPP measurements are difficult to perform on these systems due to the reasons mentioned below.

Turbostratic graphite has been synthesized on SiC by thermal decomposition [18], [35], [67], [102], but such samples do not allow direct CPP transport measurements. This is because SiC is an insulator and the as-grown turbostratic graphite needs to be transferred on a conducting surface for CPP measurements. However, SiC is highly resistant to chemical etchants [103]. Therefore the standard wet chemical etching process used to transfer CVD-grown MLG [28], [30], [65], are not useful for these samples. Advanced exfoliation techniques have been developed [104]–[106] to transfer SiC-grown turbostratic graphite on conductive surfaces. However, these exfoliation techniques create voids and defects in the transferred turbostratic graphite [106]. In the CPP measurement geometry, these voids and defects can potentially short top and bottom electrodes. Therefore, such transferred samples are not suitable for CPP measurements.

[3] Parts of this chapter have been published in [96], [97].

MLG can also be grown on copper (Cu) and nickel (Ni) catalysts and these metal catalysts can serve as the bottom electrode. Graphene layers grown on these catalytic substrates are weakly coupled as well, and in these devices, transfer process is not required for CPP measurements. CVD growth on Cu leads to fewer number of graphene layers due to limited solubility of carbon in Cu [71]. However, MLG grown on Cu is generally incorporated with defects at grain boundaries. These defect states are known to be conductive [107] and can effectively short neighbouring graphene layers [56]. CPP charge transport in this case will primarily occur via the conductive defect states instead of interlayer tunneling [8], [56]. In contrast, for Ni catalyst, thicker MLG is obtained due to higher solubility of carbon in Ni. Interestingly, graphene layers in the "bulk" of MLG (i.e. layers away from Ni/MLG interface) show weak interlayer coupling and no structural defect. The in-plane lattice constant in the (111) Ni plane (0.232 nm) matches closely with that of graphite (0.246 nm), allowing continuous growth of graphene layers over the entire Ni surface during the CVD process [28], [30]. Based on these considerations we have chosen Ni as the catalytic substrate for our study. This allows CPP transport experiments on large area, defect-free MLG that contains weakly coupled graphene layers. However, as mentioned in previous chapter (section 1.7), graphene layers at the interface form strong chemical bond with Ni and do not preserve their intrinsic electronic configuration. Therefore, thinner MLG specimens exhibit a Raman *D* peak that originates from the defects at the Ni/MLG interface and the layers close to the interface. Thus, the as-grown MLG on Ni has two distinct regions: (a) Ni/MLG interface and layers close to this interface ("defective region") and (b) layers away from Ni/MLG interface ("defect-free region"). CPP transport characteristics of the "defective region" need to be studied as well to understand the observed MR effects.

In this work, we have fabricated MLG on polycrystalline Ni foil using CVD and have performed CPP-MR measurements on as-grown MLG on Ni. During CVD process, MLG growth occurs over all surfaces of the Ni foil. Therefore, to achieve CPP geometry, MLG on the top surface of the Ni foil is coated with a thin polymer (polymethyl methacrylate) film. Then, MLG is removed from bottom and edges of

the Ni foil by oxygen plasma etching. Later, for control experiments, as-grown MLG is transferred on gold electrodes patterned on SiO_2/Si substrate. Device fabrication therefore consists of four major steps: (1) CVD-growth of multilayer graphene (MLG) on catalytic Ni substrate, (2) oxygen plasma etching of MLG and device patterning and (3) transfer of MLG on SiO_2/Si (Figure 2.1). Finally, the MLG is characterized by optical microscopy, scanning electron microscopy (SEM), step height measurements and Raman spectroscopy. In this chapter we will briefly describe these fabrication and characterization steps.

2.1.1 CVD Growth of Multilayer Graphene (MLG) on Ni

Multilayer graphene (MLG) stack with various thicknesses have been grown on polycrystalline Ni substrates using a standard CVD recipe [28], [30], [65], [66]. Polycrystalline Ni foil (25 μm thick, annealed, 99.5% metal basis, purchased from Alfa Aesar) is used to grow thick multilayer graphene (MLG) stacks (200 – 300 nm). E-beam evaporated Ni thin films (~ 600 nm) are used to grow thinner MLG (15 – 20 nm) stacks. The e-beam evaporated Ni thin films are also polycrystalline in nature. The typical X-ray diffraction (XRD) spectrum of polycrystalline Ni (both foil and thin film) shows a stronger Ni (111) peak and a weak Ni (200) peak (Figure 2.1*inset*). Various groups have used polycrystalline Ni substrates (e-beam evaporated as well as foil) in the past for graphene growth [28], [30], [65], [66].

CVD process flow consists of the following steps: (a) Ni substrate (~ 2 cm $\times$ 2 cm in size) load, (b) furnace purge, (c) temperature ramp to 1000^{o}C and hydrogen anneal for one hour, (d) graphene growth at 1000^{o}C for 10 minutes, (e) natural cooling, and finally (f) unloading of the sample. We have used 0.3% CH_4, 9.7% H_2, and 90% Ar during the growth of graphene. The hydrogen anneal step removes the native oxide layer and any adsorbate from the Ni surface. In case of thick Ni substrate (~ 25 μm), this growth process results in MLG that are characterized by absence of Raman *D* peak and absence of significant splitting in the Raman *2D* peak (as discussed later, Figure 2.7). For e-beam evaporated Ni thin films (~ 600*nm*), the above mentioned CVD process produces 15 – 20 *nm* thick MLG that are characterized by strong Raman *D* peak (as discussed later, Figure 2.9). Optical

microscope images of CVD-grown MLG on both thick and thin substrates are shown in Figure 2.2. To vary MLG thickness from 20 nm to 200 nm, we adjusted carbon species concentration from 0.1 - 0.3% while keeping all other CVD parameters unchanged. At intermediate concentrations of carbon species, we also obtained MLG of thickness ~ 60 nm that exhibit almost identical Raman spectra as 200 nm thick MLG samples. Characterization of 60nm thick MLG samples will be presented in Chapter 5 where these samples are extensively used for angle dependent MR measurements. We also observed that a higher relative concentration of carbon-containing species within the chamber leads to bulk graphite (HOPG-like) growth on the Ni surface (Figure 2.8(a)), which is consistent with the literature [65], [95].

We used atomic force microscopy (AFM) to obtain surface roughness profile of as-grown MLG-on-Ni. A standard tetrahedral silicon tip (Olympus, OMCLAC 160TS-W2) located at the end of silicon cantilever is used for imaging under AC mode with a typical values of force constant, resonant frequency and scan rate of 42 N/m, 300 kHz and 1Hz respectively. The radius of curvature of the tip is < 10 nm. Interestingly, in thick MLG grown on Ni foil, we have observed bulging features at grain boundaries (Figure 2.3). This observation is consistent with ref. [108].

2.1.2 Oxygen Plasma Etching of MLG and Device Patterning

During the CVD process, MLG growth takes place on both sides of the substrate catalyst. To prepare a well-defined device geometry for CPP measurement, we removed MLG from the bottom and side surfaces. For this purpose, a thick protective polymethyl methacrylate (PMMA) layer is coated on the top surface of the MLG, and the sample is subjected to oxygen plasma etching. In this process, the surface uncovered with PMMA is exposed to oxygen plasma (90 Watts) under chamber pressure of 180 – 190 *m*Torr for 10 mins. This process removes MLG from the bottom and side surfaces, and the MLG under the PMMA layer is preserved. We have also prepared and tested several control samples in which the

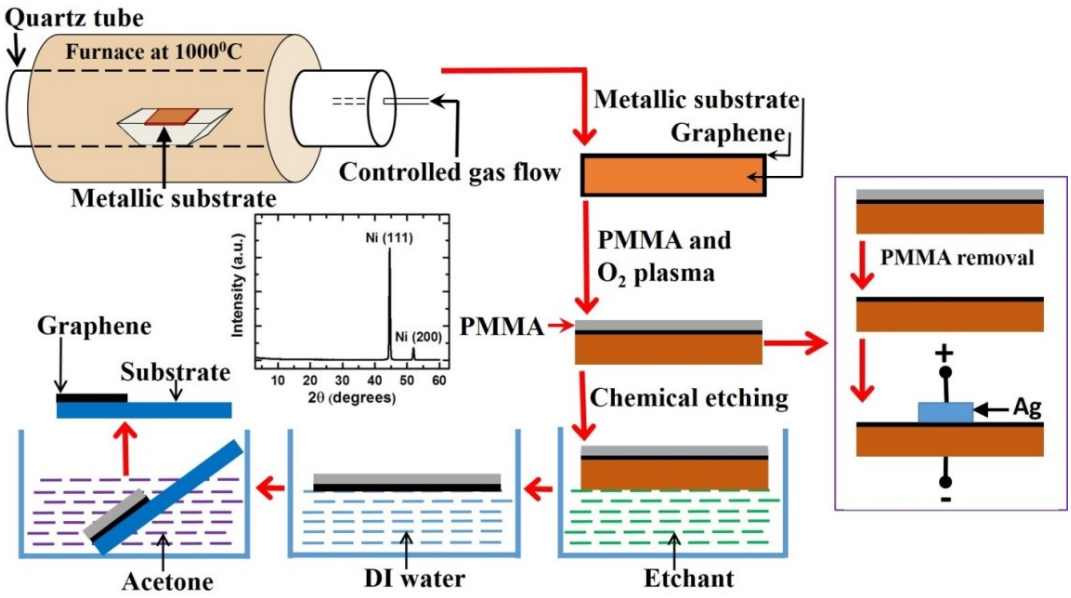

Figure 2.1 Schematic description of the fabrication process. The CVD growth of MLG on Ni; oxygen plasma etching of graphene on the bottom surface; transfer of MLG on SiO_2/Si are depicted in the schematic. Typical XRD spectrum of the polycrystalline Ni substrate used in this work is presented in the *inset*.

CVD-grown MLGs have been transferred on a separate substrate. This has been achieved by chemically etching the metal catalyst. Before this chemical etching step, the above-mentioned oxygen plasma etching needs to be performed, so that the etchant can come in contact with the metal catalyst and initiate the etching process.

2.1.3 Transfer of MLG on SiO_2/Si

The above-mentioned oxygen plasma-etching step removes MLG from back and side surfaces of the Ni foil and exposes it for chemical etching. The Ni foil was then etched away using warm (~ 60°C) ferric chloride ($FeCl_3$) solution. The etching process takes ~ 4 – 5 hours to complete. Etching process in cold $FeCl_3$ solution is less efficient and generally leaves Ni particle residues with PMMA/MLG film even after overnight etching. Upon completion of the etching step, PMMA/MLG composite film floats up in the $FeCl_3$ solution. The PMMA/MLG film was collected and thoroughly cleaned in deionized water. Next, the cleaned PMMA/MLG film was transferred on a SiO_2 (300 nm)/Si wafer. After overnight drying we heated the

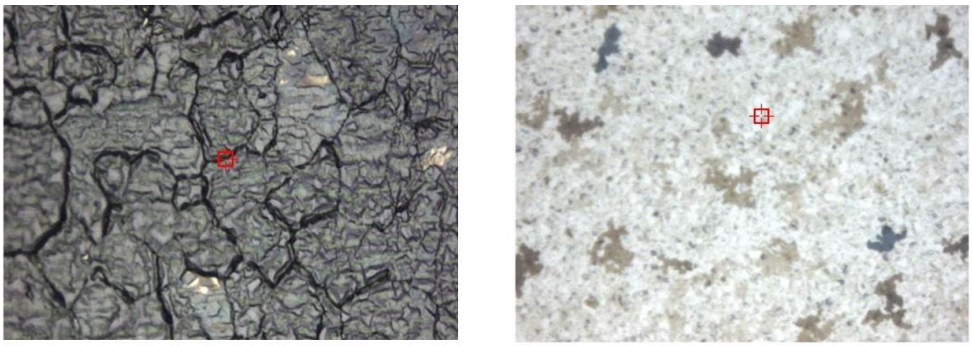

(a) **(b)**

Figure 2.2 Optical microscope images of CVD-grown MLG on Ni. (a) Thick (~ 200 nm) as-grown MLG on 25 μm thick Ni foil. (b) Thinner (15 – 20 nm) as-grown MLG on ~ 600 nm Ni thin film.

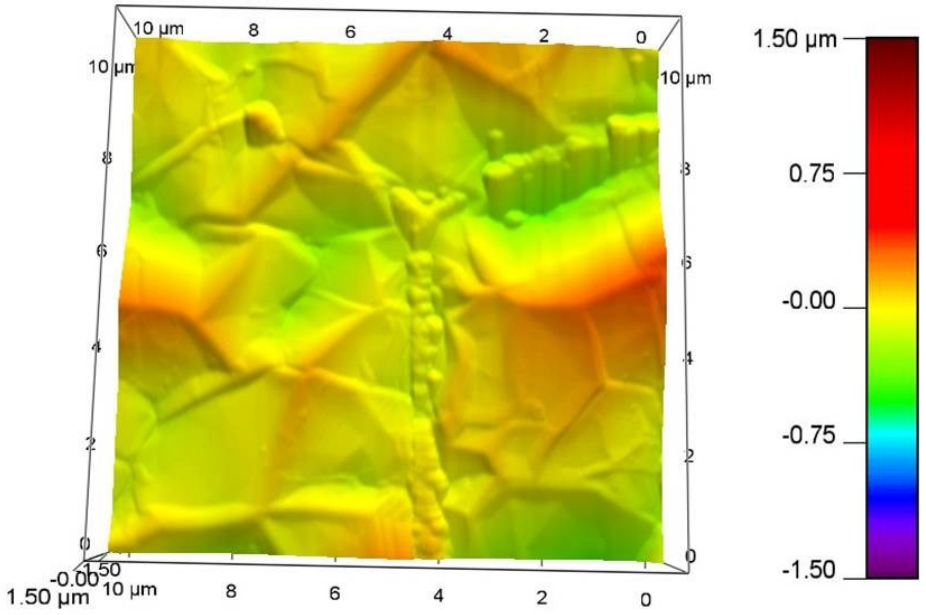

Figure 2.3 Atomic Force Microscopic (AFM) image of CVD-grown MLG-on-Ni.

sample (~ 250^{o} C) in a vacuum oven so that the graphene layer adheres strongly to the SiO_2 surface. Finally, top PMMA layer was dissolved in acetone, which left only MLG layer on SiO_2 surface. We estimated the average number of graphene layers to be ~ 600 (Figure 2.4) from step height measurements using profilometer (Alphastep-200). As shown later, unlike the as-grown MLG, the transferred

samples show HOPG-like Raman 2*D* peak. This implies that interlayer coupling becomes stronger as a result of transfer. This has a significant effect on the CPP-MR characteristics.

Without annealing, the electrical contact (and adhesion) between bottom electrode and transferred MLG was poor and we were unable to get reliable electrical measurements. The transferred MLG films tend to peel off the substrate in absence of annealing. Such poor contact and poor adhesion to the bottom substrate presumably results from water or air molecules trapped in a "dead space" between MLG and the bottom contact. Annealing helps to compress this "dead space" via desorption of such species and significantly improves the quality of the bottom electrical contact (after transfer) but also destroys the weak interlayer coupling. Improvement of surface adhesion upon annealing has also been observed by other groups [84], [109].

There are other advantages of post-transfer annealing as well. For example, annealing is often used to desorb and decompose the chemical (primarily PMMA) residues that remain on graphene as a result of the transfer process [109]–[111]. Such residues cause unintentional doping of the graphene layers and result in a shift of the Fermi level from the Dirac point. Since ILMR is primarily due to interlayer tunneling between the zero mode Landau levels that are located at the Dirac points, such doping-induced shift of the Fermi levels from Dirac points is undesirable. Annealing is necessary to avoid this effect.

The transfer process is slightly different for thinner MLGs (~ 15 – 20 nm) grown on Ni thin film samples compared to thicker MLG grown on Ni foil samples. Since Ni thin film is deposited on SiO_2/Si substrate, the bottom surface is not exposed for etching. As an alternative, the central region of as-grown MLG is covered with thick PMMA coating, and the outer region around the PMMA coated area is exposed for plasma etching. Then the sample is dropped in $FeCl_3$ etchant. During the etching of Ni substrate, PMMA/MLG attaches to the SiO_2/Si substrate. We used

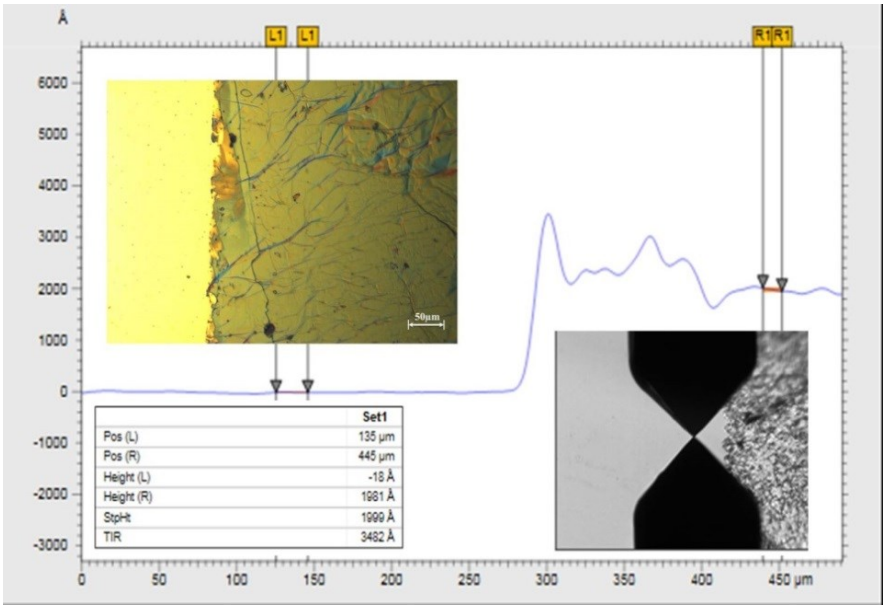

Figure 2.4 Thicker MLG transferred on SiO_2/Si. Step height measurement of transferred MLG on SiO_2/Si using profilometer (Alphastep-200). Average thickness of transferred MLG is ~ 200 nm. *Insets* show optical image of transferred MLG on SiO_2/Si.

sodium hydroxide (NaOH) solution which slightly etches SiO_2 and releases PMMA/MLG in the solution. The PMMA/MLG floating in NaOH solution is transferred into water and finally to another clean SiO_2/Si substrate. Finally, top PMMA layer was dissolved in acetone, which left only MLG layer on SiO_2 surface. The step height of transferred MLG is measured using AFM as shown in Figure 2.5.

2.2 Raman Characterization of Synthesized MLG

Raman spectroscopy is an effective non-destructive tool, which can be used to shed light on layer arrangements and interlayer coupling in MLG samples. We used Raman spectroscopy to highlight the differences between as-grown MLG, transferred MLG on SiO_2/Si and commercial samples.

All Raman spectra in this work have been acquired at room temperature using a Nicolet Almega XR Micro and Macro Raman Analysis System. Laser wavelength is set to 532 nm (2.33eV). Maximum power is set to 24mW, 100% of which has been used for all studies. No evidence of laser-induced heating has been found in

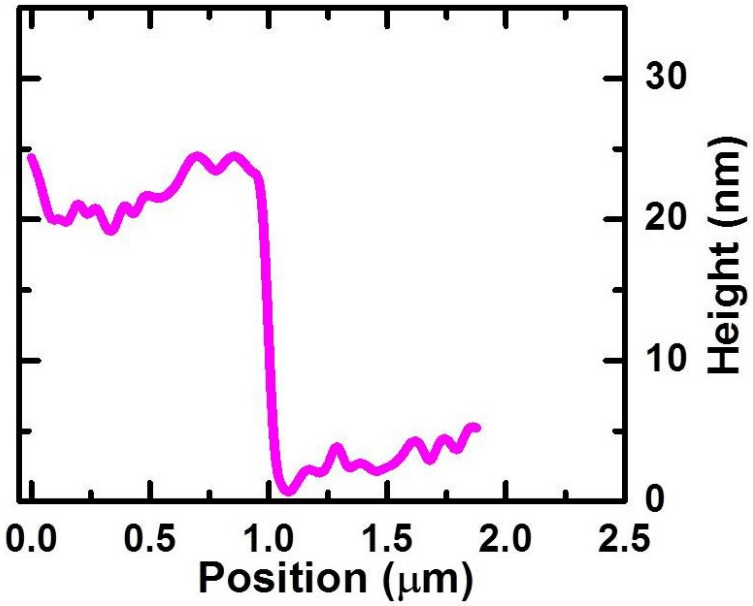

Figure 2.5 Thinner MLG transferred on SiO_2/Si. Step height measurement of transferred MLG on SiO_2/Si using Atomic Force Microscope (AFM). Average thickness of transferred MLG is ~ 15 – 20 nm.

any case. We note that the typical penetration depth of Raman laser into graphite is ~ 50-100 nm [84], [112]–[114], whereas total MLG thickness is 200 nm. Hence the Raman spectra reported in this work convey information about the layers away from MLG/Ni interface. For the purpose of comparison with the Raman spectra of CVD-grown MLG samples, we collected Raman spectrum of *HOPG* (SPI supplies, SPI-1 grade, 10 x 10 x 1 mm) as our reference spectrum (Figure 2.6). *G* and *2D* peaks of HOPG occur at ~ 1580 cm^{-1} and ~ 2718 cm^{-1} respectively. The 2*D* peak is asymmetric and consists of two shifted Lorentzian components and the higher intensity component appears at higher frequency side (Figure 2.6 *inset*). MLG samples extracted from HOPG typically consist of a layers that are Bernal stacked. Bernal stacked graphene layers are generally well ordered and strongly coupled compared to other layer arrangements. As discussed in section 1.6 in chapter 1, this strong coupling is responsible for the observed asymmetric Raman *2D* peak (Figure 2.6 *inset*).

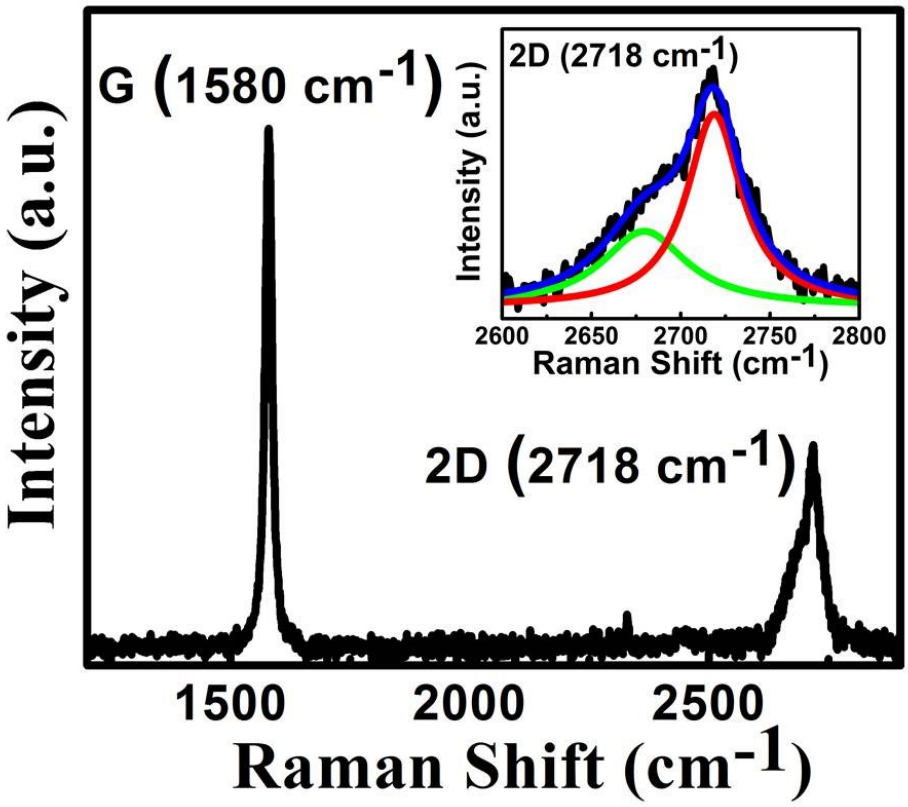

Figure 2.6 Raman spectrum of HOPG (SPI supplies, SPI-1 grade). The Raman 2D (2718 cm^{-1}) is asymmetric and consists of two shifted Lorentzian components (red and green lines in *inset*). The higher intensity component (red line) appears at higher frequency side.

2.2.1 Raman Spectra of MLG on Ni

As mentioned before, we primarily studied thick MLG (60 – 200 nm) as grown on Ni and thin MLG (~15 – 20 nm) as grown on Ni. The thin MLG is characterized by symmetric 2*D* band and presence of *D* band. For thick MLGs, *D* band is absent everywhere in the sample, implying that graphene layers close to the top surface are free from structural defects. Depending on growth conditions, thicker MLG samples can show either symmetric 2*D* peak or HOPG-like split 2*D* peak. These Raman features reveal key properties of the MLG. In this section, we present Raman spectra of above-mentioned categories of CVD-grown MLGs.

2.2.1.1 Case 1: Thicker MLG (~200 nm) Showing Symmetric 2*D* Band and no *D* Band

Raman spectra taken from various regions of as-grown MLG on Ni substrate are shown in Figure 2.7. The top Raman spectrum (black line) is most commonly observed, with few occurrences of the other two (blue and red). The strong *G* peak (1580 cm^{-1}) indicates formation of hexagonal lattice of carbon atoms. The 2*D* peak (2700 cm^{-1}) is weaker compared to the *G* peak. The line width (full width at half-maximum) of 2*D* peak is wider (~ 50 cm^{-1}) than that of single layer graphene (~ 35 cm^{-1}) and its position (2700 cm^{-1}) is slightly upshifted compared to single layer graphene (~ 2690 cm^{-1}) [28]. These features indicate presence of multiple graphene layers [28], [34], [73]. Previously mentioned step-height measurement is consistent with this observation (Figure 2.4). The disorder-induced "*D*-band" at 1350 cm^{-1} is

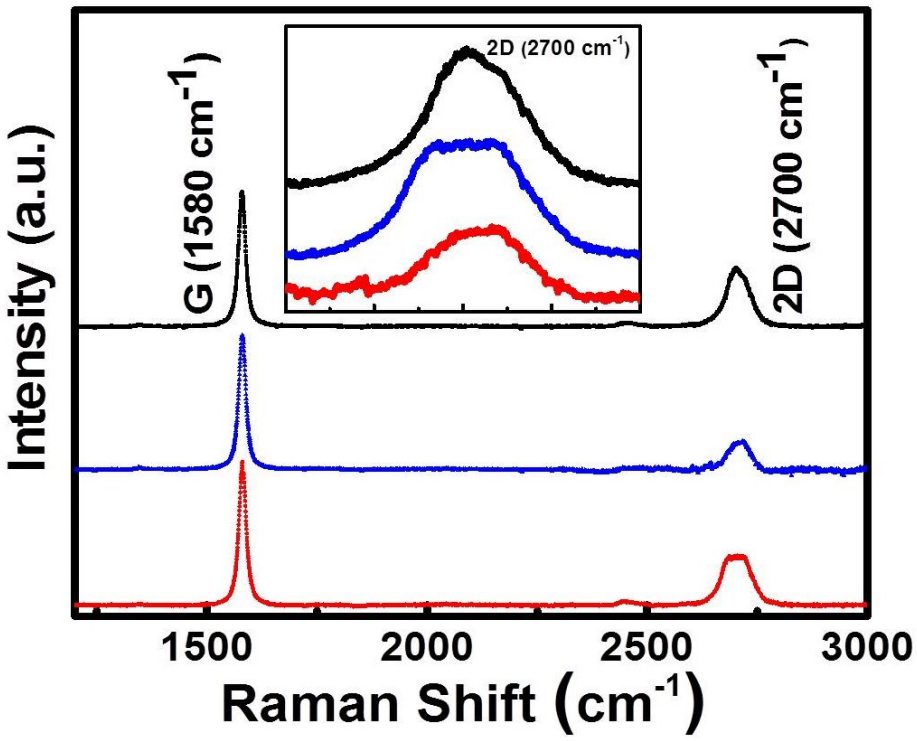

Figure 2.7 Raman Spectrum of CVD-grown MLG on Ni Sample in Case1. The Raman spectra have been taken from three representative areas of the MLG on Ni sample. The 2*D* bands do not show HOPG-like "shoulder" peak or any significant splitting. The *D* peak is not present anywhere. The top Raman spectrum (black line) is most commonly observed, with few occurrences of the other two (blue and red).

strongly suppressed in all regions, which indicates extremely low density of structural defects in the layers close to the top surface. We note that no *D* band has been found in any area of the sample. Unlike HOPG (Highly Oriented Pyrolytic Graphite), the *2D lineshape* of the as-grown MLG samples does not exhibit any clear "shoulder" peak at the lower frequency side of the *2D* band or any pronounced "splitting" (Figure 2.7). Such absence of "shoulder" peak and splitting has been observed before in CVD-grown MLGs and turbostratic graphite [28], [34]–[36].

From the Raman spectra, we note that there are minor variations in the 2*D* line shape, which indicates interlayer coupling may not be uniform over the sample surface. We have also studied ~ 60 nm MLG samples, which show similar Raman features as ~ 200 nm samples. Specific details on ~ 60 nm samples are provided in Chapter 4.

2.2.1.2 Case 2: Thicker MLG (~200 nm) Showing Distorted 2*D* Band and no *D* Band

We have synthesized MLG on Ni that exhibits HOPG-like shoulder peak in the Raman *2D* band (Figure 2.8 (a)). This has been done by controlling the CH_4:H_2 ratio during CVD growth process. Thickness of MLG in this sample is ~ 200 *nm*, which is similar to the sample in Figure 2.7. Even at grain boundaries, Raman spectroscopy shows features that are very similar to the regions within the grain boundaries. These features bear close resemblance to the HOPG Raman features (Figure 2.6).

Figure 2.8(b) shows Raman spectroscopy performed on commercially available MLG/Ni samples (Graphene Supermarket). The thickness of MLG in these samples is ~100 nm. Again, the *2D* peaks in these samples show pronounced splitting and they can be fitted with two Lorentzian peaks (Figure 2.8 *inset*). As discussed in chapter 1 (section 1.6), splitting and distortion in 2*D* peak indicate strong interlayer coupling similar to HOPG samples. The defect peak (*D* peak) is absent in these samples (Figure 2.8 (a), (b)).

2.2.1.3 Case 3: Thinner MLG (~15 – 20 nm) Showing Presence of *D* Band and Symmetric 2*D* Band

As mentioned before, we have grown thinner MLG (~ 15 – 20 nm) using Ni thin film (~ 600 nm) as substrate catalyst. CVD growth parameters are same as those reported in section 2.1.1. The only parameter that has been changed to obtain thinner MLG is the thickness of the Ni substrate. Growth of fewer number of layers in this case is presumably due to reduced dissolution of C atoms in thin films compared to bulk foil. Adjusting the substrate thickness is expected to introduce minimum perturbation in the growth process as compared to changing the CVD growth parameters.

These thinner MLG samples exhibit significant defect (*D*) peak at ~1350 cm^{-1} in Raman spectrum (Figure 2.9). This *D* peak originates from the defects at the Ni/MLG interface and layers close to the interface ("defective region"). As discussed before (section 1.7 in Chapter 1) these defects are due to strong hybridization between $2p_z$ orbitals of interfacial graphene and 3*d* orbitals of Ni [85].

2.2.2 Transferred MLG on SiO_2/Si

We have also transferred CVD-grown MLG on SiO_2/Si substrate and have performed Raman spectroscopy. Unlike as-grown MLG (Figure 2.7), the *2D* band in the Raman spectrum in this case resembles HOPG-like *2D* band with a shoulder in the lower frequency range of the band (Figure 2.10 *inset*). Such change in Raman characteristics has been observed before by other groups [30], [65], [115], and can be attributed to the previously mentioned thermal processing steps (section 2.1.3) involved in the transfer process.

Annealing or heat treatment indeed causes "graphitization" of turbostratic graphite. For example, ref.[115] started out with a turbostratic graphite sample in which the *2D* peak is symmetric and does not show any splitting. For this sample, interaction between the basal planes is weak enough so that the splitting in the π electrons' dispersion energies does not occur resulting in a single Lorentzian in the *2D* band.

However after heat treatment, the *2D* band resembles the shoulder-like shape of HOPG, indicating splitting of the π electrons' dispersion energies. Such splitting

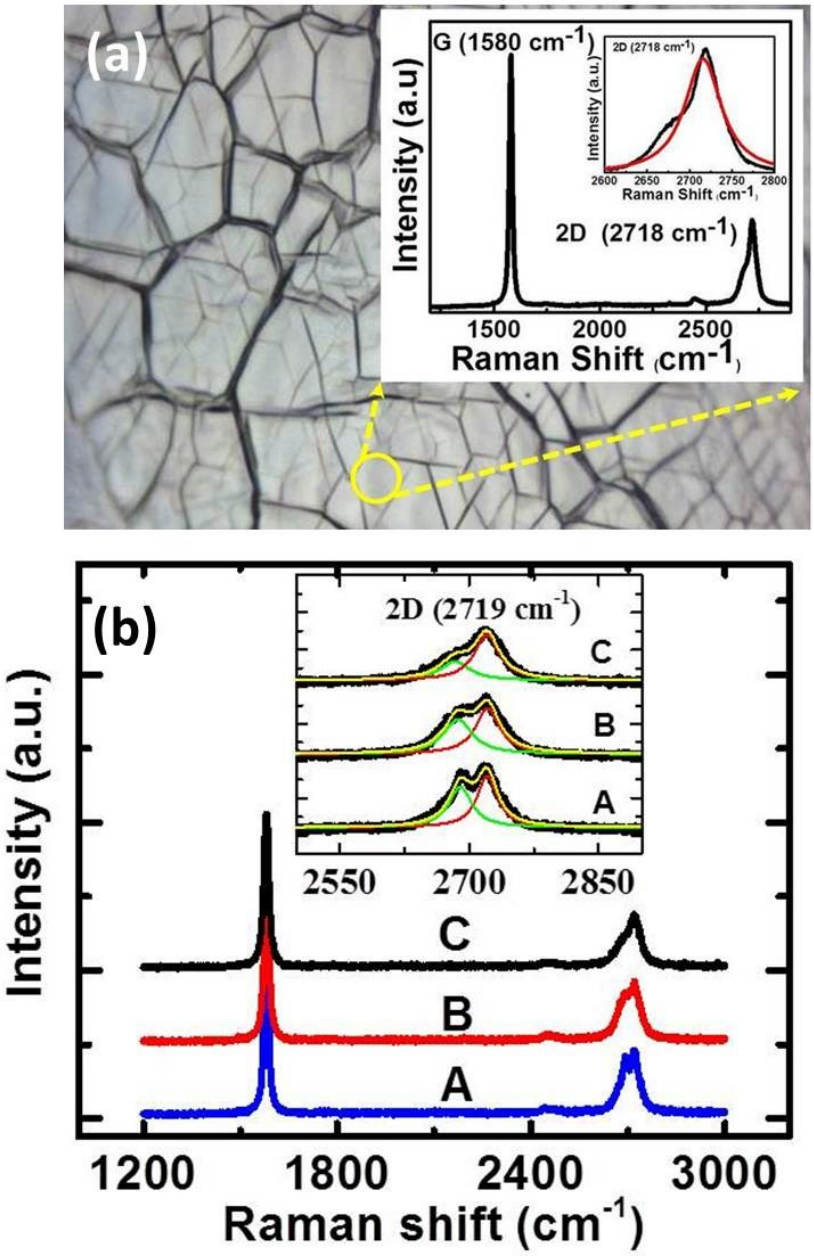

Figure 2.8 Raman spectra of CVD-grown MLG on Ni Samples in Case 2**.** MLG thickness is ~ 200 nm (Figure (a)) and ~ 100 nm (Figure (b)). (a) Raman spectrum of HOPG-like sample CVD-grown on Ni. The *2D* band in the Raman spectrum shows a shoulder peak (*inset*). (b) Raman characteristics of commercial MLG/Ni samples (from Graphene Supermarket). The 2*D* band in the Raman spectra shows pronounced splitting.

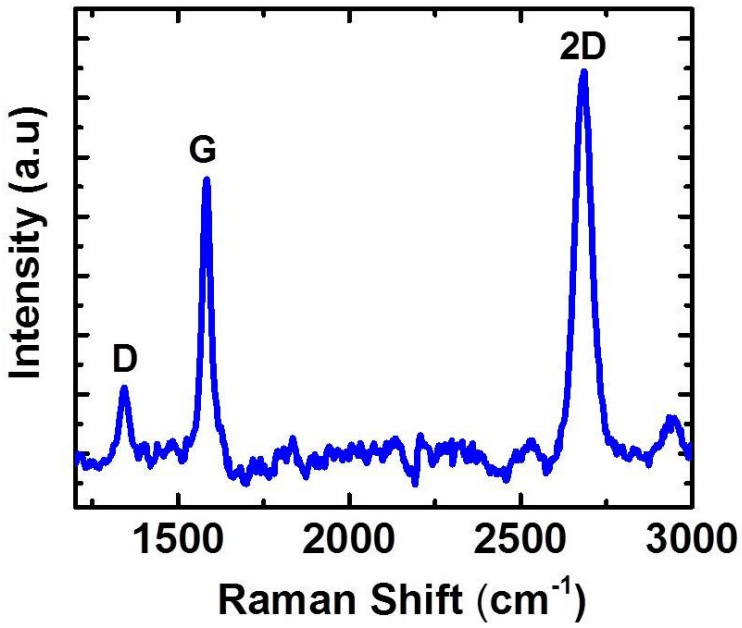

Figure 2.9 Raman Spectrum of CVD-grown MLG (~ 15 – 20 nm) on Ni Thin Film (~ 600 nm) Sample in Case 3. A clear *D* peak can be observed at ~ 1350 cm^{-1}, which was not present in thicker specimens.

indicates presence of significant interlayer coupling as compared to the starting turbostratic sample. Presumably, the heat treatment gives rise to planar rearrangement of the carbon atoms, which stabilizes to stronger interlayer coupling (Bernal stacked) configuration after the sample is cooled. Our observation is consistent with this work because during the transfer process we have used high temperature (250ºC) vacuum annealing to achieve substrate adhesion and reliable electrical measurements.

2.2.3 CVD-grown MLG on Cu

We have performed Raman spectroscopy on commercially available MLG (~ 8 layers) that are CVD-grown on Cu substrates (ACS Materials). Samples grown on copper typically show symmetric 2*D* Raman band (Figure 2.11, *inset*). These samples also exhibit significant defect peak (~1360 cm^{-1}, Figure 2.11) at grain boundaries (bottom scan, red line). The edge states at the grain boundaries are known to be conductive [107] and can effectively short the neighbouring graphene layers. Other groups have also reported Raman defect (*D*) peak at grain boundaries of CVD-grown MLG on Cu [90].

In the next chapter, we will describe the MR measurements performed on various CVD-grown MLG samples. The MR response has been found to be correlated with various Raman features reported in this chapter.

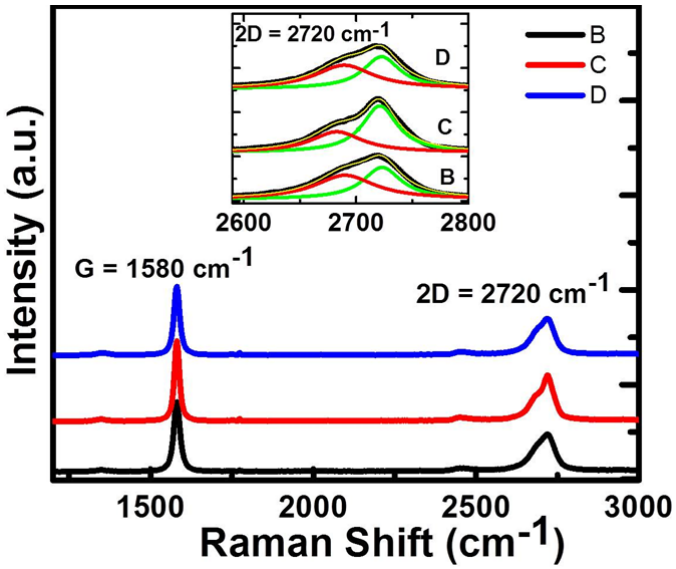

Figure 2.10 Raman Spectra of MLG Transferred on SiO_2/Si. A HOPG-type distorted 2*D* band is observed.

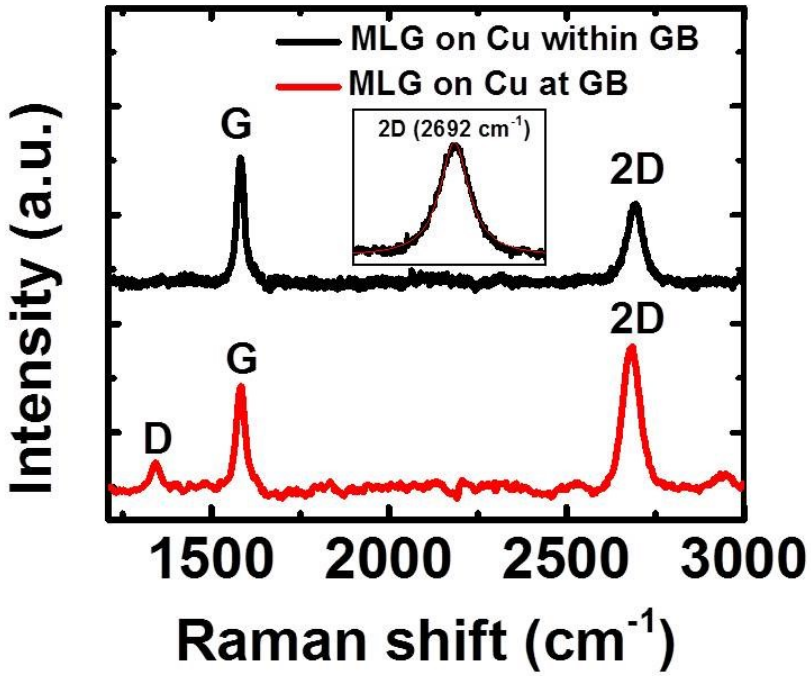

Figure 2.11 Raman Characteristics of CVD-grown MLG (~ 8 layer) on Copper (ACS Materials). The 2*D* peak is symmetric and can be fitted with a single Lorentzian (*inset*). The bottom scan (red line) is taken from the grain boundary (GB) region, which shows a significant defect (*D*) peak at ~1360 cm^{-1}.

3 MAGNETORESISTANCE (MR) MEASUREMENTS ON CVD-GROWN MLG[4]

In this work, one of our aims is to explore CPP-MR behavior of as-grown MLG on Ni substrate. As discussed before in chapter 2, we primarily studied thick MLG (~ 200 nm) as grown on Ni and thin MLG (~15 – 20 nm) as grown on Ni. We have also studied ~ 60nm thick MLG, which is similar to ~ 200 nm samples. Data from ~ 60nm samples are presented in Chapter 4. Based on Raman spectra, these samples are categorized into three classes: (1) thicker MLG (~ 200 nm) showing symmetric 2*D* band, (2) thicker MLG (~ 200 nm) showing distorted 2*D* band, and (3) thinner MLG (~15 – 20 nm) showing presence of *D* band and symmetric 2*D* band. The thicker MLG samples do not exhibit any Raman defect (*D*) peak. In this chapter, we first present MR effects observed in above-mentioned three classes of samples and then provide a detailed discussion on the physical origin of the observed MR effects.

The device fabrication processes for all three classes of samples have been clearly described in Chapter 2 (section 2.1.1). For CPP measurements, the bottom Ni (111) substrate acts as one of the contacts and to assure uniform current distribution, the other contact is fabricated at the center of the top MLG surface using silver epoxy. The device schematic is shown in Figure 3.1(a). As discussed later, contact resistance at Ni/MLG interface and Ag paste/MLG interface have been found to have negligible effect on the overall CPP resistance (R_{ZZ}). Typical contact area is ~1 mm^2. R_{ZZ} is measured between these two contacts by a conventional two-wire dc method. The combined resistance of the contacts and the interconnecting wires is at least two orders of magnitude smaller than the minimum device resistance and does not exhibit any measurable magnetoresistance. This has been confirmed by directly connecting silver epoxy over Ni substrate and collecting MR data. To further understand the observed MR effects, we have conducted similar MR

[4] Parts of this chapter have been published in [96], [97].

measurements on multiple control samples, which are discussed later in this chapter.

For magnetoresistance (MR) measurements, Model 642 electromagnet power supply and Cryotronics 332 Controller (Lakeshore) have been used as electromagnet current source and temperature controller respectively (Figure 3.1 (b)). Picotest M3500 multimeter has been used to extract directly the resistance of the device. Each resistance value is the average of 50 readings. The measured resistance values have been independently validated by a Keithley Model 2636 dual-channel system source meter. A 475 DSP gauss meter has been used to record the magnetic field values. All equipment have been synchronized by LabView VI for data acquisition.

3.1 CPP-MR of CVD-grown MLG on Ni

We have performed CPP-MR measurements on above-mentioned three classes of as-grown MLG on Ni samples. For thick MLG (~ 200 nm) samples (case 1 and case 2), *D* band is absent everywhere, implying that graphene layers close to the top surface (within the Raman laser penetration depth of 50 – 100 nm), are free from structural defects. This region is labeled as "defect free region". In case 1, Raman2*D* band is symmetric indicating weak interlayer coupling between graphene layers in the defect free region. However, in case 2, 2*D* band is distorted, which represents strong interlayer coupling between graphene layers in the defect free region. Finally, for thinner MLG (~15 – 20 nm) samples defect (*D*) peak is present and 2*D* peak is symmetric. CPP-MR data for all samples have been collected at a constant current bias (~ 1 mA). CPP-MR have been found to be correlated to Raman spectra.

3.1.1 Case 1: CPP-MR of Thicker MLG (~200 nm) Showing Symmetric Raman 2*D* Band and no *D* Band

CVD-grown thicker MLG (~200 nm) on Ni, which shows symmetric 2*D* and no *D* band in Raman spectrum, is the primary sample of our study. Figure 3.2 shows the magnetic field (*B*) dependence of the "current-perpendicular-to-plane" (CPP)

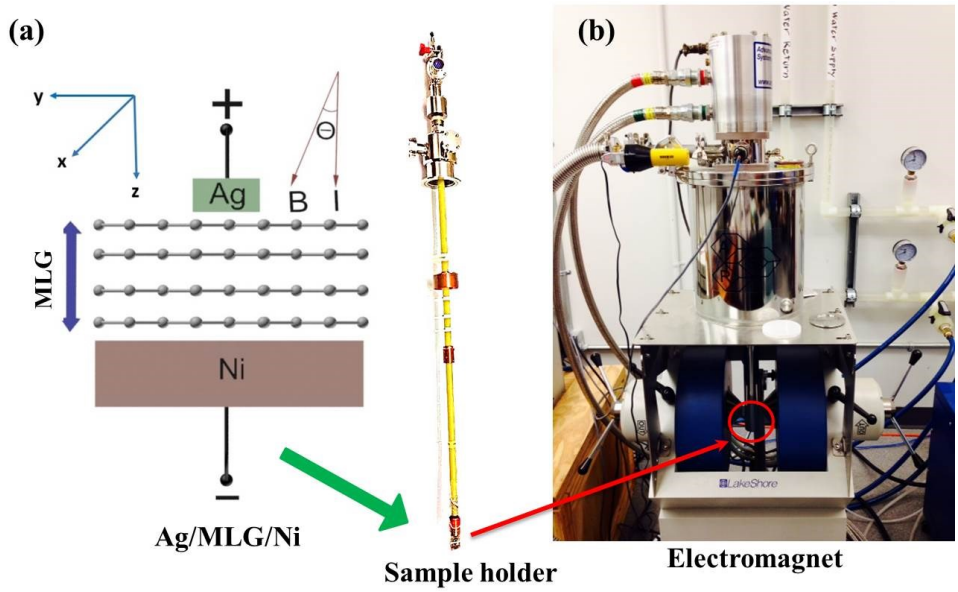

Figure 3.1 Device Schematic and Magnetoresistance (MR) Measurement Setup. (a) Measurement geometry. The MLG (*xy* plane) is grown on the bottom Ni substrate by CVD. (b) Sample is mounted on the sample stick for low temperature measurements. Magnetic field is generated by the electromagnet as shown in figure.

resistance (R_{zz}) at various temperatures (T). CPP-MR depends strongly on the direction of the magnetic field. For "B in plane" geometry ($B \perp I$ or, $\theta = \pi/2$ in Figure 3.1(a)), a weak positive MR[5] of ~ 3% or less is observed (insets of Figure 3.2), which gradually becomes weaker as the temperature is increased. However, in "B normal to plane" geometry ($B \parallel I$ or, $\theta = 0$ in Figure 3.1(a)), resistance decreases drastically as B is increased and this negative MR persists over the entire temperature range of 10 – 300K. We note that the amount of resistance change is extremely large, ~ 2 orders of magnitude over a moderate field range of ~ 2 kG. Semi classical models do not predict such effects since Lorentz force on charge carriers is zero in $B \parallel I$ configuration. Multiple devices (~ 30) have been tested and large resistance change (minimum by a factor of 2, i.e. MR ~ 10^2%) has been recorded in most cases (~ 20) [97].

[5] MR = $\frac{[R_{zz}(11\ kG) - R_{zz}(0\ G)]}{R_{zz}(11\ kG)} \times 100\%$

To gain further insight into the CPP charge transport we have performed temperature and magnetic field dependent current-voltage (*I – V)* measurements on the sample of Figure 3.2. This data is presented in Figure 3.4. Previous works have modeled CPP transport as a combination of in-plane (*x*-*y*) charge transport in constituent layers, and phonon- or impurity-assisted interlayer (*z*) charge transfer [8], [116], [117]. For a disorder-free system, the latter exhibits insulator-like temperature dependence ($\mathrm{d}R_{zz}/\mathrm{d}T < 0$) [116], [117]. In-plane resistance ($R_{in-plane}$), on the other hand, has a metal-like temperature dependence ($\mathrm{d}R_{in-plane}/\mathrm{d}T > 0$) [116], [117]. However, recently it has been shown that in-plane resistance of CVD-grown and transferred graphene can also exhibit insulator-like temperature dependence [118]. As shown in Figure 3.3, we observe an insulating behavior of the CPP resistance in our samples. As shown later in Figure 3.9 (c), in-plane resistance in our samples also exhibits insulating behavior, which is consistent with ref. [118].

However as shown later in Figure 3.9, in-plane resistance does not exhibit any strong negative MR effect in presence of an out-of-plane magnetic field. Instead, it only shows a weak positive MR effect (Figure 3.9 (b)), which is consistent with previous studies [52]. In-plane transport in graphene nanoribbons can lead to large negative MR in presence of an out-of-plane magnetic field [119]–[121]. However, this effect occurs over a field range of several Teslas and is qualitatively different than the MR effects reported in Figure 3.2. Thus the in-plane charge transport component is not dominant in the measured CPP resistance and the large negative MR observed in Figure 3.2 must originate from interlayer charge transport (along $\hat{z}$) between the graphene layers. We note that the insulating behavior of CPP resistance (or, R_{zz}) in Figure 3.2 persists both under zero field and high field conditions (Figure 3.3), which excludes "magnetic field induced metal-insulator transition" [9] as the possible mechanism behind the observed large CPP-MR effect. Ref. [118] reported a positive CPP-MR in graphitic samples, which is associated with metal-insulator transition. Here, on the other hand, we observe a

negative CPP-MR and our devices remain insulating over the measured magnetic field range (Figure 3.3).

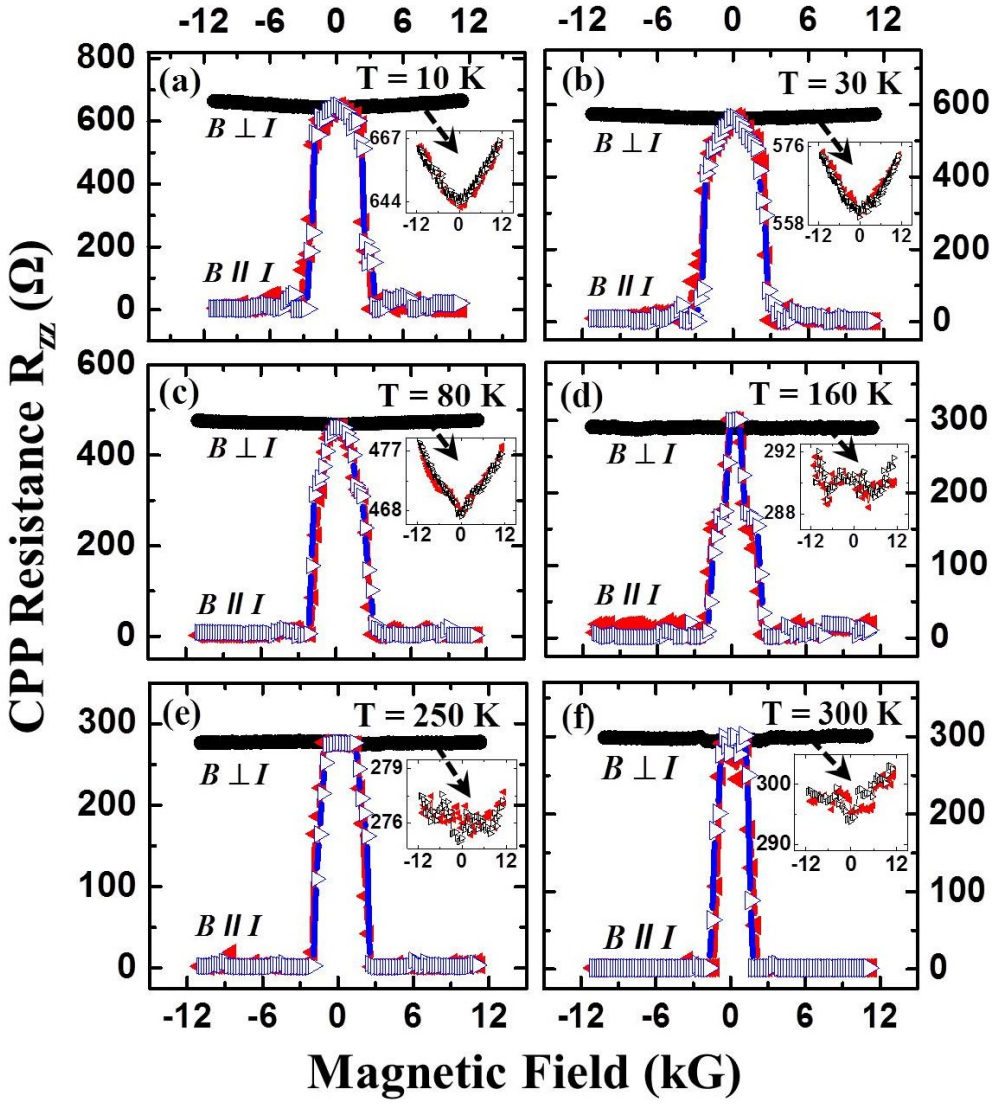

Figure 3.2 Magnetic Field Dependence of CPP Resistance (R_{zz}) in the Temperature Range 10 – 300*K* for MLG/Ni Samples in Case 1. For each temperature two orientations of the magnetic field have been considered: (i) $B \parallel I$ ($\theta = 0$) and (ii) $B \perp I$ ($\theta = \pi/2$). Giant negative magnetoresistance is observed in $B \parallel I$ configuration whereas in $B \perp I$ geometry weak positive magnetoresistance is recorded (insets), which becomes less pronounced at higher temperatures. Both scan directions are shown in each plot, indicating absence of any hysteresis. Each resistance value is the average of 50 readings. For $B \parallel I$, minimum resistance (occurring at high fields) is ~2 – 4 Ω as shown later in Figure 3.3. In all cases, bias current is 1mA dc.

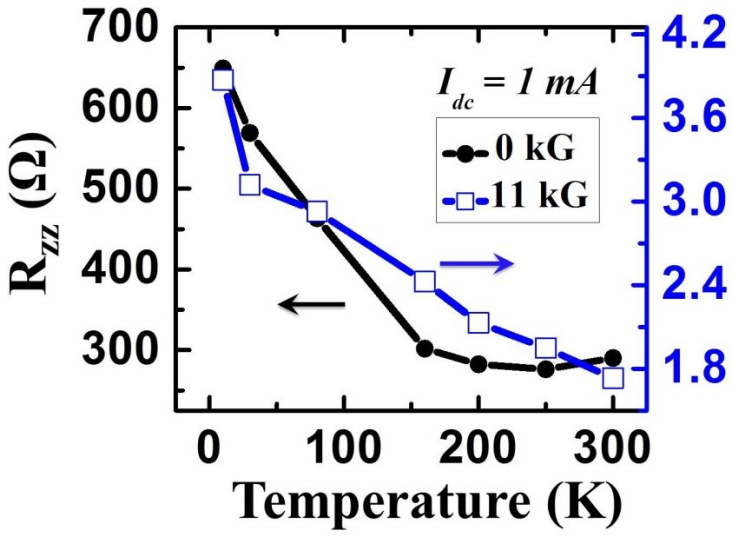

Figure 3.3 CPP Charge Transport Characteristics of Samples in Case 1**.** R_{zz} (T) at zero field and high field (11kG) indicate insulating behavior and absence of any field induced metal-insulator transition.

To gain further insight into CPP charge transport we have performed: (a) current-voltage ($I - V$) measurements in the CPP geometry, and (b) CPP-MR measurements on transferred MLG samples.

(a) I – V Characteristics

The current-voltage (I-V) characteristics are linear (Figure 3.4) over a bias range of [–1 mV, 1 mV], which indicates that MR is independent of bias at least in $\pm$1 mV range. The zero-field I –V characteristics are also linear in this bias range as shown in Figure 3.4 (b). Thus, "magnetic field induced shifting of current path" appears to be an unlikely mechanism behind the observed MR effect. Further, as mentioned before such mechanism is virtually ineffective in the B || I geometry due to the absence of Lorentz force. This mechanism is strongest in the $B \perp I$ geometry, but we have observed significantly weaker MR in this case (Figure 3.2, insets). We note that similar linear $I - V$ characteristics have been reported before for c-axis transport in multilayer graphene stacks [8]. Resistance values measured at a higher current bias (1mA, Figure 3.2) match reasonably well with the slopes of the $I - V$ curves in Figure 3.4. Thus, it appears that the linearity of the $I - V$ curves is maintained over a relatively wide current bias of 1mA. We avoid applying even

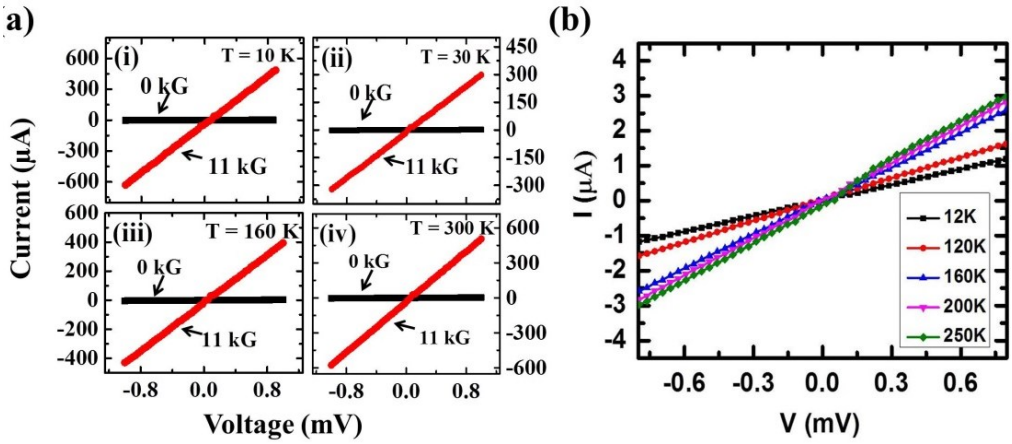

Figure 3.4 *I – V* Characteristics of Samples in Case 1. (a) *I – V* characteristics of MLG/Ni samples at four different temperatures, indicating bias independence of the CPP-MR in ±1 mV range. For zero magnetic field, current is ~ few μA at 1mV bias. (b) A zoomed-in image of the zero-field *I – V* data is presented.

larger bias in order to prevent sample damage due to large out-of-plane electric field in the CPP geometry.

(b) CPP-MR in Transferred MLG

We have transferred Ni-grown MLG presented in case 1, on Au and Ni contacts patterned on SiO_2/Si and have performed CPP-MR measurements. The transferred MLG has shown only a weak positive MR (Figure 3.5) and no large negative MR. As noted before, in the transferred graphene, the Raman 2*D* peak is slightly

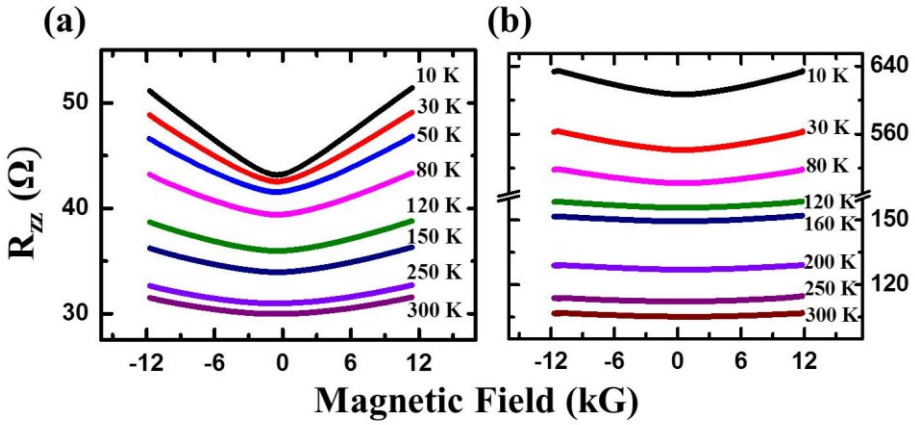

Figure 3.5 CPP MR of MLG Transferred on Au and Ni Electrodes. (a) CPP-MR of MLG (Ni-grown) transferred on Au contact and (b) CPP-MR of MLG (Ni-grown) transferred on Ni contact. Unlike as-grown MLG, the transferred MLG exhibits shoulder peak in Raman 2*D* band (Figure 2.10).

distorted (Figure 2.10) and no negative MR has been observed in this case. As discussed before (Chapter 2, section 2.1.3), such change in 2*D* Raman peak occurs due to the thermal treatments involved in the transfer process. No weak-localization related negative MR has been observed due to presence of larger number of graphene layers. This is consistent with ref. [34].

3.1.2 Case 2: Thicker MLG (~ 200 nm) Showing Distorted Raman 2*D* Band and no *D* Band

We have grown MLG samples of similar thickness (~ 200 nm, on Ni) that exhibit HOPG-like shoulder peak in the Raman 2*D* band of the "defect-free region" (Figure 2.8 (a)), by controlling the CH_4:H_2 ratio during CVD [95]. Such samples have not shown any negative CPP-MR, but showed positive CPP-MR instead, with magnetic field-dependent metal-insulator transition (Figure 3.6 (a)). These features are consistent with prior CPP measurements performed on HOPG [9]. Further, we have performed CPP measurements on commercially available thick (~100 nm) MLG on Ni (Graphene Supermarket). The 2*D* Raman bands from the "defect-free region" of these samples exhibit pronounced splitting (Figure 2.8 (b)) and these samples show weak positive MR (Figure 3.6 (b)) and no negative MR is observed.

3.1.3 Case 3: Thinner MLG (~15 – 20 nm) Showing Presence of Raman *D* Band and Symmetric 2*D* Band

To explore the role of the Ni/MLG interface and nearby graphene layers, we have studied Ni-grown MLG samples, in which the thickness of MLG is ~ 15-20 nm (Figure 3.7). CVD growth conditions have been kept the same as before (Chapter 2, section 2.1.1). Smaller thickness of Ni substrate (~ 600 nm, e-beam evaporated) has been used in this case to obtain thinner MLG. These thinner specimens show a pronounced defective (*D*) peak and a symmetric 2*D* peak in the Raman spectrum (Figure 2.9). We have only observed a very weak positive CPP-MR (~ 0.3%) response from this "defective region" (Figure 3.7). This indicates that the large negative CPP-MR effect reported in Figure 3.2 does not directly originate from the "defective region" close to the Ni/MLG interface. The "defective region" also exhibits weak metallic temperature dependence of CPP resistance (Figure 3.7 (b)),

which is opposite of what is observed in the thicker specimens (Figure 3.3). The resistance of Ni contact itself is ~ 1% of overall CPP resistance and it does not exhibit any measurable MR (Figure 3.8).

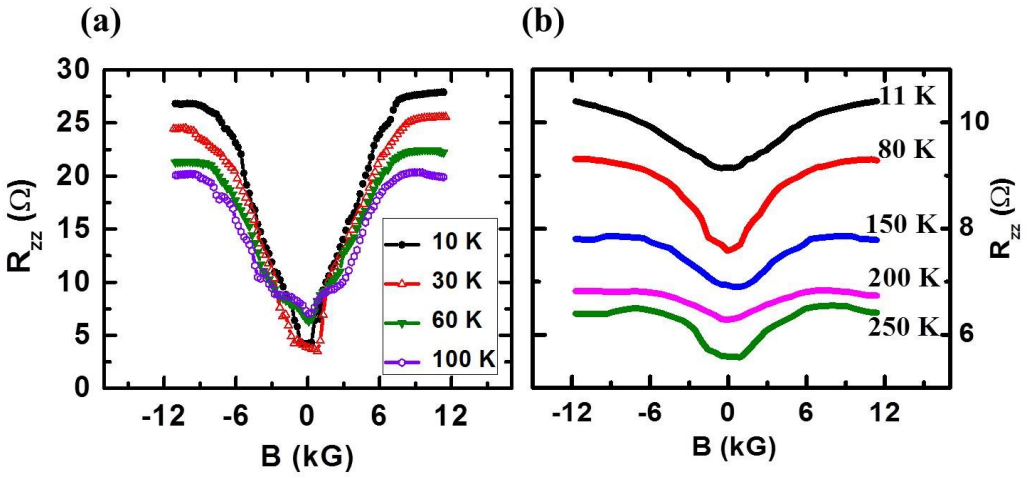

Figure 3.6 CPP-MR of samples in Case 2. (a) R_{zz} vs. B in the $B \parallel I$ geometry. A metal-insulator transition is observed near ~1kG. (b) CPP-MR of commercial MLG/Ni samples (from Graphene Supermarket).

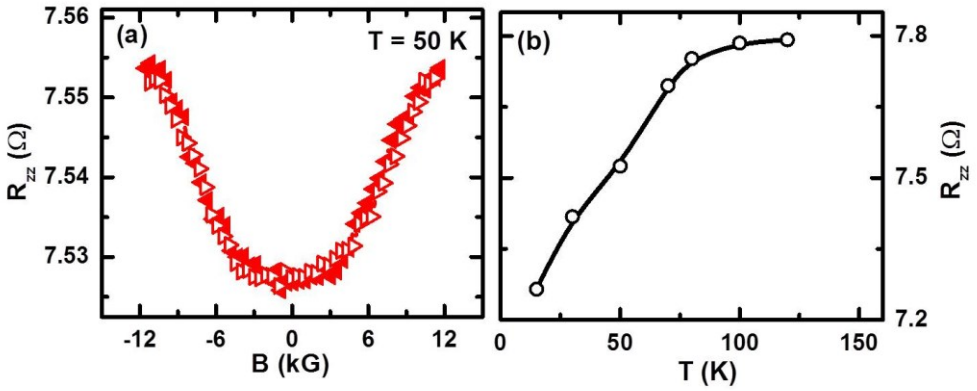

Figure 3.7 Charge Transport Characteristics of Samples in Case 3. (a) CPP-MR of thinner (~15 – 20 nm) MLG samples. (b) Metallic temperature dependence of CPP resistance (R_{zz}).

3.2 Anisotropic Magnetoresistance (AMR) of Ni Foil

Anisotropic magnetoresistance (AMR) of the bottom Ni contact has no effect on the observed MR data presented in Figure 3.2 due to the following reasons: (a) the typical AMR effect is ~1% (Figure 3.8), whereas we have observed ~10^4% MR in

Figure 3.2, (b) the CPP resistance of the Ni substrate is ~100 times smaller than the CPP resistance of MLG/Ni composite and hence any MR of Ni substrate will be negligible in the MR of MLG/Ni composite and (c) CPP resistance of the composite exhibits a semiconducting temperature-dependence (Figure 3.3) and not a metallic temperature-dependence as shown in Figure 3.8. Thus we can rule out possibility of any artifact due to AMR of Ni. Based on above considerations we can also rule out the possibility of any pinhole short between top Ag contact and bottom Ni substrate.

3.3 Ag/MLG Contact Resistance

To understand the role of Ag/MLG contact resistance, we have evaluated the (zero magnetic field) contact resistance between Ag paste and MLG using two different methods as described below. Devices for in-plane measurements have been fabricated in two different ways. In one method, MLG has been transferred on Au fingers patterned on SiO_2 substrate. Au wires have been attached to these fingers by using Ag paste. Transfer process of the MLG has been described previously in Chapter 2, section 2.1.3 of this thesis. In the second method electrical contacts are directly made on the top surface of transferred MLG by Ag paste. Thus in these devices the MLG is actually contacted by Au fingers and not directly by Ag paste. A digital image of the in-plane device and measurement geometry are shown in Figure 3.9 (a). Distance between neighbouring electrical contacts is ~ 1mm. Contact area is ~ $1mm^2$ (same as in our CPP devices in Figure 3.2 and 3.3). Similar in-plane device dimensions have been reported in some recent work such as ref.s [122]–[124]. In-plane resistance has been measured by both two-probe and four-probe methods. Devices contacted by Au fingers or Ag paste show nominally identical (in-plane) MR behaviour. Since devices in which Ag paste contacts have been made directly on graphene are directly relevant for our study (since they allow estimation of Ag paste/graphene contact resistance), we present data from these devices in Figure 3.9 (b).

Figure 3.9 (b) shows in-plane MR (measured in a four probe geometry, Ag-paste contacts directly made on MLG) of the transferred MLG sample. In-plane

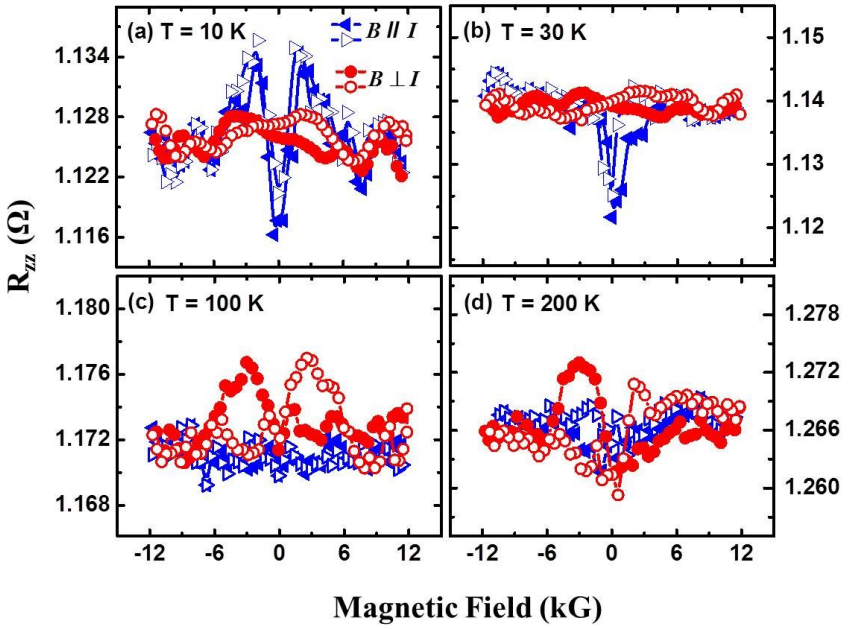

Figure 3.8 AMR of Ni Foil Substrate. (a)-(d) Typical AMR response of Ni foil for the temperature range 10–200 *K*. Triangular symbols indicate scans in $B \| I$ geometry and circular symbols indicate scans in $B \perp I$ geometry.

resistance exhibits insulating temperature dependence, which is consistent with ref.[118]. MR data has been taken in presence of an out-of-plane magnetic field. No strong negative MR signal has been observed. We only observe weak positive MR (~ 8% at 120K and ~ 7% at 300K). Thus the MR response reported in Figure 3.2 must originate from out-of-plane carrier transport.

We have evaluated the (zero magnetic field) contact resistance between Ag paste and MLG using two different methods. First, the two-point and four-point resistances have been measured (Figure 3.9 (c)) between the inner pair of contacts (B and C) in Figure 3.9 (a). Contact resistance has been estimated as [two-point-resistance – four-point-resistance]/2. Two-point and four-point data have been collected by Picotest M3500 multimeter as well as Keithley 2636 Dual Channel Source Meter. Excellent agreement has been obtained between the readings of these two equipment.

Next, we have plotted two-point resistance (zero magnetic field) as a function of the distance between contacts (or "channel length") in Figure 3.9 (d). Two-point

resistance has been found to increase linearly with increasing channel length. This linear trend, extrapolated to zero channel length limit, should give us an estimate of the contact resistance since contact resistance is independent of the channel length. In Figure 3.9 (d) solid lines and filled symbols correspond to zero magnetic field measurements. Same current bias (1mA) has been used in all measurements (in-plane two-point and four-point in Figure 3.9, out-of-plane in Figure 3.2 and 3.3).

Contact resistances estimated by these two methods match very closely and in all cases contact resistance is ~ 1 – 3 Ohms. This value is two orders of magnitude smaller than the (zero field) CPP resistance reported in Figure 3.2. Further, the contact resistance does not depend significantly on magnetic field. In Figure 3.9 (d) we also show the two-point-resistance vs. channel length data taken at 11kG (open symbols, dashed lines). As expected, in presence of magnetic field, resistance values are slightly higher compared to the corresponding zero magnetic field values (positive in-plane MR effect, Figure 3.9 (b)). However they depend linearly on channel length and the extrapolated values in the limit of zero channel length match very well with the zero field case. Thus, Ag paste/graphene contact resistance does not play any crucial role in our reported CPP MR data. The evidences described in sections 3.1.3, 3.2, 3.3 indicate that the transport features in Figure 3.2, 3.3 and 3.4 are not limited by the "defective region" in the vicinity of Ni/MLG interface, but is governed by the "defect-free region" located away from the Ni/MLG interface. Based on the data described in sections 3.1.2 and 3.1.3, we conclude that the large negative CPP-MR originates from the graphene layers that are characterized by distortion free 2*D* band and in the absence of *D* band.

3.4 CPP-MR of CVD-Grown MLG on Cu

We have studied CPP-MR of MLG samples as grown on Cu (ACS materials). Figure 3.10 (a) shows the typical MR response of such MLG-on-Cu samples. A negative MR of ~ 0.8 % is observed between ± 0.6 T in the temperature range 10 K– 50 K. This negative MR gradually decreases with temperature and completely

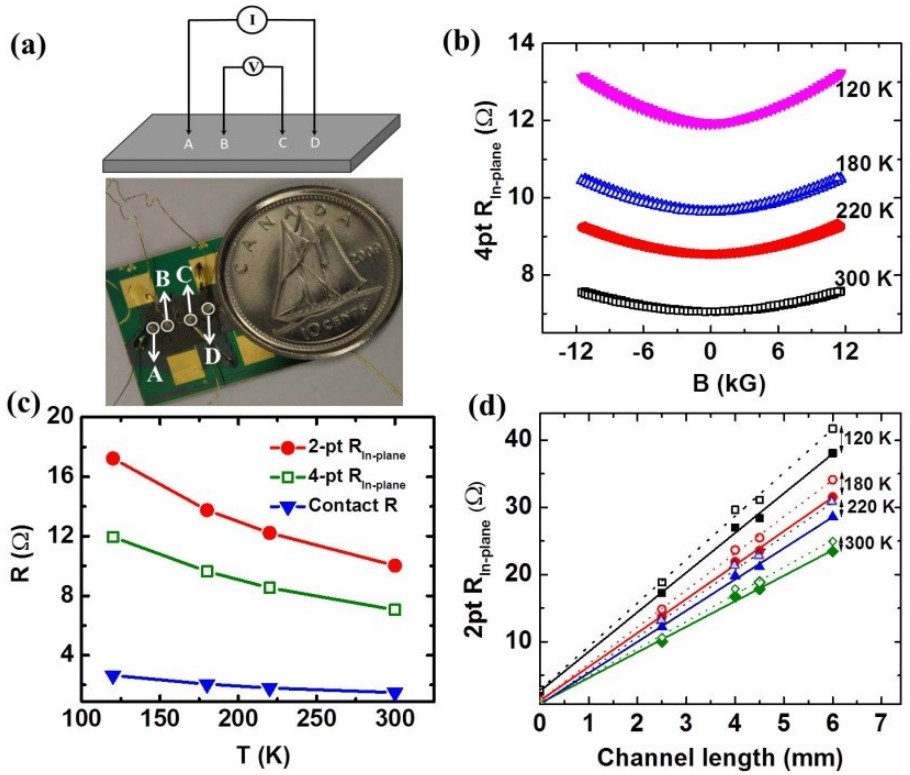

Figure 3.9 In-plane Measurements. (a) Four point measurement geometry and digital image of the device. (b) In-plane four-point MR of transferred (Ni-grown) MLG. (c) Two-point and four-point in-plane resistance at zero magnetic field. Contact resistance has been estimated as half of the difference between two-point and four-point data. (d) In-plane two-point resistance vs. channel length (i.e. distance between the two contacts). Closed symbols and solid line fits correspond to zero magnetic field case whereas open symbols and dashed line fits correspond to the case when 11kG out-of-plane magnetic field is present. The linear trends extrapolated to zero channel length limit provide an estimate of the Ag paste/MLG contact resistance.

disappears above 120K. The similar CPP-MR response has been reported before in MLGs prepared by a layer-by-layer transfer technique on a Cu substrate [8], and such MR has been attributed to weak localization (WL) effect [8], [10]. Linear current-voltage ($I - V$) characteristics indicate bias independence of observed MR (Figure 3.10 (b)).

3.5 Discussion

To our knowledge, CPP-MR of as-grown MLG on Ni has not been studied previously and the large negative CPP-MR observed in Figure 3.2 has not been

reported before in any graphene-based system [8], [9], [11]. However, growth on Ni substrate alone is not sufficient for observation of the large negative CPP-MR effect. As described in section 3.1.3, this effect is absent in thin MLG that exhibits Raman *D* peak. As shown above, the negative CPP-MR originates from the "defect-free region" away from the Ni/MLG interface. Further, this negative MR has been found to be correlated with the Raman *2D* lineshape of the "defect-free region". As mentioned before, the devices characterized in Figures 3.2 and 3.3 do not exhibit any significant splitting or HOPG-like shoulder peak in the *2D* Raman band and large negative CPP-MR has been observed only in these samples. If the 2*D* Raman band shows HOPG-like shoulder peak or splitting, then the large negative CPP-MR is absent and a positive CPP-MR is observed instead (section 3.1.2). Negative MR in the vicinity of zero magnetic field can originate from three sources: (a) weak localization [8], (b) spin filtering and associated giant magnetoresistance (GMR) effect [33] and (c) interlayer tunneling between zero mode Landau levels [38], [39], [61], [62]. Negative MR originating from weak localization gradually diminishes with increasing temperature due to reduction of phase coherence time at higher temperatures [8]. In our MLG/Ni samples (Figure 3.2) however, the negative MR is relatively insensitive to temperature. Additionally, the shape and angle dependence of MR in Figure 3.2 are qualitatively different than that observed in the case of weak localization and for thick samples such as ours this effect is not expected to occur [8]. Finally, the negative MR effects shown in Figure 3.2 are orders of magnitude stronger than a typical weak localization related effect in similar system [8]. Therefore, it is unlikely that the MR response shown in Figure 3.2 originates from weak localization.

Very recently a novel "perfect spin filtering" effect has been proposed in MLG CVD-grown on (111) Ni [33] . Due to very high degree of spin filtering (~ 100%), such effect can give rise to very large negative MR. According to this theory, perfect spin filtering is achieved due to special energy band alignment at (111) nickel/graphene interface, which promotes transmission of only minority spins through the graphene [33].

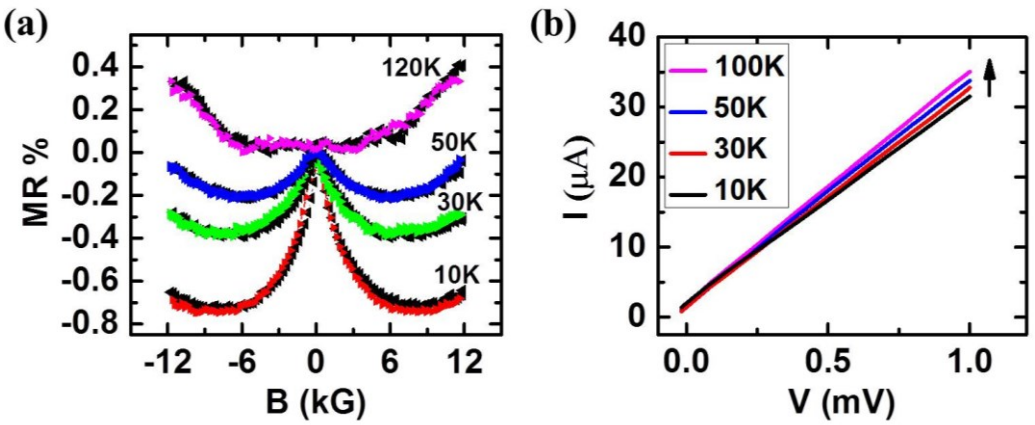

Figure 3.10 Charge Transport Characteristics of MLG/copper Sample. (a) CPP-MR of MLG/copper showing weak localization at low field in the temperature range 10 K– 50 K, which disappears at higher temperature. (b) Linear current-voltage (*I-V*) characteristics indicate bias independence of observed negative MR.

Presence of multiple graphene layers (3 – 4 or more) quenches any tunneling conductance of majority spins. However, in our case such spin-dependent transport cannot be used to explain the observed MR. This is because our device (Ni/MLG/Ag) is not a "spin valve" type device since the top electrode (Ag) is *non-magnetic*. Thus, unlike ferromagnetic contacts, this electrode is not able to differentiate between various spin orientations. Thus, we believe that the observed large MR in Figure 3.2 is not due to this spin filtering effect.

Negative MR can also arise from an interlayer tunneling mechanism, which is often dubbed "interlayer magnetoresistance" or ILMR [38], [39], [61], [62]. As described before in Chapter 1, section 1.4.4, this effect is observed in a stack of two-dimensional (2D) massless Dirac electron systems. The interlayer coupling between these 2D layers should be sufficiently weak so that the entire system can be viewed as a stack of 2D systems instead of a bulk 3D material. In such systems out-of-plane charge transport occurs via interlayer tunneling. Such interlayer current can be tuned by a large factor by applying an out-of-plane magnetic field. The physical origin of this ILMR effect is described below.

For a stack of weakly coupled 2D massless Dirac electron system in absence of any magnetic field, electronic dispersion of each layer can be modelled by a linear *E-k*

spectrum (or "Dirac cone dispersion") with Fermi level located at the Dirac point [44]. Density of states (DOS) is small at the vicinity of the Dirac point, since it depends linearly on energy measured from the Dirac point [44]. When an out-of-plane electrical bias is applied, carriers tunnel from one layer to the next. In this case small tunneling current is expected due to low DOS near the (quasi) Fermi level of each layer.

When an out-of-plane magnetic field is applied, linear *E-k* dispersion of each layer converts into a series of Landau levels, with a (zero mode) Landau level located at the Dirac point [44]. Out-of-plane charge transport will now occur via interlayer tunneling between the zero mode Landau levels. The degeneracy of the Landau levels increases with magnetic field. Thus with increasing magnetic field, degeneracy of the zero mode Landau level will increase, giving rise to larger interlayer tunneling current. This is the origin of large negative MR and is dubbed ILMR [38], [39], [61], [62].

If the magnetic field is in-plane, it exerts Lorentz force on the electrons traveling out-of-plane and bends their trajectories. As a result, with increasing in-plane magnetic field effective interlayer tunneling distance increases, resulting in weaker tunneling probability and hence smaller interlayer tunneling current. Thus a weak positive MR is observed when the magnetic field is in-plane.

The stack of two-dimensional massless Dirac electron systems can be realized by stacking multiple graphene layers provided the interlayer coupling is sufficiently weak. Further, in order to observe the above-mentioned effect one has to ensure that out-of-plane charge transport occurs primarily via interlayer tunneling and not via some conductive defect states electrically shorting neighbouring graphene layers. As described below, in our devices (Figures 3.2, 3.3) both of these conditions are fulfilled by the graphene layers in the "defect-free region" (i.e. layers away from the Ni/MLG interface).

We note that the lack of pronounced splitting (or lack of HOPG-like "shoulder peak") in the 2*D* band of the Raman spectrum (Figure 2.7) indicates weak interlayer

coupling in the "defect-free region" of these samples. As discussed in Chapter 1, section 1.6, the 2*D* band in the Raman spectrum of (monolayer) graphene originates due to a 2nd order, two-phonon, "double resonance" process, which has been analyzed extensively by various theoretical and experimental techniques [34], [73], [81]–[83]. For monolayer graphene this double resonance process leads to a single Lorentzian *2D* peak in the Raman spectrum. Now, For bilayer/trilayer graphene or graphite the single electronic dispersion curve of monolayer graphene is split into multiple branches due to interlayer coupling [44]. As a result double-resonance scattering processes can take place between various branches, resulting in multiple slightly-shifted Lorentzian peaks. The resultant *2D* band is a combination of all these Lorentzians and therefore loses its symmetrical shape and shows signs of splitting and distortion.

However, if interlayer coupling is weak, splitting of electronic dispersion is negligible and therefore splitting of Raman 2*D* band is also negligible. We note that weak interlayer coupling and absence of splitting in the 2*D* Raman band are common features of CVD-grown MLGs and have been reported by many groups in the past [28], [34]–[36]. Ref.[37] employed Landau level spectroscopy to demonstrate weak interlayer coupling in graphene layers CVD-grown on Ni. The correlation between CPP-MR and 2*D* lineshape as described before indicates that the observed large negative CPP-MR effect originates from the weakly coupled graphene layers.

The weak interlayer coupling and resulting (quasi) two-dimensional picture described above is valid when the nearest-neighbor interlayer coupling (or interlayer transfer energy t_c) is sufficiently small compared to thermal ($k_B T$) and disorder-induced (Γ) broadening. Since we have observed giant negative magnetoresistance even at the lowest temperature of 10 K for which $\Gamma \sim 30\ K$ [125], clearly $t_c < 30$ K ≈ 2.6 meV. This matches reasonably well with ref. [126], which calculated $t_c \sim 5\ meV$ for quasi two-dimensional carriers in graphite. For HOPG samples, on the other hand, $tc \sim 0.39\ eV$ [11] $\gg k_B T$, Γ and the above quasi two-dimensional picture does not hold for T ≤ 300 K. The Raman 2*D* band of

HOPG is also asymmetric with a pronounced shoulder peak (Figure 2.6, Figure 2.8). Thus no ILMR effect is expected in HOPG, which is consistent with our control experiments on HOPG-like sample (Figure 3.6) and previous work [9].

As mentioned before, presence of defects is negligible in the "defect-free region" of thick MLG samples grown on Ni foil (both homemade and purchased). For MLG-on-Ni, both fcc and hcp domains can form during CVD growth, depending on the adsorption sites of the carbon atoms [108]. According to ref.[108], the grain boundaries between these domains are often "delaminated" from the substrate and MLG tends to bulge away from the substrate. These features allow matching of fcc and hcp domains by a continuous sheet of graphene, without formation of defects at the domain boundaries. In our MLG-on-Ni samples, we have observed similar bulging features as shown in Figure 2.3. This is presumably the reason for absence of D peak in the "defect-free region" of our MLG-on-Ni samples. Thus weak interlayer coupling is preserved in the "defect-free region" of MLG-on-Ni samples described in Figures 3.2 and 3.3 and in this region CPP charge transport primarily occurs via interlayer tunneling and not via conductive defect states.

The thin MLG samples (~ 15 – 20 nm) as-grown on Ni also show symmetric 2*D* Raman peak (Figure 2.9). However, unlike thicker specimens, these are accompanied by defect (*D*) peak and CPP transport is fundamentally different from the thicker samples (Figure 3.7). In these thinner samples, CPP charge transfer primarily occurs via defect states instead of any interlayer tunneling. As a result, no large negative CPP-MR is observed in these thinner samples.

We have studied CPP-MR of MLG samples as-grown on Cu. Such devices have been studied by other groups in the past [8] but no large negative CPP-MR (similar to Figure 3.2) was reported. Samples grown on copper typically show symmetric Raman 2*D* peak (Figure 2.11) and therefore large negative CPP-MR is expected in these samples as well. However, the copper-grown MLG samples also exhibit significant defect peak (~1360 cm^{-1}, Figure 2.11, bottom scan) in the Raman spectrum, which originates from the grain boundaries and also as a result of the

fabrication process [8], [56]. As mentioned in Chapter 2, the edge states at the grain boundaries are known to be conductive [107] and can effectively short the neighboring graphene layers. In this case, CPP charge transport will primarily occur via the conductive edge states instead of interlayer tunneling. This is presumably the reason for absence of large negative CPP-MR in Cu-grown samples. Transport through edge states and defects however results in a weak negative CPP-MR at low temperature due to weak localization and this effect has been observed by us (Figure 3.10 (a)) and is consistent with literature [8].

Summarizing the above discussion, we conclude that for the samples in Figures 3.2, 3.3 the graphene layers in the "defect-free region" (i.e. away from the Ni/MLG interface) are characterized by distortion-less 2*D* band and absence of *D* band in the Raman spectrum. Thus, in this region interlayer coupling is weak, and charge transfer via conductive edge states (defects) is absent. Due to weak interlayer coupling, CPP resistance is dominated by these weakly coupled layers and a large zero-field CPP resistivity is observed compared to typical HOPG samples [9]. CPP charge transfer in these layers takes place only by interlayer tunneling and results in a large negative ILMR in presence of an out-of-plane magnetic field. Thus, the primary role of the Ni substrate is to realize graphene layers that are weakly coupled and are not electrically shorted with each other via conductive edge states. Our CVD growth parameters (Chapter 2, section 2.1.1) allow us to simultaneously satisfy both of these conditions.

Varying the growth parameters can give rise to strong interlayer coupling characterized by split or HOPG-like 2*D* band in the Raman spectrum (Figure 2.8). Similarly in case of commercially available HOPG, interlayer coupling is strong as well (Figure 2.6). Growth on Cu leads to formation of defect states at grain boundaries (Figure 2.11), which effectively short neighboring graphene layers. In all of these cases no ILMR has been observed (Figure 3.10). We have also transferred the Ni-grown MLG on Au and Ni electrodes (patterned on a SiO_2/Si substrate) and have performed CPP-MR measurements (Figure 3.5). As mentioned before, unlike as-grown MLG these transferred samples exhibit a shoulder in the

2*D* Raman band that arises as a result of the transfer process (Figure 2.10). Thus interlayer coupling is adversely affected as a result of transfer and we have not observed any large negative CPP-MR, but found weak positive CPP-MR instead (Figure 3.5), which is consistent with prior studies [8], [9], [11].

According to the interlayer tunneling theory [38], interlayer conductivity σ_{zz} (which is proportional to the inverse of measured interlayer resistance R_{zz}) is proportional to the out-of-plane magnetic field $|B|$ and is given by:

$$\sigma_{zz} = 2C\tau|B|\frac{t_c^2 ce^3}{\pi\hbar^3}$$

where τ is the characteristic lifetime associated with Landau level broadening (or relaxation time for in-plane scattering), t_c is the interlayer transfer energy estimated to be ~ 2 meV for weakly coupled graphene layers (as discussed earlier), c represents interlayer spacing (~ 0.342 *nm* for turbostratic graphite with weakly coupled graphene layers), e is the electronic charge and $\hbar$ is reduced Planck constant. It has been shown [38] that C is $\sim 1/k_BT$ for "high temperatures" for which $k_BT > t_c, \hbar/\tau$. This condition is satisfied at almost all temperatures (above ~ 30K) considered in this work and hence C can be equated to $1/k_BT$. Now since τ is expected to decrease with increasing temperature, we expect the slope of $\sigma_{zz} - |B|$ curve to decrease with increasing temperature.

To check the validity of this model, first we have fitted $1/R_{zz}$ as a function of B as shown in Figure 3.11. A clear linear fit is observed in the vicinity of ~ 2 kG, where the negative MR occurs. Further as mentioned above, the slope of $1/R_{zz}$ vs. B is expected to decrease with increasing temperature, which is also consistent with Figure 3.11.

However we note that this model is not valid in the low field regime (~ 0 kG) where inter Landau level mixing plays a dominant role [39], [61]. This model also does not hold at high magnetic fields (> ~ 3kG) where additional level splitting (due to effects such as spin-orbit interactions) may become important. We note that a strong Rashba type splitting has been reported in graphene/Ni composites [32], which can become further pronounced in presence of high magnetic field. Such additional

level splitting will clearly affect the high field CPP-MR. Such effects are not captured by the interlayer tunneling model described above. Additionally, strain in graphene layers can result in strong out-of-plane pseudo-magnetic field (~ 300 T), which mimics the externally applied field and gives rise to pseudo Landau levels [127]. Stacking misorientations in graphene layers can result in strong in-plane pseudo-magnetic field [128]. These effects may play a role in quantitative understanding of the observed MR effect. The observed angle dependence of the CPP-MR response (Figure 3.2) is also consistent with the interlayer tunneling theory. As described before, in $B \perp I$ configuration, classical Lorentz force bends carrier trajectory to the direction parallel to the MLG plane, which reduces interlayer tunneling probability and results in a positive MR. Such bending becomes less pronounced at higher temperatures due to thermal fluctuations. As a result, the positive CPP-MR effect weakens with increasing temperature as observed in Figure 3.2.

In Figure 3.2, the shape of the low-field MR response (+/- 2 kG range) is strongly dependent on temperature. At low temperatures (10 – 80K) the low-field MR response is "smooth-topped" with gradual variation in the neighborhood of zero field, but at higher temperature (160K, 250K) the low-field MR response becomes "flat topped". This indicates that at higher temperature a competing positive (low-field) MR effect emerges that offsets the negative (low-field) MR and makes the net (low-field) MR flat-topped. At 300K, the positive MR effect is quite dominant and we see a weak net positive MR effect in the near vicinity of the zero field. As described below, the "interlayer tunneling" model mentioned above can be used to obtain a qualitative understanding of the temperature-dependence of low-field MR curves.

According to the interlayer tunneling model, the low-field MR response results from a competition between the following two mechanisms: (a) interlayer tunneling between the zero-mode Landau levels, which gives rise to negative MR and this effect becomes dominant as the magnetic field is increased due to an increase in

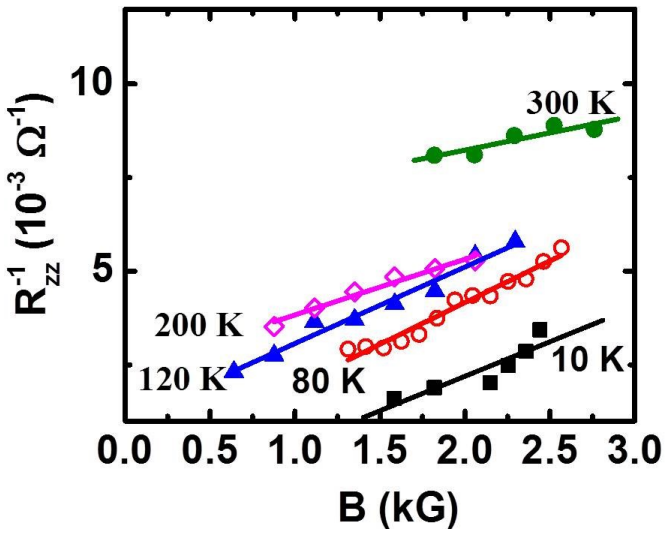

Figure 3.11 Inverse of CPP resistance (R_{zz}) as a function of out-of-plane magnetic field (B) in the vicinity of the switching field of ~ 2 kG. A linear trend is observed at all temperatures.

Landau level degeneracy and (b) a positive MR effect, which originates from inter-Landau level mixing due to thermal broadening [61]. The positive MR effect is only effective at low field range and higher temperature, where inter-Landau level spacing is comparable to thermal broadening. In presence of inter-Landau level mixing, interlayer carrier transfer is not perpendicular to the plane, which results in a positive MR. We observed such effects for temperatures 160K and 250K (Figure 3.2 d, e), at which the positive MR effect offsets the negative MR effect in the vicinity of zero field and results in a flat-topped MR response near zero field. At 300K (Figure 3.2 f) the positive MR exceeds the negative MR and hence we observe a small net positive MR near zero field. At 10K, 30K and 80K (Figure 3.2 a, b, c) thermal broadening is negligible, which suppresses the positive MR effect and only negative MR is observed at low field.

Figure 3.12 shows the temperature dependence of the "switching field (B_{sw})" at which sharp drop in CPP resistance takes place due to the negative MR effect. In this plot B_{sw} is taken to be the field value at which resistance decreases to 50% of its zero-field value and B_{sw} essentially demarcates the low field region from the high field region. We note that the switching field as defined above is not necessarily same as the "critical magnetic field" required to achieve "quantum

limit" [38]. As described before, the low field MR is a result of two competing processes and the negative MR effect should be dominant when the inter Landau level mixing is not significant (but not necessarily zero). In order to reduce inter Landau level mixing, spacing between neighboring Landau levels should be made comparable (or larger) than thermal broadening of the Landau levels. Inter Landau level spacing increases with magnetic field [44] and thermal broadening increases with temperature. Thus at higher temperatures, negative MR will manifest at higher magnetic field. Thus, B_{SW} is expected to show an increasing trend with temperature. This is consistent with Figure 3.12.

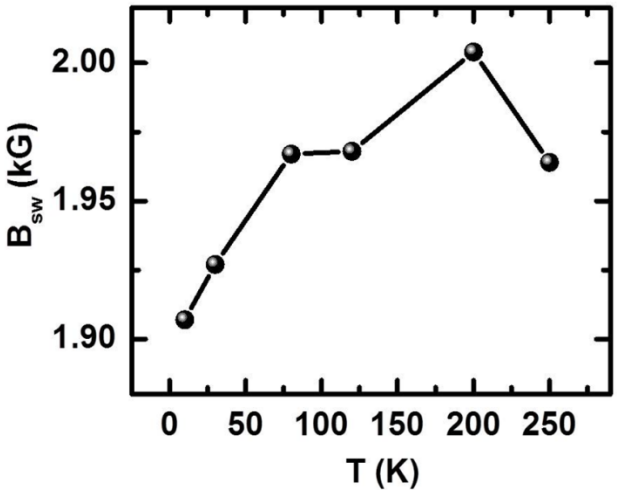

Figure 3.12 Switching magnetic field as a function of temperature.

3.6 Conclusion

In conclusion, we have observed a novel giant negative CPP-MR ($> 10^4\%$) in MLG as-grown on Ni, which persists even at room temperature. The negative MR manifests in thick multilayer samples in which the Raman 2*D* peak does not exhibit any significant splitting (or HOPG-like distortion) and the *D* peak is absent. Such features have been realized by controlling the parameters of the CVD growth process. The observed data is qualitatively consistent with the "interlayer magnetoresistance" (ILMR) mechanism in which interlayer charge transfer occurs between the zero mode Landau levels of weakly coupled graphene layers. Due to large MR value and its persistence at room temperature, this effect is expected to

have commercial implications and encourage further research on MLG physics and MLG growth mechanisms on ferromagnetic substrates.

A detailed angle dependent study will be presented in the next chapter.

4 ANGLE DEPENDENT INTERLAYER MAGNETORESISTANCE (ILMR) IN CVD-GROWN MLG[6]

In the last chapter, we have reported current perpendicular to plane (CPP) magnetoresistance (MR) in CVD grown multilayer graphene (MLG) on Ni. As-grown graphene layers are misoriented, which has been confirmed by Raman spectroscopy (section 2.2.1, Chapter 2) and this observation is consistent with prior studies as well [28], [37]. A very large negative CPP MR effect was observed in as-grown MLG which persists even up to room temperature (Figure 3.2, Chapter 3). By means of control experiments (sections 3.1, 3.2 and 3.3, Chapter 3) it was shown that the observed negative CPP MR originates from the MLG stacks and not from the Ni/graphene interface or the contacts. However, only two orientations of the external magnetic field were considered: $B \parallel I$ ($\theta = 0^o$) and $B \perp I$ ($\theta = 90^o$). The observed CPP MR effect was found to be consistent with the interlayer magnetoresistance (ILMR) theory developed in ref.s [38], [39]. However, ILMR has a unique dependence on the tilt angle θ, which provides additional insight into CPP magnetotransport of this unusual material system. In this chapter, we are providing a detailed angle dependent study of ILMR effect in CVD grown MLG.

A brief description of ILMR has been provided in previous chapters (sections 1.4.4 and 3.5). For the convenience of the reader, in this section, we review key features of ILMR and prior works related to angle dependent study of ILMR. ILMR effect can be observed in out of plane charge transport of multilayer massless Dirac carrier systems. These materials are realized by stacking two-dimensional (2D) layers of Dirac carriers, while ensuring weak coupling between the neighbouring layers. Charge carriers obey linear energy dispersion in each layer and due to weak interlayer coupling, their motion is primarily confined in the 2D plane. Thus these materials can also be viewed as "bulk 2D systems" with zero gap energy bands [39]. Current perpendicular to plane (CPP) transport in these systems takes place

[6] Results described in this chapter have been published in [98].

via interlayer tunnelling between the weakly coupled layers and CPP transport exhibits novel magnetoresistance (MR) effects such as ILMR that are not observed in other material systems.

The origin of this CPP MR is intricately related to the existence of 2D Dirac carriers in individual layers. In presence of an out-of-plane magnetic field B_z, linear energy dispersion of each layer transforms into a series of Landau levels [40], [44], [129]. Of particular importance is the so-called "zero mode Landau level", which is a unique feature of 2D Dirac electrons [40], [44], [129]. This zero mode Landau level remains pinned at the Dirac point, which also coincides with the Fermi level where carrier occupancy probability is ½ [40], [44], [129]. Thus, interlayer tunnelling now occurs between the zero mode Landau levels of the individual layers. As the magnetic field B_z is increased, degeneracy of the zero mode Landau level and hence carrier density at zero mode increases, resulting in an increased tunnelling current and negative CPP MR. As shown in ref.[38], CPP resistance (R_{zz}) in this system has $1/|B_z|$ dependence and hence strong negative MR can be obtained for relatively small values of magnetic field. This effect is often dubbed "interlayer magnetoresistance" or, ILMR [38], [39], [62]. It is important to note that in this configuration, magnetic field (B_z) is parallel to the interlayer current and hence no classical magnetoresistance effect is expected due to absence of Lorentz force.

However, realization of such multilayer massless Dirac electron systems is not straightforward. The material that has been extensively studied so far in this context is the organic compound α-(BEDT-TTF)$_2$I$_3$ where BEDT-TTF represents bis(ethylenedithio)-tetrathiafulvalene [39], [62]. This material has a multilayered structure in which conductive layers of (BEDT-TTF) molecules are separated by insulating layers of I_3^-. As a result, the conductive layers are weakly coupled to each other resulting in strong conductance anisotropy and strong 2D nature of the charge carriers. When subjected to high pressure (> 1.5 GPa) [39], carriers in the conducting layers follow Dirac-like energy dispersion. The ILMR effect described above has been reported in this system at low temperatures, ~ 10K [39], [62].

Graphene, a single atomic layer of carbon atoms arranged in a honeycomb pattern [40], [130], is a well-known 2D massless Dirac Fermion system. Existence of 2D Dirac carriers in graphene has been established experimentally via observation of unconventional half-integer quantum Hall effect [15], [131]. In principle, multilayer massless Dirac carrier systems could be realized by stacking multiple graphene layers. In fact such a stacked configuration exists in nature and is commonly known as graphite. Unfortunately, the neighbouring graphene layers in graphite are generally strongly coupled, which results in 3D nature of the charge carriers instead of massless 2D behaviour. This is particularly true for most common phases of graphite such as Bernal (or AB) stacked and rhombohedral (or ABC) stacked graphite [34], [83], which exhibit complex energy dispersion near the Fermi level instead of linear, massless dispersion of single layer graphene. As a result ILMR effect as described in ref.s [38], [39], [62] is rarely observed in graphitic systems [9], [11].

However, interlayer coupling between neighbouring graphene layers in graphite can be significantly weakened if the neighbouring layers are misoriented with respect to each other so that AB or ABC stacking is destroyed. Such randomly oriented stack of graphene layers is often termed as “turbostratic graphite” and can be realized by chemical vapor deposition (CVD) technique as shown in sections 2.1.1, 2.2.1 (Chapter 2) [12], [28], [35], [37], [96]. Due to weak interlayer coupling in this system, charge carriers have 2D Dirac character, despite the presence of the neighbouring layers. Existence of 2D Dirac carriers in CVD grown multilayer graphene (MLG) has been demonstrated by various techniques such as Raman spectroscopy [28], [34], scanning tunnelling microscopy [37], infrared spectroscopy[132] and even ab-initio calculations [133]. Thus ILMR effect is expected to manifest in CVD grown multilayer graphene stacks (or, turbostratic graphite). In the next section, we will discuss theory related to angle dependent ILMR in bulk 2D systems such as CVD grown MLG stacks.

4.1 Angle Dependent Interlayer Magnetoresistance (ILMR)

The basic idea of ILMR has been briefly outlined above and is schematically described in Figure 4.1. In this section, we review key concepts to understand angle dependent ILMR effect in bulk 2D systems. As mentioned before, most of this work has been done on α-(BEDT-TTF)$_2$ I$_3$. As described before, a vertical stack of weakly coupled 2D Dirac electron systems is considered, in which Fermi level resides in the vicinity of the Dirac points where the density of states is small (in absence of any external magnetic field, Figure 4.1(a). Any interlayer charge transfer occurs via tunnelling between the states located close to the Fermi level. In this case, interlayer current is small, due to lack of available states (and low number of carriers) in the vicinity of the Fermi level. In this case, therefore large CPP resistance (R_{zz}) is expected.

This situation changes dramatically when an out-of-plane magnetic field (B_z) is applied. The linear energy dispersion of 2D Dirac electrons now converts into a series of Landau levels (Figure 4.1(b)), given by $E_n^{LL} = \pm\sqrt{(ehv_F^2|n||B_z|/\pi)}$, where v_F is the Fermi velocity and n is an integer representing the Landau index. Most importantly, a "zero mode" Landau level corresponding to $n = 0$ exists at the (quasi) Fermi level (Figure 4.1(b)). This zero mode Landau level is a signature of 2D Dirac materials and as can be seen from the above expression of E_n^{LL}, its location is independent of the applied magnetic field. As the out-of-plane magnetic field is increased, degeneracy (eB_z/h) of the zero mode Landau level and carrier concentration of zero mode increases. Since interlayer current is carried by the charge carriers located in the vicinity of the (quasi) Fermi level (Figure 4.1(b)), increased magnetic field increases the interlayer current, which results in negative interlayer magnetoresistance (ILMR). As noted before (see section 3.1.1, Chapter 3), in this measurement configuration ($\theta = 0$, Figure 4.2a) magnetic field does not exert any Lorentz force on the charge carriers.

When the magnetic field is slightly tilted from the out-of-plane direction ($\theta \neq 0$, Figure 4.2(a)), Lorentz force on the charge carriers is non-zero and carrier trajectory

deflects from the out-of-plane direction. As a result, effective tunnelling distance between neighbouring layers increases, resulting in smaller interlayer current or reduced ILMR. In the limit of in-plane magnetic field, interlayer current is weakest and a positive magnetoresistance is observed (see Figure 3.2, Chapter 3).

This physical picture has been modeled in ref.[38], which derived the following expression for interlayer resistivity (ρ_{zz}) under dc bias and in presence of an external magnetic field B (B_x, B_y, B_z):

$$\rho_{zz}(B) = \frac{\pi\hbar^3}{2C\tau t_c^2 ce^3}\frac{1}{|B_z|}exp\left[\frac{1}{2}\frac{ec^2\left(B_x^2 + B_y^2\right)}{\hbar|B_z|}\right] \qquad (1)$$

where τ is the characteristic life time (or relaxation time for in-plane scattering), c is the interlayer spacing (~ 0.342 nm for turbostratic graphite [34]), e is electronic charge, $\hbar\ (= h/2\pi)$ is reduced Plank constant and t_c is the "interlayer transfer energy", which represents the degree of coupling between neighbouring graphene layers [38]. As discussed before in section 3.5 (Chapter 3), the condition of "weak interlayer coupling" requires t_c to be smaller than disorder induced broadening ($h/2\pi\tau$) and thermal broadening (k_BT) [38]. For graphene, $h/2\pi\tau \sim$ 30K [125] (~ 3 meV) and for weakly coupled graphene layers, $t_c \sim$ 2meV [11], [126]. Thus the condition of "weak interlayer coupling" holds over our measured temperature range of 10K–200K.

According to ref. [38] $C \sim 1/k_BT$ for "high temperatures" i.e. $k_BT >> t_c$, $h/2\pi\tau$. As indicated above, in case of graphene, disorder induced broadening $h/2\pi\tau \sim$ 30K (or, ~ 3meV [125]) and high temperature limit can be attained for temperatures above 30K (Figure 3.2, Chapter 3) [96]. From the above expression it is clear that for purely out of plane magnetic field (B_x, B_y = 0), $\rho_{zz} \sim 1/|B_z|$, which is the origin of large negative ILMR. In the limit of purely in-plane field (B_z = 0), ρ_{zz} approaches infinity because the carriers will be strongly deflected towards the plane, which results in very low interlayer tunnelling probability due to large increase in effective

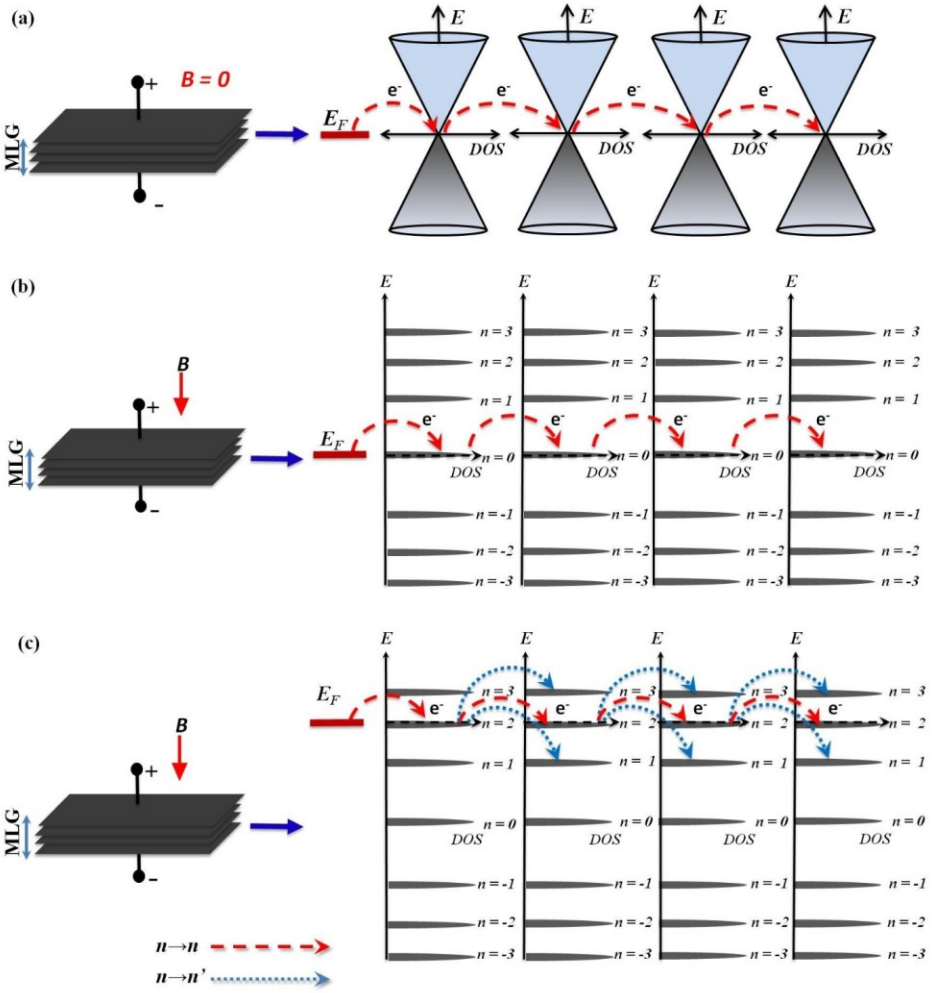

Figure 4.1 Schematic description of the ILMR effect. (a) Applied magnetic field (B) = 0 and an out of plane electrical bias drives the interlayer current. Weak interlayer coupling ensures that Dirac cone dispersion is preserved for individual layers. Carrier transport occurs via tunneling between the states in the vicinity of the (quasi) Fermi level E_F (or Dirac point). Due to the dearth of available states (and hence available carriers) and weak interlayer coupling, interlayer current is weak. (b) Out of plane magnetic field is applied ($B \neq 0$) and a zero mode Landau level ($n = 0$) forms at the Dirac point, which coincides with the quasi Fermi level E_F. Each Landau level has a finite broadening due to disorder and thermal effects. Density of states (DOS) and carrier concentration of zero mode is proportional to B. Since interlayer transport occurs via zero mode, large interlayer current is observed due to large number of carriers participating from each layer. (c) Inter Landau Level mixing effect (dotted lines), which is dominant when inter Landau level separation is small (such as small B, large T etc.). Dashed lines show typical ILMR mechanism, without any mixing. In this case E_F is located away from the Dirac point.

tunnelling distance. Using the above expression of ρ_{zz}, the following angle (θ) dependence can be obtained:

$$\rho_{zz}(\theta) = \frac{\pi\hbar^3}{2C\tau t_c^2 ce^3}\frac{1}{B|cos\theta|}exp\left[\frac{1}{2}\frac{ec^2Bsin^2\theta}{\hbar|cos\theta|}\right] \qquad (2)$$

As can be seen from the above formula, for a given field strength B, ρ_{zz} increases as the deviation (θ) from the plane normal is increased.

The above formulae (equations 1 and 2) for ρ_{zz} assume that interlayer charge transport occurs between the zero mode Landau levels of the individual layers and no other level participates in conduction, which is the so-called "quantum limit"[38]. While this assumption is valid for the intermediate values of magnetic field, other effects come into play at smaller and higher field values. For example, if the magnetic field is weak, separation between n = 0 and n = 1 levels ($\Delta E = \sqrt{(ehv_F^2|B_z|/\pi)} = \sqrt{(ehv_F^2|B\cos\theta|/\pi)}$) will be smaller than Landau level broadening ($\Gamma \sim$ max ($h/2\pi\tau$, k_BT)) and in this case both modes will participate in interlayer transport. It is straightforward to find out the "critical value" of the applied field B (say, B_{cr}) above which "quantum limit" is achieved. For graphene, using $h/2\pi\tau \sim$ 30K [125], we obtain $B_{cr} \sim 68G/\cos\theta$ for T ≤ 30K. For higher temperatures, $\Gamma \sim k_BT$ and in this regime $B_{cr} \sim T^2/\cos\theta$. Clearly, for $B < B_{cr}(T)$, Landau level mixing takes place and it has been shown in ref.[61] that such mixing leads to a positive magnetoresistance effect at low fields *due to non-vertical tunnelling processes*. Thus for $B \sim B_{cr}$, a crossover from positive to negative MR takes place and the expression for $\rho_{zz}(B)$ mentioned above (equation 1) ceases to be valid for $B < B_{cr}(T)$.

At high magnetic field limit, zero mode Landau level will be Zeeman split, resulting in reduced number of available states in the vicinity of the (quasi) Fermi level, which gives rise to a crossover from negative to positive magnetoresistance [38]. For this effect to take place in MLG, Zeeman splitting energy ($g\mu_BB_z \sim 0.12B_z$ meV [40], μ_B being the Bohr magneton and B_z measured in Tesla) must exceed broadening (thermal and disorder induced) of the zero mode Landau level. Even in the low temperature limit, where Landau level broadening is ~ 30K as mentioned

before, observation of the above effect will require a magnetic field of ~ 25T, which is beyond our measurement range. Therefore, the positive magnetoresistance effect due to Zeeman splitting is unlikely to occur in the present study.

It is important to note that the above-mentioned physical picture of ILMR remains valid even when the Fermi level resides within some higher order Landau level ($n > 0$). Effect of higher order Landau levels have been studied in ref.[61] and it has been found that $n \rightarrow n$ interlayer tunnelling leads to negative ILMR even when $n \neq 0$. As discussed before, at small fields, Landau levels overlap and $n \rightarrow n'$ ($n \neq n'$; $n, n' \neq 0$) interlayer tunnelling takes place. This process leads to positive MR at small fields for *non-vertical interlayer tunnelling* [61]. Since inter Landau level spacing decreases with increasing n, the low-field positive MR effect will become more dominant as n increases. Similarly, if the tilt angle θ is increased for a given field strength B, positive MR is expected to become even stronger. This is due to two reasons: first, tilted B results in reduced B_z and reduced Landau level spacing, which leads to significant Landau level overlap and inter Landau level mixing. Second, the tilted B will tend to deflect the carriers towards "in-plane" direction, thus increasing in-plane scattering and resulting in more "non-vertical" interlayer tunneling incidents. In addition, in-plane scattering processes themselves result in positive MR [8] (also see section 4.4.2) and for $\theta \neq 0$ this effect is significant since carriers will experience significant in plane motion during interlayer transport. Such effects are not addressed by the model described by equations (1) and (2) and hence strong deviation is expected for $n \neq 0$ and $\theta \neq 0$. In next section, fabrication and characterization of as-grown MLG sample used for angle dependent ILMR study are presented.

4.2 Device Fabrication and Characterization

Fabrication and characterization steps used for the sample in this study are identical to the steps used previously for sample in Figure 3.2 (Chapter 3). Figure 4.2(a) shows the schematic of the Ni/MLG/Ag device structure and the CPP measurement geometry. Device fabrication steps have been described in detail in section 2.1 (Chapter 2). Briefly, polycrystalline Ni foils with primarily (111) crystal orientation

are used as the catalyst for CVD growth of MLG. The Ni foil also serves as the bottom electrical contact for CPP measurement. As characterized in section 2.2.1 (Chapter 2), as-grown MLG on Ni consists of two distinct regions. The region (~ few layers) close to the graphene/Ni interface is generally defective due to strong overlap between 3*d* states of Ni and $2p_z$ states of carbon [97]. In addition, the interfacial layers contain large number of atomic steps and grain boundaries. The presence of defects has been confirmed by taking Raman spectrum from this region, which shows strong *D* (defective) peak (see later in Figure 4.3(b)). Graphene layers above this region are "defect-free" and these layers are weakly coupled to each other ("turbostratic") as shown in section 2.2.1 (Chapter 2). Again, these features have been confirmed for present sample by Raman studies shown later in Figure 4.3(a). A schematic of the MLG stack on Ni substrate is shown in Figure 4.3(b) *inset*, which highlights the origin of grain boundaries in the interfacial layers and lack of these defects away from the bottom interface. As shown previously (section 2.2.2, Chapter 2), transferring the MLG layer on another substrate generally destroys the weak interlayer coupling. Therefore similar to our previous CPP MR measurements on CVD grown MLG (Figure 3.2, Chapter 3), angle dependent MR measurements in present case are also performed on the as-grown MLG samples (see later in Figures 4.4, 4.5).

To perform CPP-MR measurements on as-grown MLG on Ni, similar to the sample in Figure 3.2 (Chapter 3), we used silver (Ag) epoxy as the top contact, with contact area ~ $1mm^2$ (Figure 4.2(a)). This contact is placed at the centre of the top MLG surface to ensure uniform current distribution. We also transferred the MLG on SiO_2/Si substrate using a previously described (section 2.1.3, Chapter 2) procedure to perform thickness and in-plane MR measurements. Optical images of the transferred MLG and its thickness distribution are presented in Figure 4.2(b), *insets*. Thickness measurements have been performed on the wrinkle-free areas of the transferred MLG and the average thickness is ~ 60 nm.

Figure 4.3(a) shows the Raman spectra from three representative areas of as-grown MLG on Ni used for angle dependent study. Strong *G* peak (1580 cm^{-1}) and absence

of *D* peak (1350 cm^{-1}) have been observed in all cases. This indicates formation of hexagonal lattice of carbon atoms without any significant structural defects. It is to be noted that the penetration depth of Raman laser in graphite is ~50 nm [84] and hence this observation is valid for the graphene layers close to the top surface (the so-called "defect-free layer" in Figure 4.2(a)). The top plot (blue) in Figure 4.3(a) is most commonly observed (> 80% area). However, in all cases the position of the 2*D* band is ~ 2705 cm^{-1} with line-width of ~ 60–80cm^{-1} and the 2*D* band can be fitted with single Lorentzian peak. As described previously in section 2.2.1 (Chapter 2), this is a typical signature of MLG with weak interlayer coupling ("turbostraticity") [7, 15], which is a necessary prerequisite for observation of ILMR.

In section 2.2.1.3 (Chapter 2), we demonstrated that the layers close to MLG/Ni surface are defective and show strong defect peak (*D* peak) in Raman spectra. To gain further insight into this point, we performed Raman studies on MLG surface close to Ni interface. To acquire this spectrum, bottom Ni foil is first etched away and MLG is transferred on SiO_2/Si in such a way that the bottom MLG surface (at the Ni interface) faces up. A clear Raman *D* peak has been observed (Figure 4.3(b)), which confirms the defective nature of this region. The defect peak originates from the edges of small-area graphene sheets that form near Ni/MLG interface and defects created by hybridization between Ni 3*d* and C $2p_z$ orbitals. The graphene layers near this interface have smaller area because their growth starts "horizontally" from the Ni grain boundaries (instead of "vertically" from the Ni surface) and the planar geometrical shape of these graphene layers are determined by the grain boundary distribution of the Ni substrate. Thus, these layers contain numerous truncated graphene planes (Figure 4.3(b) *inset*), which contribute to the *D* peak in the Raman spectrum. However, away from this interface, grain-boundary growth sites are no longer available and graphene layers tend to grow "vertically" on top of the underlying layers. This forms a continuous, undulating coverage over the underlying discontinuous films (Figure 4.3(b) *inset*). As a result, the layers away from Ni/MLG interface are free from the edge states. Also, interfacial hybridization

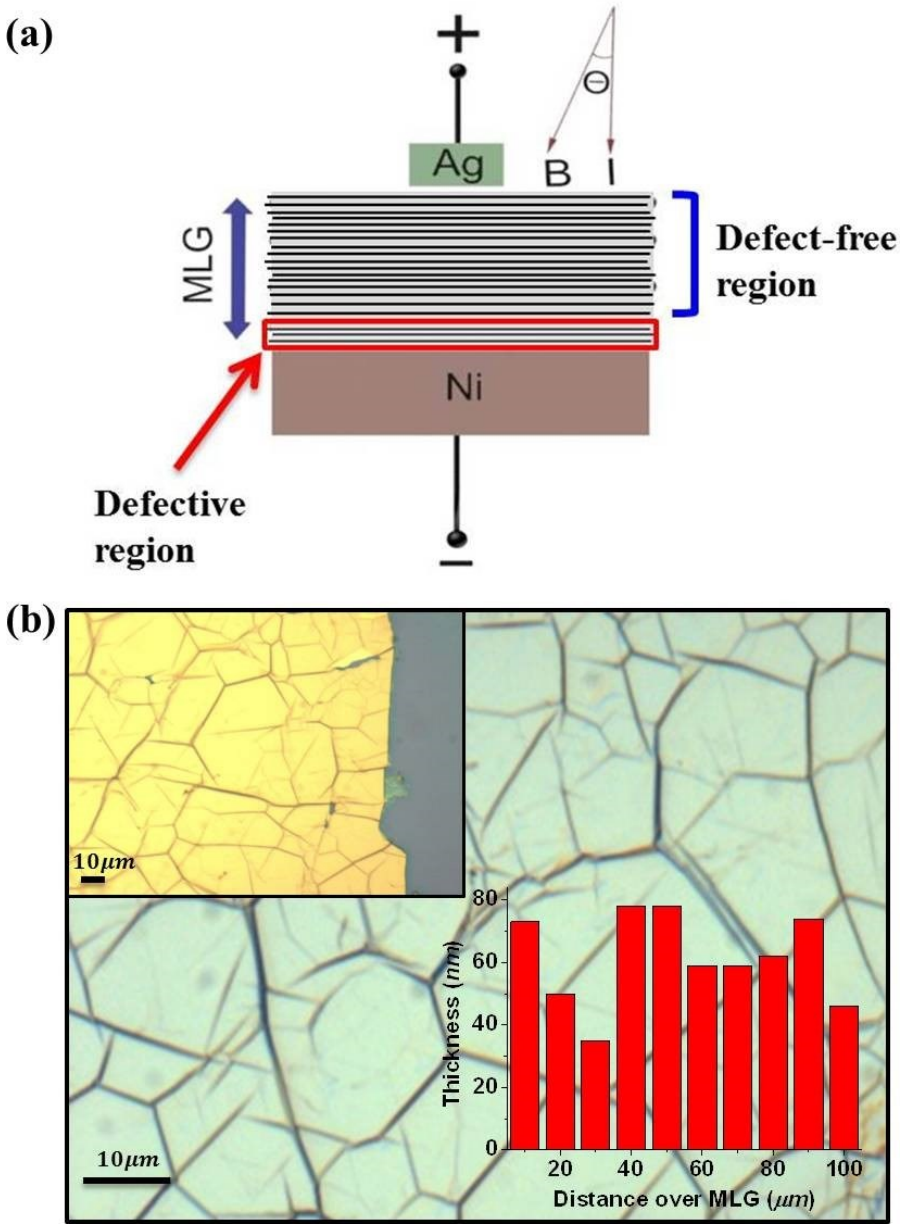

Figure 4.2 Device schematic and optical images of as-grown and transferred MLG. (a) Device structure and measurement geometry. The "tilt angle" θ is measured with respect to the out of plane direction. MLG grown on bottom Ni substrate consists of a "defective" region at the interface and a "defect-free" region at the top. The defect free region consists of weakly coupled graphene layers. Silver paste contact is placed at the centre of the top MLG surface to achieve uniform current distribution. (b) (main image) Optical micrograph of as-grown MLG on Ni. Top left inset shows the transferred MLG on SiO_2/Si. The histogram in the main image shows typical thickness distribution in the wrinkle free areas of transferred MLG. Average MLG thickness in the wrinkle free area is ~ 60 nm. In the optical images, the dark lines represent wrinkles (or regions of larger thickness) in the MLG layer.

effects are absent away from the interface. Due to these reasons, *D* peak is absent in the Raman spectrum taken from the MLG stack away from the interface. The dark contrast in Figure 4.2(b), *main image*, is due to the unevenness in layer thickness near the Ni/MLG interface. After transferring on a flat SiO_2 substrate, this uneven bottom surface creates a wrinkled appearance as shown in Figure 4.2(b), *left inset*. Details of graphene growth on Ni and complete evidence of the physical picture presented above are available in ref.s [134], [135].

Figure 4.3(c) shows the Raman spectra taken from three representative areas of MLG after transferring on SiO_2/Si. Unlike the as-grown samples in Figure 4.3(a), the Raman 2*D* band of the transferred MLG consists of either a shoulder or a strong splitting, which is reminiscent of HOPG (highly oriented pyrolytic graphite) in which the graphene layers are primarily Bernal stacked [34]. The presence of shoulder or significant splitting in Raman 2*D* band is a signature of strong interlayer coupling in MLG [34] and as discussed previously (section 2.2.2, Chapter 2) this change in the 2*D* band behaviour originates due to the transfer process. Thus for ILMR studies, we have chosen as-grown MLG (on Ni) in which the graphene layers are weakly coupled. As shown previously in Figure 3.5 (Chapter 3) and in the present sample (Figure 4.4(c)), transferred MLGs do not show any ILMR effect.

We also note absence of *D* peak in these transferred samples. This proves that the transfer process does not introduce any significant defect in the sample. Thus, the *D* peak observed in Figure 4.3(b) does not originate from the transfer process and indeed comes from the other sources as described above.

To determine the electrical quality of MLG grown in CVD process, we further characterized the transferred MLG using various electrical measurements that are presented later in section 4.4. Based on these measurements, sheet resistance of transferred MLG (~ 60 nm thick) is ~ 50-100Ω, depending on temperature (Figure 4.7, section 4.4.1). This is in good agreement with literature, where similar sheet resistance values were reported for Ni-grown MLG of similar thickness [136], [137]. Typical contact resistance between MLG and Ag paste has been found to be

~ 3-10 Ω (Figure 4.7 (b), section 4.4.1), which is an order of magnitude smaller than the zero field CPP resistance mentioned in the next section. Thus MLG/Ag contact resistance does not play a crucial role in our experiments. Further, in-plane MR measurements performed on transferred MLG (Figure 4.8, section 4.4.2) do not show any weak localization effect even at low temperatures. This is consistent with non-observation of defect peak in the Raman spectrum (Figure 4.3(c)). In contrast, copper grown MLG shows presence of grain boundaries and defects, which are detected in the Raman spectrum (*D* peak) and weak-localization feature in the in-plane MR measurements. Finally, in-plane MR measurements also reveal signatures of Shubnikov-deHaas (SdH) oscillations within 1T (Figure 4.9, section 4.3.3), which indicates formation of Landau levels in this field range. From the periodicity of SdH oscillations, carrier concentration per layer is estimated to be ~ $10^{10}/cm^2$, which implies n ~ 1-2 Landau levels are occupied at B ~ 2kG. As described in the next section, this is roughly the field range where the negative MR manifests in CPP MR measurement of CVD grown MLG on Ni. These electrical measurements confirms that the as-grown MLG used in study consists of high electrical quality and therefore out of plane charge transport in this system is dominated by interlayer tunneling between defect-free graphene layers. Detailed angle dependent CPP MR measurements in CVD-grown MLG on Ni are presented in next section.

4.3 Angle Dependent CPP MR in CVD grown MLG on Ni

In this section, angle dependent CPP MR study is performed in CVD grown MLG on Ni sample that has been characterized in previous section. First, we performed CPP transport measurements in as-grown MLG sample to confirm the existence of ILMR effect (Figure 4.4). CPP resistance has been measured with a bias current of 1mA. Temperature dependence of CPP resistance shows insulating behaviour (Figure 4.4(a)), which is common for out of plane transport in disorder free graphite [116], [117]. The zero field CPP resistance $R_{zz}(0)$ is ~ 190Ω at 15K and ~ 80Ω at 220K (Figure 4.4(a)). Application of a large magnetic field (8kG) results in a decrease in device resistance, but the insulating temperature dependence still

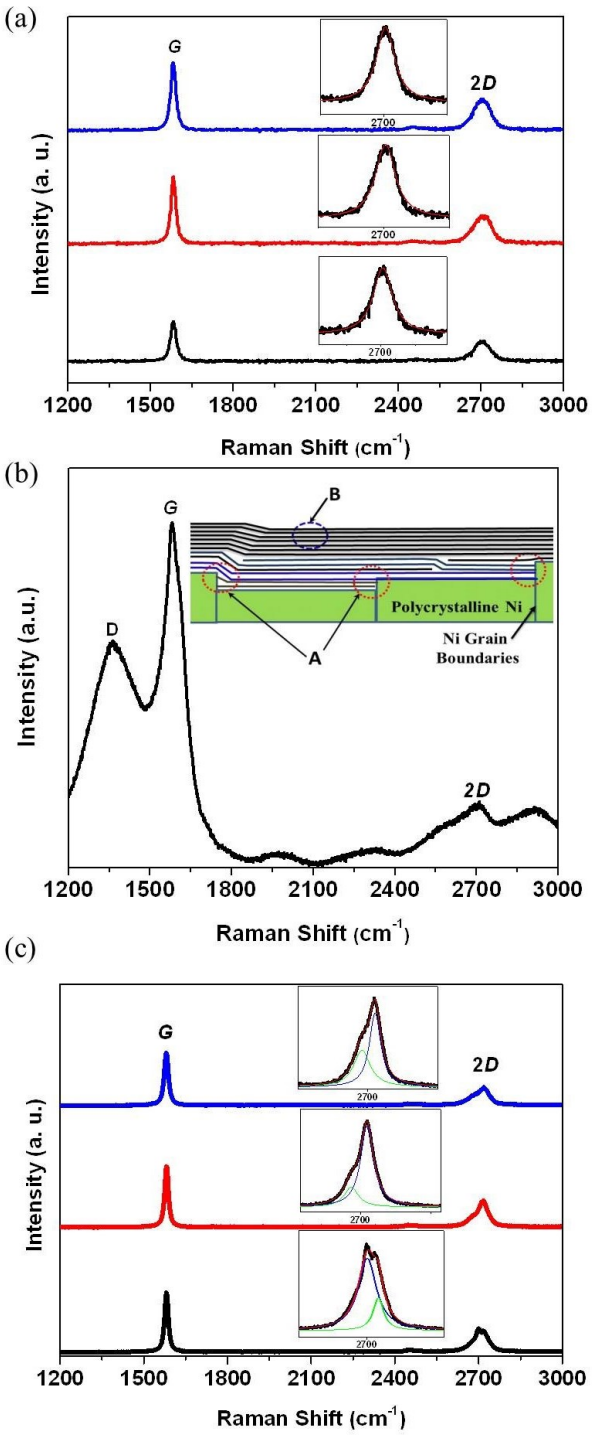

Figure 4.3 Raman studies on as-grown and transferred MLG. (a) Raman spectra from three representative areas of as-grown MLG on Ni (i.e. *before* transfer). The top plot (blue) is most commonly observed (~ 80% area). The 2*D* band is symmetric in all cases and can be fitted with single Lorentzian (*insets*). (b) Raman spectrum taken from the Ni/MLG interface after removing the Ni. Clear *D* peak is present, which confirms defective nature of this region. The inset shows schematic of graphene growth on Ni. Regions marked "A" (near Ni/MLG interface) are truncated by Ni grain boundaries and significant interfacial hybridization occurs in this region, which are the origins of defects in this region. But regions marked "B" (away from Ni/MLG interface) have continuous graphene layers covering the underlying layers. These layers are relatively defect free. (c) Typical Raman spectra of MLG (top layers) transferred on SiO_2/Si, from three representative regions. In all cases either splitting or shoulder in 2*D* band has been observed. No defect (*D*) peak has been observed in both as-grown and transferred MLG. Since the penetration depth of the Raman laser (2.33 eV) is ~ 50 nm and average sample thickness is ~ 60 nm, the Raman signal originates from the "defect free" region as described in Figure 4.3(a).

persists (Figure 4.4 (a)), indicating absence of any magnetic field induced metal-insulator transition effect. Also note that the $R_{zz}(0)$ values mentioned above are at

least an order of magnitude higher than the MLG/Ag contact resistance observed (see section 4.4.1). Thus Ni/MLG contact resistance does not play a significant role in the observed MR characteristics. Figures 4.4(b), (c) show normalized CPP MR [$R_{zz}(B)/R_{zz}(B = 0)$] of as-grown MLG on Ni in the field range ±8kG for $\theta = 0°$ (or 180°) and 90° (or 270°). As evident from Figures 4.4(b), (c), the CPP resistance of as-grown MLG on Ni is strongly dependent on the direction of the magnetic field (θ). When the magnetic field is normal to the graphene plane, i.e. $B \parallel I$ ($\theta =$ 0° or 180°), we observe ~ 40% drop in CPP resistance in the vicinity of 2kG (at 15K, Figure 4.4(b)). However, when the magnetic field is in-plane, i.e. $B \perp I$ ($\theta =$ 90°, 270°), we observed only a weak positive MR of ~ 8% (at 15K, within the measurement range of +/- 8kG, Figure 4.4(c)). Such MR features cannot be explained with any semi-classical theory since Lorentz force on charge carriers is negligible when $B \parallel I$ and strongest for $B \perp I$. These MR characteristics are however consistent with the ILMR picture described in section 4.2 and CPP MR measurements performed previously in as-grown MLG sample (Figure 3.2, Chapter 3).

One key characteristic feature of ILMR is the inverse dependence of CPP resistance (R_{zz}) on the out of plane component of the magnetic field (B_z). As discussed previously, such dependence is only valid in the "intermediate field" range, where only a single mode (but not necessarily the zero mode) participates in interlayer transport and high field effects as well as low field Landau level mixing effects [61] are absent. In Figure 4.4(d), we have plotted inverse of (normalized) interlayer resistance as a function of normal component of the magnetic field in the range where negative MR is most prominent ($B > B_{cr}$). A clear linear fit is observed at all measurement temperatures as expected from theory. Figure 4.4(d) *inset* shows temperature dependence of the critical magnetic field (B_{cr}). As expected, based on the discussion in section 4.2, $B_{cr} \propto T^2$, which is a signature of the ILMR effect. In this plot B_{cr} is the value of the magnetic field at which device resistance starts to decrease and this quantity is closely related to the width (full width half maximum) of the MR curves in Figure 4.4(b).

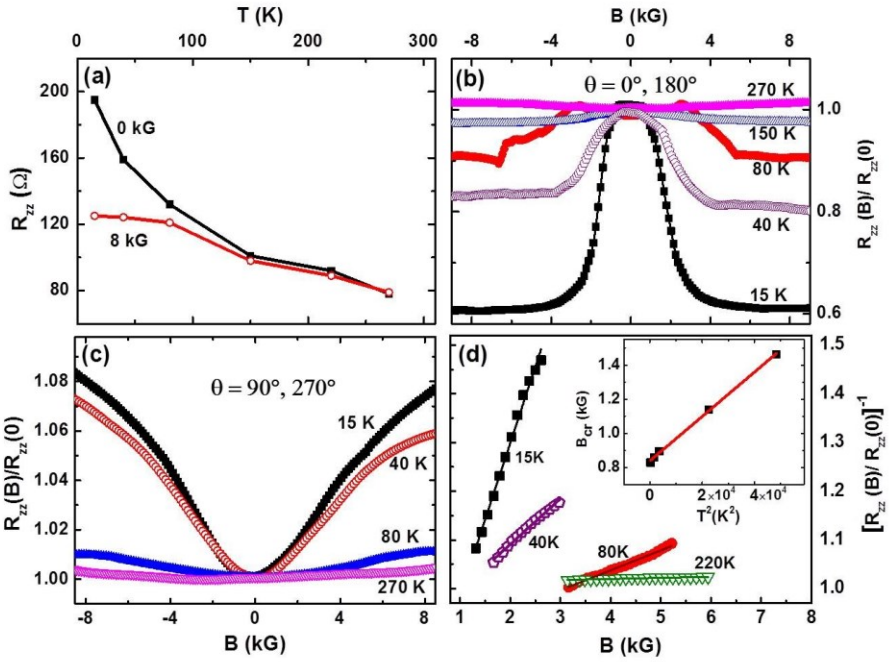

Figure 4.4 CPP MR characterization for out of plane ($\theta = 0^o, 180^o$) and in-plane ($\theta = 90^o, 270^o$) magnetic fields**.** (a) Temperature (T) dependence of CPP resistance $R_{zz}(T)$ in MLG/Ni samples at zero magnetic field and at 8kG (out of plane) over the temperature range 15 – 270K. Insulating behaviour is observed at both temperatures, along with a magnetoresistance effect. (b) Normalized CPP resistance ($R_{zz}(B)/R_{zz}(B = 0)$) at various measurement temperatures for $\theta = 0^o, 180^o$. A negative MR effect is observed. This effect weakens and MR curves broaden as temperature is increased. Critical field B_{cr} is the field value at which device resistance starts to drop significantly. (c) Normalized MR ($R_{zz}(B)/R_{zz}(B = 0)$) at various measurement temperatures for $\theta = 90^o, 270^o$. A positive MR is observed in this case. As before, MR effect weakens and MR characteristics broaden as temperature is increased. (d) Inverse of normalized CPP resistance $(R_{zz}(B)/R_{zz}(B = 0))^{-1}$ as a function of out-of-plane magnetic field (B) in the range where negative MR is most prominent. Clear linear fit is observed in all cases. The inset shows variation of B_{cr} as a function of T^2. A clear linear fit is observed.

Clear linear fit in the B_{cr}-T^2 plot, and absence of any saturation at low T implies that $\Gamma \propto k_B T$ even at the low T limit. Thus disorder induced broadening is not significant in the present case, which is also consistent with Raman characterization (Figure 4.3(a)).

As discussed above, MLG/Ag contact resistance does not play a major role in the CPP measurements. In section 3.3 (Chapter 3), we showed that the metal contacts (Ni and Ag) or the interfacial regions are not responsible for the observed negative

CPP MR in these samples. For example, unlike the actual devices the metallic contacts themselves show metallic temperature dependence of resistivity. Further the metallic contacts have significantly smaller resistance than the actual device. Characterization of the "defective layer" at Ni/MLG interface also revealed metallic temperature dependence (section 3.1.3, Chapter 3). Thus the observed CPP MR originates from the graphene stacks away from the Ni/MLG interface, as a result of the ILMR effect. As characterized in Figure 4.3 by Raman spectroscopy, these layers are indeed defect free and weakly coupled, which are necessary prerequisites for observation of ILMR. As described later (also see Figure 5.2 (a), Chapter 5), zero field resistance R_{zz} (B = 0) scales with MLG thickness, which further confirms that the CPP resistance originates from the "bulk" region of the MLG and not from the interfaces.

Figures 4.5(a), (b) show the angular (θ-dependent) response of CPP MR in MLG/Ni samples at 15K and 220K respectively. As consistent with the ILMR model described earlier, negative MR is strongest for θ= 0°, 180˚ (B normal-to-plane) and gradually weakens as θ is tilted away from this direction. The measured CPP resistance curves for θ, $180^{o} \pm \theta$ and $360^{o} - \theta$ are almost identical to each other, which is consistent with the expression of ρ_{zz} (θ) described earlier in this chapter. Decrease in negative MR with increasing tilt angle (θ) can be viewed as a result of a competition between the negative MR effect (due to B_z component) and a positive MR effect (due to in-plane components B_x, B_y), which becomes stronger at larger θ and larger $|B|$. Additionally, as described before, a positive MR effect arises at low field range ($B < B_{cr}$) as well where inter Landau level mixing takes place [61]. However, negative MR effect generally dominates at higher fields ($B > B_{cr}$) for small θ. Due to these competing effects, the MR characteristics tend to broaden as θ is increased, and often "shoulder"-like features are observed in the MR characteristics. As a result, B_{cr} as defined earlier, increases with θ. Physically, at a higher tilt angle, larger magnetic field needs to be applied to reduce Landau level overlap and overcome the resulting low field positive MR. In addition, increased

in-plane scattering at higher tilt angle can further enhance the Landau level mixing effect described in ref. [61].

Figure 4.5(c) shows the angle dependence of the critical field (B_{cr}) at two different temperatures. As expected, at both temperatures critical field shows an increasing trend with the angular deviation (θ). The negative MR and the interplay between positive and negative MR can be observed up to $\theta = 10^{o}$ (Figures 4.5(a), (b)) and then the positive MR completely overwhelms negative MR. In Figure 4.5(c), B_{cr} has been found to be higher for 220K as compared to 15K. This is expected due to the reasons described above.

Figure 4.6(a), (b) show angle dependence of the normalized MR over the entire range of 0^{o}–360^{o} for three different values of (fixed) field strengths ($B > B_{cr}$) at two different temperatures. The data shows 180° periodicity and identical sharp dips for tilt angles $\theta = 0^{o}$, 180^{o} and 360^{o}, both of which are consistent with the ILMR model. For a given field strength, device resistance increases as the tilt angle is increased with respect to the above-mentioned values. As described before, this increase arises from the Lorentz force due to the increased in-plane field component. However, the dips in the vicinity of these angles are sharper than that predicted by theory [38] (equations (1) and (2)), and device resistance tends to saturate at ~ 10^{o} deviation from the above-mentioned angles. According to the theory [38], change in resistance with angle (at a given field strength) is more gradual (Figure 4.6(c)). The reason for this discrepancy can be understood as follows.

The theoretical model described in equations (1) and (2) predicts a positive MR as θ is increased. This model considers carrier deflection in presence of a tilted magnetic field and resulting increase in effective interlayer tunnelling distance (or reduced overlap between the wave functions of the neighbouring layers), which causes the positive MR for $B > B_{cr}$. However, there is another factor that contributes to positive MR at higher fields. For example, tilted B implies more in-plane carrier scattering in the current path, which results in a positive MR [8] (also see Figure 4.8(a)). In a MLG stack containing ~100 layers or more, carriers undergo

significant in-plane scattering in each layer in presence of tilted B during interlayer transport, which can result in a significant positive MR. However, this effect was not considered in equations (1) and (2), and as a result these equations underestimate the effect of the tilt angle on the observed MR.

As noted in Figure 4.4(b), MR at $\theta = 0$ is smaller than that reported previously in Figure 3.2 (Chapter 3). This difference can be attributed to the thickness of the MLG considered or the number of graphene layers participating in interlayer transport. For thicker samples (~ 200 nm), such as in Figure 3.2, $R_{zz}(B = 0)$ is large (~ 650 Ω) due to large number of weakly coupled graphene layers along the out of plane direction. In this case, $R_{zz}(B$=8kG) is significantly small due to an abundance of carriers generated in a large number of graphene layers. As a result, very strong negative MR effect was observed in thicker MLGs, with a factor of ~ 160 drop in device resistance as shown in Figure 3.2. However, in the present case we have used thinner MLG (~ 60 nm), which resulted in smaller zero field resistance R_{zz} (B = 0) ~ 200 Ω. In presence of 8kG field, carriers will be generated but in fewer numbers due to fewer number of graphene layers. As a result, weaker MR effect will be observed for thinner samples, which is consistent with our observation. It is important to note that zero field CPP resistance scales with MLG thickness for the same contact area, which confirms that zero field resistance originates from the "bulk" (or the "defect free region") and not from the contacts or the interfaces. In next section, as described earlier, we have further characterized the transferred MLG using various electrical measurements. These measurements demonstrates the electrical quality of as-grown MLG stack used in this study.

4.4 In-plane Electrical Characterization of Transferred MLG

In section 4.2, we reported characterization of as-grown and transferred MLG (both surfaces) using Raman spectroscopy (Figure 4.3). This method is widely used for characterization of graphitic nanostructures (graphene, graphite, carbon nanotubes etc.) due to its non-destructive nature and the wealth of information that can be obtained from such measurements [34], [73]. In section 4.2, we have shown that

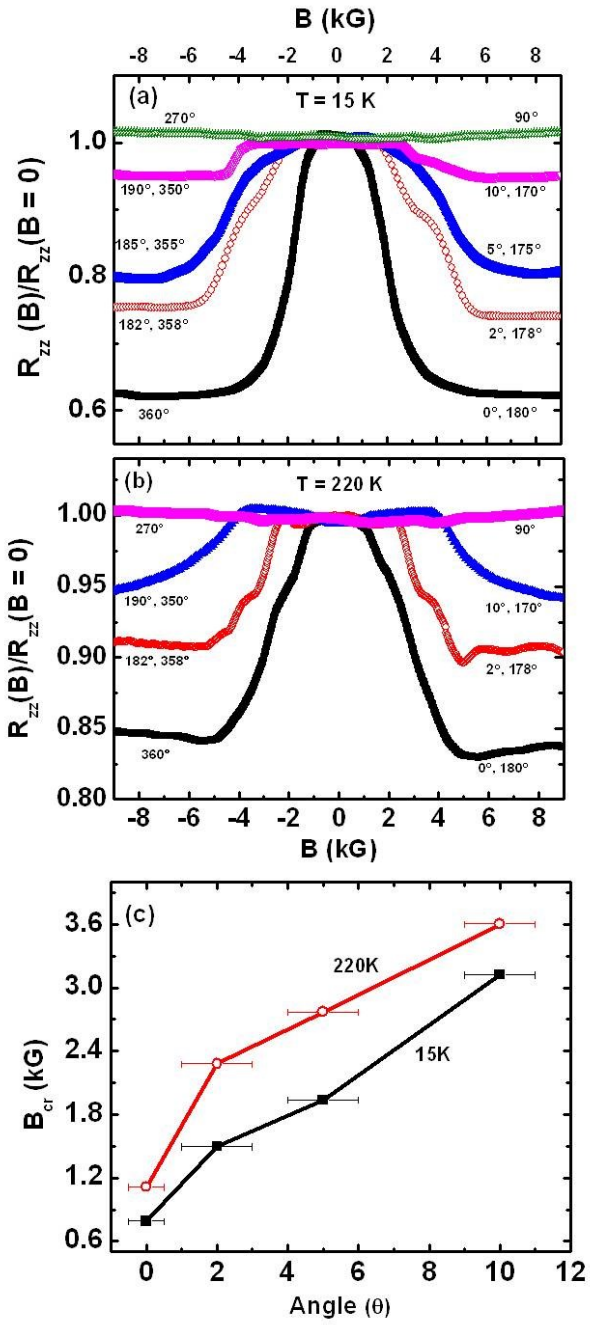

Figure 4.5 Angle dependence of CPP MR. (a), (b) Normalized CPP resistance ($R_{zz}(B)/R_{zz}(B = 0)$) of as-grown MLG on Ni at various orientations of the magnetic field (θ) at two different temperatures (15K and 220K). The negative MR gradually decreases as tilt angle θ is increased. (c) Critical field (B_{cr}) as a function of θ at 15K and 220K. Critical field is higher at higher temperature and increases with the tilt angle.

our as-grown samples (on Ni, not transferred) typically show formation of prominent hexagonal lattice of carbon atoms (strong *G* peak), weak interlayer coupling (symmetric 2*D* band), and absence of any defect (absence of *D* band). After transferring on SiO_2 substrate, 2*D* Raman band becomes distorted, indicating loss of weak interlayer coupling as a result of the transfer process. Such change is not surprising since there are several recent reports that have unearthed various non-idealities of the transfer process[111], [138]. Nevertheless, to further characterize our samples, we have performed in-plane electrical measurements on the transferred specimens. Details of these measurements are described below.

4.4.1 Sheet Resistance and Contact Resistance Measurements.

Sheet resistance (R_s) of the transferred MLG has been measured using two methods. First, a "Transfer length (TLM) method" has been employed, from which sheet resistance (R_s) and contact resistance (R_c) have been evaluated. The typical device geometry is shown in Figure 4.7(a). The electrical contacts used in TLM measurements are labeled as A, B, C, D in Figure 4.7(a**)**. From the TLM measurement (Figure 4.7(b)), R_s is < 100 Ω/□ and R_c is < 10 Ω within temperature range of 10K – 290K. **Table 1** lists the typical R_s and R_c values at two different sample temperatures.

Next, a van der Pauw geometry has been used to extract R_s following a standard procedure [139]. Typical measurement configuration is shown in Figure 4.7(a) and the electrical contacts for this measurement are labeled as 1, 2, 3 and 4. At T = 30K, R_s = 87.5Ω/□, whereas at 80K and 200K R_s takes values 78 Ω/□ and 50.7 Ω/□ respectively. These values are consistent with those extracted by the TLM method (see **Table 1**) and give us confidence about the reliability of these numbers.

We note that such values of R_s are typical for CVD grown MLG of similar thickness (on Ni), and similar values have been reported by several groups in the past [136], [137]. Thus, electrical quality of our Ni-grown MLG samples is on a par with those reported in literature.

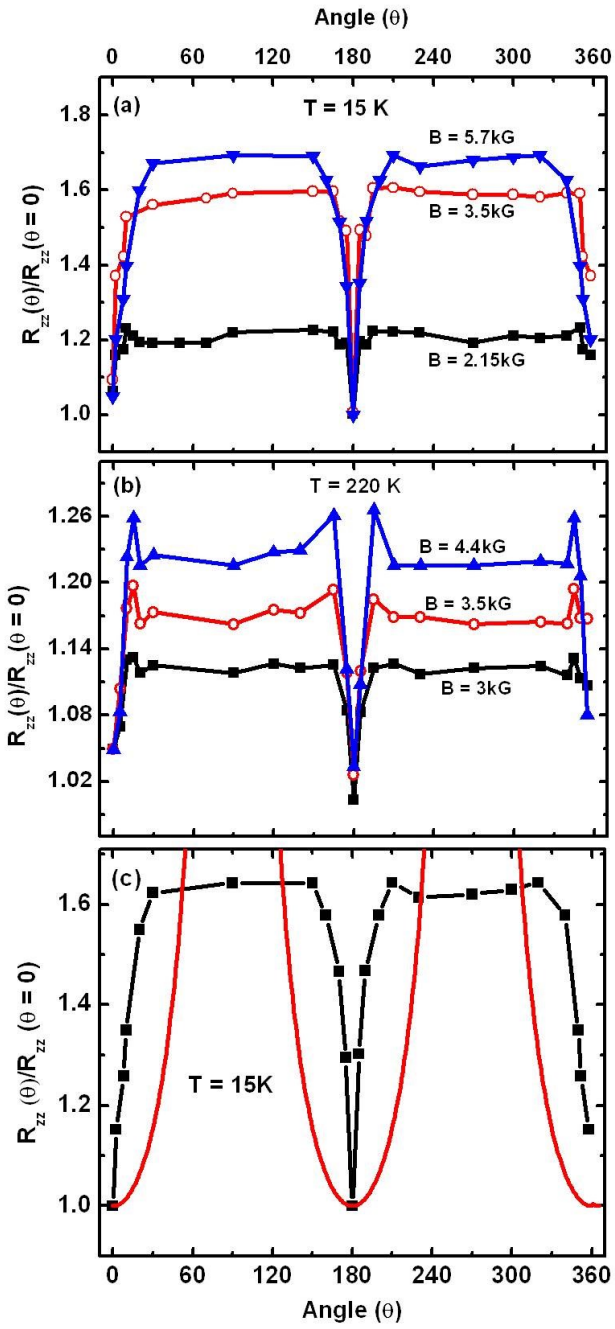

Figure 4.6 Angular dependence of CPP resistance $R_{zz}(\theta)$ at various field strengths. (a), (b) Data at 15K and 220K respectively. Three different field values are chosen, which are higher than B_{cr}. For a given field strength (B), device resistance at angle θ is normalized by the resistance value at $\theta = 0^{o}$, which also coincides with the resistance value at $\theta = 180^{o}$. As the tilt angle is increased with respect to 0^{o} (or 180^{o}), device resistance increases and ultimately saturates for $\theta > 10^{o}$. (c) Experimental data (black line with data points) shows sharper angular dependence compared to theory (red, smooth curve). The data corresponds to $B = 5.7$ kG.

Note that such low R_s films are often used as flexible, conductive and (semi)-transparent electrodes in flexible optoelectronic applications Thus Ag/MLG contact resistance does not play an important role in the observed MR.

4.4.2 In-plane MR Characterization of Transferred MLG – Weak Localization.

As discussed before, graphene layers near the top surface are almost defect-free, since no defect-induced peak has been observed in the Raman spectrum (Figure 4.3 (a)). To further test this point, we performed temperature-dependent in-plane magnetoresistance measurements on these samples (Figure 4.8). It is well known that the presence of grain boundaries and defects leads to weak-localization effect due to scattering of carrier wave functions [56]. However, no such effect has been observed in our Ni-grown MLG samples (after transferring on SiO_2, (Figure 4.8(a)), which is consistent with the Raman data (Figure 4.3(a)) that does not indicate any presence of defects or scattering centers.

On the other hand, we have measured in-plane magnetoresistance of Cu-grown samples (Figure 4.8(b)), which shows pronounced weak localization effect. This is consistent with observation of strong defect peaks in the Raman spectra of Cu-grown samples (Figure 4.8(c)), which originate from the grain boundaries. Thus the top layers of our Ni-grown samples indeed have very low defect content.

Table 1 Contact and sheet resistances (R_c and R_s) using TLM and van der Pauw methods.

Temperature (T)	**R_c (TLM method)**	**R_s (TLM method)**	**R_s (van der Pauw method)**
30K	7.9 Ω	98.7 Ω/□	87.5 Ω/□
200K	2.9 Ω	36.7 Ω/□	50.7 Ω/□

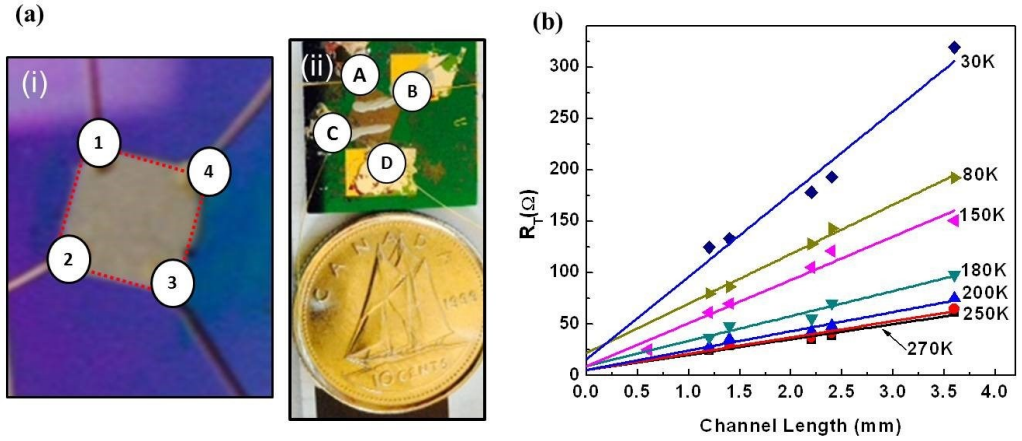

Figure 4.7 Electrical characterization of MLG transferred on SiO_2/Si. (a), (i) Typical van der Pauw geometry and (ii) TLM geometry. (b) TLM data, from which Ag/MLG contact resistance (R_c) and MLG sheet resistance (R_s) have been extracted.

4.4.3 Shubnikov-deHaas Oscillations in the in-plane MR Measurements.

The occurrence of ILMR as observed in as-grown MLG samples (Figures 4.4(b), 4.5(a), (b)) relies on formation of distinct Landau levels in presence of an out-of-plane (i.e. parallel to the c axis) magnetic field (B_z). Due to in-plane scattering, Landau levels are broadened ($E_{LL} \pm \Gamma/2$) and for small values of magnetic field, inter-Landau level separation ($\Delta_{LL}(B_z)$) is small. As a result, for small magnetic field values Landau levels are not distinct ($\Delta_{LL}(B_z)) < \Gamma$). However, as magnetic field strength is increased, inter-Landau level separation increases, eventually resulting in distinct Landau levels (($\Delta_{LL}(B_z)) > \Gamma$). Formation of distinct Landau levels leads to oscillations in in-plane resistance at higher B_z values, which is commonly known as Shubhnikov-deHaas oscillations [140]. Prior works on various graphitic systems have reported observation of such oscillations for $B_z \geq 0.6$T [141]–[143], and the oscillations increase in amplitude as magnetic field is increased. This occurs because higher magnetic field leads to larger separation between the neighboring Landau levels. At the same time, oscillation amplitude decreases with increasing temperature because at higher temperature scattering induced broadening is larger due to thermal excitations.

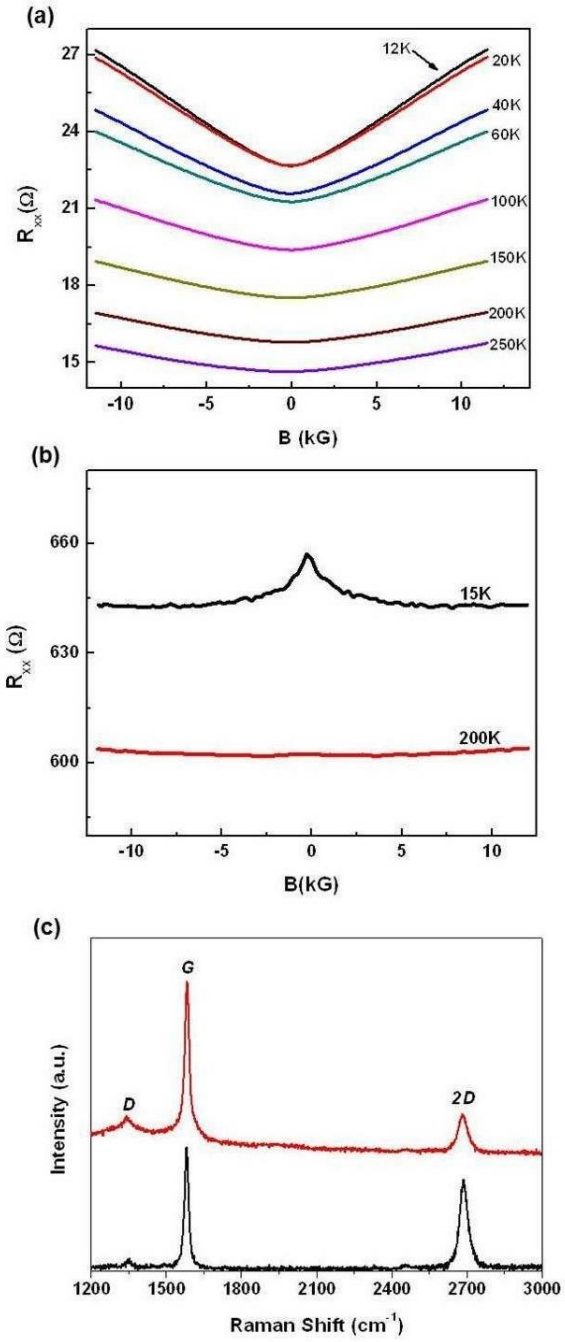

Figure 4.8 In-plane MR characterizations. (a) In-plane MR from MLG (top surface), transferred on SiO_2/Si, at various temperatures. Positive MR has been observed at all temperatures. No negative MR due to weak localization effect has been observed near $B = 0$. (b) In-plane MR from 8-layer transferred graphene (Cu-grown). Clear negative MR due to weak localization effect has been observed near $B = 0$. As expected, this effect disappears as temperature is increased. (c) Typical Raman data from 8-layer, Cu-grown graphene. Defect induced Raman peak (*D*-peak) is present, which originates from the grain boundaries. Weak localization effect observed in (b) is due to these grain boundaries.

To explore if Landau levels are formed within our measurement range of ±1 T, we have performed in plane magnetoresistance measurements on our transferred samples (CVD grown on Ni and subsequently transferred on SiO_2). Figure 4.8(a) shows the raw data (solid curves) at various measurement temperatures. To explore the presence of any underlying oscillation in the measured field range, we have fitted the experimental curves by monotonic backgrounds (Figure 4.9(a)). Figure 4.9(b) shows the residues after subtracting the background from the experimental data. A clear oscillatory behavior has been observed within our measurement range of ±1 T. As expected, the oscillation amplitude increases as field is increased and the oscillation amplitude is weakened as temperature is increased. However, phase and periodicity of oscillation remain almost unchanged. Oscillations have been detected up to T = 250K. Thus, distinct Landau level formation takes place within our measurement range of ±1 T, which is consistent with prior experiments on graphitic specimens [141]–[143].

Using the SdH data, carrier concentration per layer is estimated [9] to be ~ $10^{10}/cm^2$. Since the observed ILMR effect (main paper) manifests at ~ 2 kG, we can estimate the number of occupied Landau levels at this field value. Using the standard formula [140] (number of Landau levels = $(n_S)_{1L}/[2eB/h]$), we find that ~ 1-2 Landau levels are occupied. Thus, our devices operate very close to the so-called "quantum limit".

4.5 Conclusion

In this chapter, we have presented experimental measurement of interlayer magnetoresistance effect in a vertical stack of randomly oriented graphene layers (or, turbostratic graphite). Temperature, field and angular dependences of this effect agree well with theory. The angular response is sharper than expected and is related to the additional sources of positive MR present in the system. In graphitic systems such as above, this effect persists at temperatures much higher than that reported for α-(BEDT-TTF)$_2$ I_3, presumably due to higher Fermi velocity in graphene (~10^6m/s, as opposed to ~10^5m/s for α-(BEDT-TTF)$_2$ I_3), which leads to larger

separation between the Landau levels. At the same time, this also explains why this effect is observed at a much lower field (~ 0.2 T) in MLG as compared to α-(BEDT-TTF)$_2$ I$_3$ (~ 2T). Due to the strong MR signal at higher temperatures and lower field range, this effect is promising for next generation of flexible memory and sensor devices. In the next chapter, we will explore thickness dependent ILMR effect in as-grown MLG on Ni systems that provide additional proof that the observed large negative MR due to ILMR is originated from bulk MLG stack, but not from interfaces or contacts.

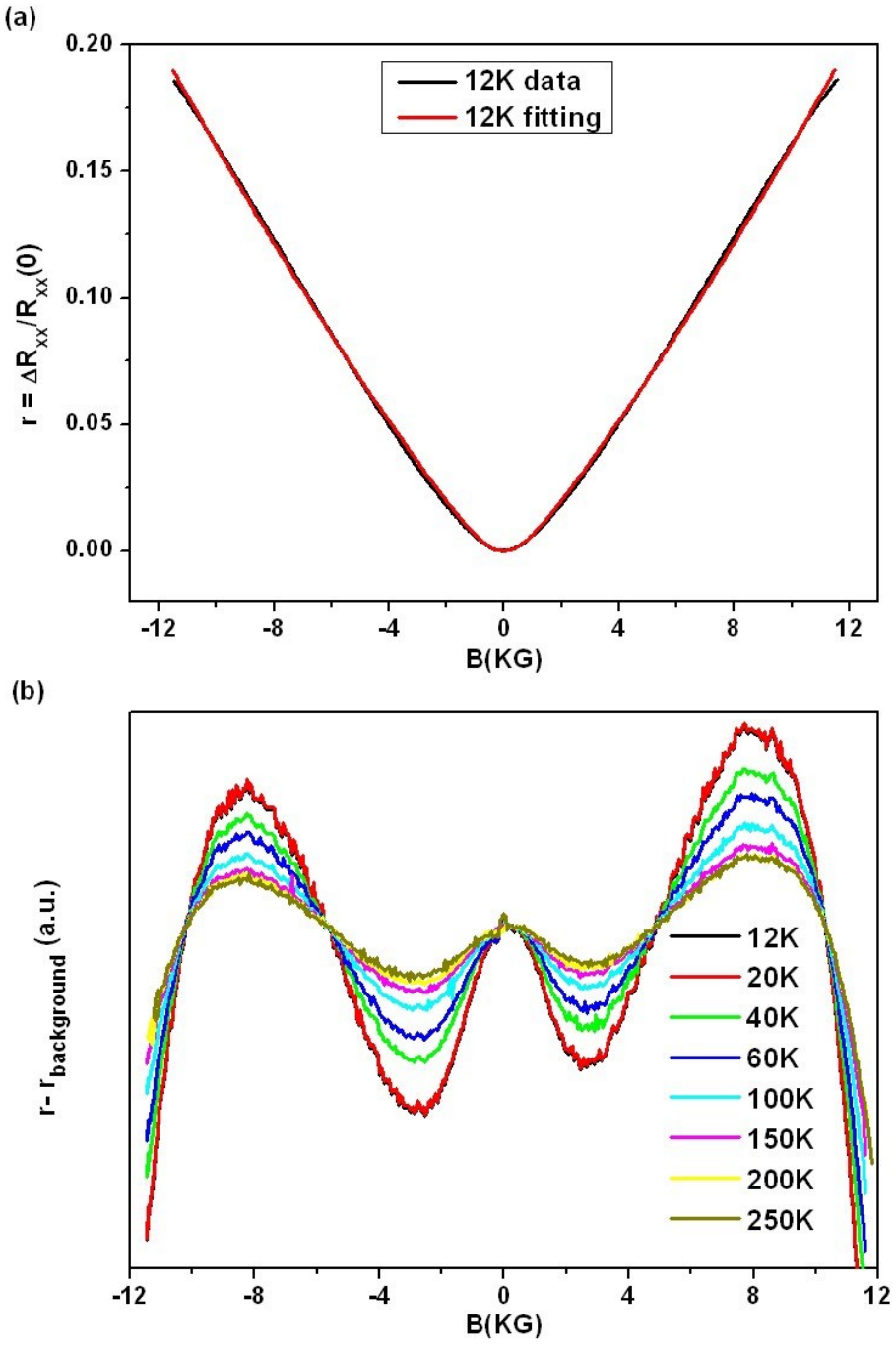

Figure 4.9 Shubnikov-deHaas oscillations in in-plane MR of Ni-grown MLG transferred on SiO_2/Si. (a) Typical MR plot at 12K (black line) and smooth monotonic background (red line). (b) MR at various temperatures after removing the smooth background. MR oscillations have been observed, which increase in amplitude as B is increased. Also, oscillation amplitude decreases as T is increased.

5 THICKNESS DEPENDENT INTERLAYER MAGNETORESISTANCE (ILMR) IN CVD GROWN MLG[7]

As described in previous chapters, CVD grown multilayer graphene (MLG) exhibits large out of plane magnetoresistance (MR) due to interlayer magnetoresistance (ILMR) effect. It is essential to identify the factors that influence this effect to explore its potential in magnetic sensing and data storage applications. It has been demonstrated in chapters 3 and 4 that the ILMR effect in as-grown MLG on Ni is sensitive to the interlayer coupling and the direction of magnetic field. In this chapter, we investigate the role of MLG thickness on ILMR effect. This study provides further evidence that the observed large negative MR in as-grown MLG is due to ILMR and not from interfaces or contacts. For this, we performed current perpendicular to plane (CPP) MR measurements on three sets (S1, S2, S3) of MLG devices with different average thicknesses: (a) 60 nm, (b) 200 nm and (c) 300 nm. In the following sections, we outline the device fabrication steps and characterization of MLG stacks used in this study.

5.1 Fabrication and Characterization

We used low pressure chemical vapor deposition (LPCVD) process (section 2.1.1, Chapter 2) to grow MLG on catalytic Ni substrate of thickness ~25μm. To grow MLG with different thicknesses, we systematically varied the concentration of carbon containing species (methane, in our case) from 0.1% to 0.3 % in the CVD process by keeping all other parameters unchanged. This affects the amount of dissolved and precipitated carbon during the CVD process, and results in MLGs with different nominal thicknesses. A detailed description of the CVD process has been presented in section 2.1.1 (Chapter 2). Similar to our previous samples, the structural quality and uniformity of as-grown MLG samples have been investigated by Raman spectroscopy (with laser excitation wavelength of 532nm) and in-built

[7] Results described in this chapter have been submitted for publication & are currently under review [99].

optical microscopy. As mentioned before, the estimated penetration depth of Raman laser within graphite is ~ 50 nm [84], and hence Raman data reveals the quality of the graphene layers within this thickness range. Raman spectra of as-grown MLG samples (on Ni) with different average thickness of MLG are displayed in Figures 5.1 (a), (b) and (c). These samples exhibit strong *G* peak at 1580 cm^{-1} and a symmetric 2*D* band around 2700 cm^{-1} (Figures 5.1 (a), (b) and (c)). As described earlier, the strong *G* peak implies formation of hexagonal graphene lattice in all cases. The symmetric 2*D* band has been observed over entire MLG surface, which confirms weak interlayer coupling over an extended volume of the samples [34], [96]. The absence of defect (*D*) peak at 1350 cm^{-1} in all of our as-grown MLG samples indicates high structural quality and negligible defect density, at least within ~50 nm (penetration depth of the Raman laser) from the top surface. These features are common for all three batches of MLG samples considered in this study and also consistent with the Raman spectra of samples previously used for CPP MR studies (Figures 2.7, 4.3 (a)). In Figure 5.1(d), typical Raman spectrum of MLG/Ni interfacial layers of a transferred MLG sample is shown. Strong defect (*D*) peak is observed from these interfacial layers and this feature is again common for all three batches used in this study. As described earlier in section 4.2 (Chapter 4), this defect peak originates due to two reasons: (1) it is well known [85] that the 3*d* states of Ni hybridize strongly with the $2p_z$ states of carbon atoms, which results in disappearance of the Dirac cone dispersion, opening of a band gap and creation of defect states in the band gap and (2) Ni surface has grain boundaries with atomic scale discontinuities, which result in small area graphene growth near the interface and creation of edge states [134], [135]. However, these defects are non-existent as one moves away from the Ni/MLG interface. We demonstrated in previous chapters that hybridization effect only affects the interfacial layers and the layers away from the interface are not affected by this effect. Similarly, top layers tend to grow continuously over the (small area) bottom layers, without creation of any edge states. As a result, the top layers do not exhibit any *D* band in the Raman spectra. The wrinkles observed in Figures 5.2(b), (c) and (d) as discussed earlier in section 4.2 (Chapter 4), originate from the small area graphene layers at the interface.

To estimate nominal thickness of these as-grown MLG samples, we performed step height measurements after transferring MLG stack on SiO_2/Si substrate. A detailed description of the transfer process has been presented in section 2.1.3 (Chapter 2). Optical images of the transferred samples are displayed in Figure 5.2. The typical thickness distributions of the transferred MLG samples are shown in the insets of Figures 5.2 (b), (c) and (d). From these distributions, the average thicknesses of the three batches are estimated to be (*i*) ~ 60 nm (batch S1), (*ii*) ~ 200 nm (batch S2) and (*iii*) ~ 300 nm (batch S3).

Based on our earlier discussions on the Raman spectra (Figure 5.1) and our previous studies (sections 3.1, 4.1), we conclude that as-grown MLG on Ni consists of two regions: "defective" region that shows Raman *D* peak and a "defect-free" region that does not show any Raman *D* peak. The layers in the defect-free region are weakly coupled as evidenced by the distortion-free 2*D* Raman band as seen in Figure 5.1. The defective interfacial region shows metallic temperature dependence ($dR_{zz}/dT > 0$) due to presence of Ni atoms and/or conductive "edge states" at the missing atom sites. The defect-free region, on the other hand, exhibits insulator-like temperature dependence ($dR_{zz}/dT < 0$). We observed that the charge transport characteristics of as-grown MLG samples with thickness ≤ 30 nm were dominated by the defective interfacial region (Figure 3.7, Chapter 3). Therefore, in this study we only considered samples with as-grown MLG thicker than 50 nm to ensure that the CPP resistance is dominated by the defect-free region. It is important to note that the transferred samples generally show distorted 2*D* Raman band, which is a signature of strong interlayer coupling and hence ILMR has not been observed in the transferred samples. In next section, a detailed thickness dependent CPP MR in CVD grown MLG on Ni is presented and discussed the results.

5.2 Thickness Dependent CPP MR in CVD grown MLG on Ni

The device geometry of samples used in this study is similar to our as-grown MLG devices used previously for CPP MR studies (Figure 5.2(a) *inset*). The catalytic Ni substrate and silver epoxy have been used as bottom and top contacts respectively. The top contact area is ~1mm^2 and is carefully placed at the center of top MLG

surface to maintain uniform current distribution during CPP measurements. A constant DC current bias of 1mA has been used in all MR measurements. The total CPP resistance of the device is a serial combination of contact resistance (R_{cont}), resistance from defective interfacial region (R_{def}) and the "bulk" interlayer resistance (R_{int}) as shown in Figure 5.2(a). Both R_{cont} and R_{def} exhibit metallic temperature dependence as described above and are almost identical for the three batches considered in this study. It has been independently verified (Figures 3.7 & 3.9, Chapter 3) that the R_{cont} and R_{def} vary in between 2-4 Ω and 6-7 Ω respectively (at zero field). However, the (zero field) CPP resistance of our samples exhibit insulator-like temperature dependence and it is at least two orders of magnitude larger than R_{cont} and R_{def}. Therefore, the overall CPP resistance is dominated by the interlayer resistance (R_{int}) component. To further verify this, we compared the zero field CPP resistance of MLG samples (same contact area) with different thicknesses (Figure 5.2(a), main image). The CPP resistance has been found to increase with MLG thickness. This indicates that CPP resistance R_{zz} is Figure 5.3(a) shows typical CPP MR of a thinner (~60 nm) MLG stack in the temperature range 50 – 200K. The zero field resistance of this sample is ~ 200 Ω at 50K which gradually decreases to 100 Ω at 200K. The sample clearly shows strong insulator-like temperature dependence ($dR_{zz}/dT < 0$) at zero field. CPP MR is ~ 40% at 50K (over the entire field range of 10 kG) and magnitude of the negative MR drops gradually with increase in temperature. MR effect is barely perceptible at 200K and vanishes above this temperature and hence data above this temperature are not shown. Switching field (B_{sw}), the field value at which the CPP resistance sharply drops, increases gradually with increase in temperature. For this study, B_{sw} is taken to be the full-width-half-maximum (FWHM) of the negative MR curves as previously used in Figure 3.12 (Chapter 3). With increasing temperature, negative MR broadens and hence B_{sw} increases. At higher temperatures, the low-field positive MR dominates over the negative MR due to enhanced Landau level mixing, which is responsible for the increase in B_{sw} and hence broadening of the MR curves [61] dominated by the "bulk" region of the sample and not by the interfaces or the contacts.

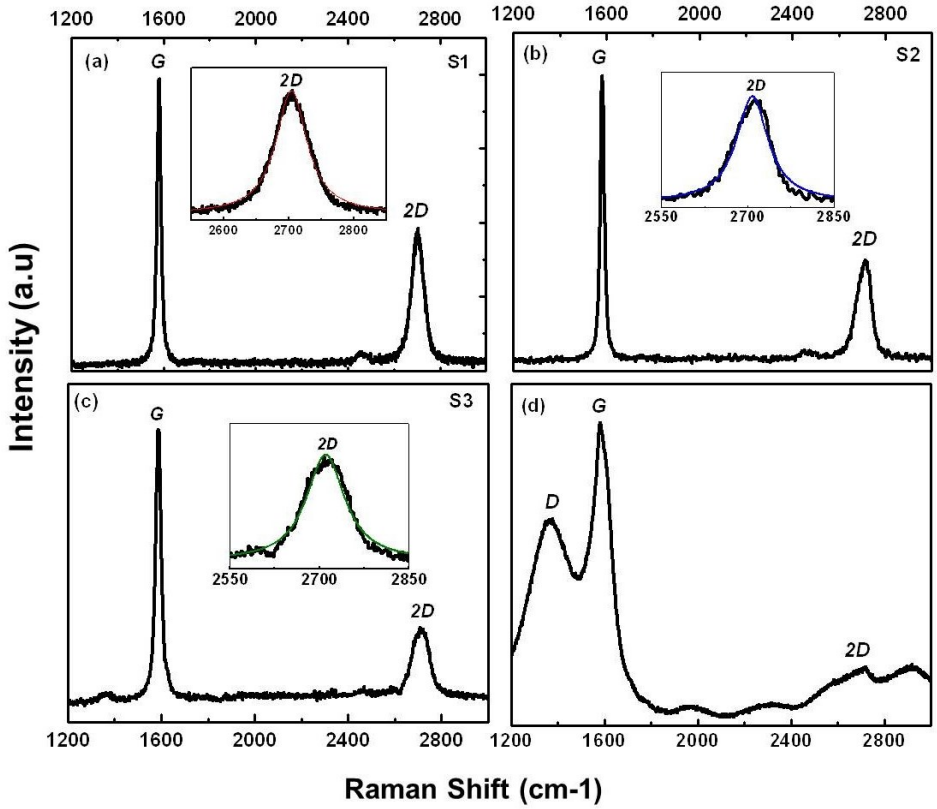

Figure 5.1 Typical Raman spectra of as-grown MLG (taken from the top surface i.e. from the "defect free region") with nominal thicknesses of (a) ~ 60 nm (batch S1), (b) ~ 200 nm (batch S2) and (c) ~ 300 nm (batch S3). (d) Typical Raman spectra of layers at the MLG/Ni interface ("defective region"). As seen from figures (a)-(c), defect (*D*) peak at 1350 cm^{-1} is absent in all these cases. The Raman 2*D* band of each batch is symmetric and can be fitted with a single Lorentzian as shown in the *insets* of figures (a), (b) and (c). In figure (d) strong *D* peak is observed from the transferred MLG sample, taken from the bottom surface. This confirms the defective nature of the interfacial layers. This is consistent with the previous observation in Figure 4.3(b).

Interestingly, in the low temperature (50K) scan in Figure 5.3(a), an oscillatory MR component has been observed for field values ~ 4 kG and larger. Such oscillations are reminiscent of Shubnikov-deHaas (SdH) oscillations that are often observed in graphitic systems [141]–[143]. In our case of CPP charge transport, such oscillations imply that the Fermi level is not located at the Dirac point (or, at the zero-mode Landau level), as a result of unintentional doping of the graphene layers during the fabrication process. In this case, CPP resistance will exhibit a valley at field values for which a Landau level coincides with the Fermi level, since under

this condition ample states will be available for interlayer tunneling. However, at other field values Landau levels will not coincide with the Fermi level, which will result in a peak in the MR oscillations due to lack of available states for tunneling. In the low field range ($B < B_{sw}$ i.e. before resistance switching due to negative MR), inter Landau level spacings are not enough to overcome Landau level broadening, and hence states are available in the vicinity of the Fermi level. This leads to finite

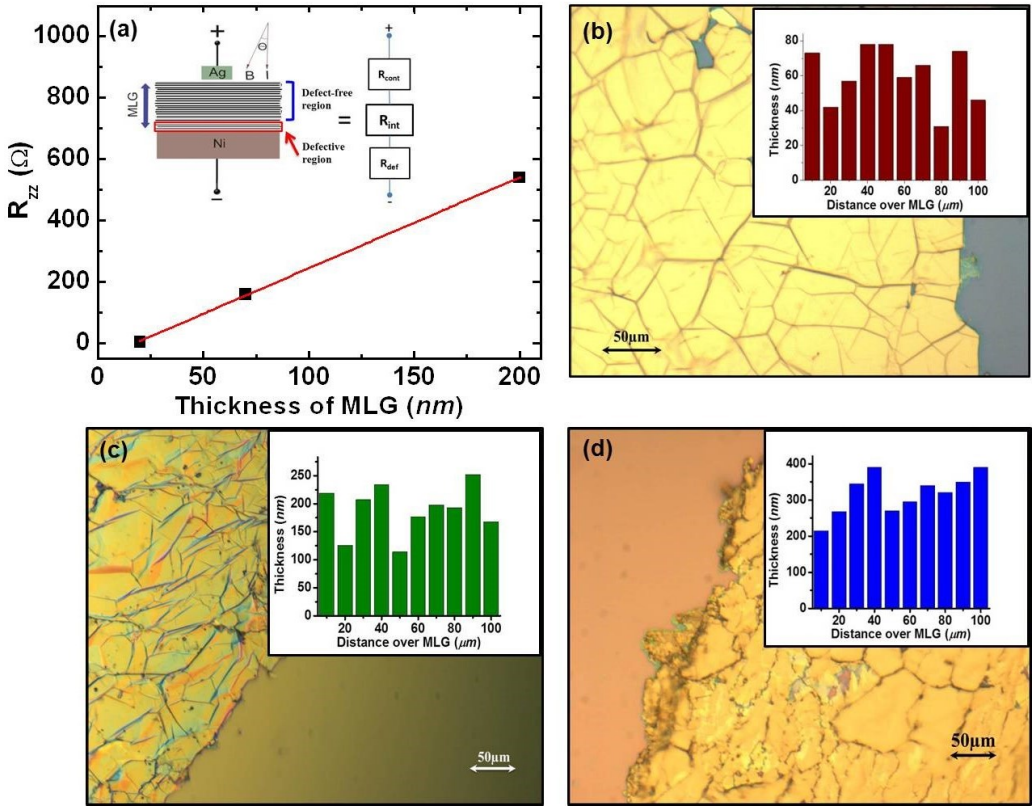

Figure 5.2 Thickness dependent zero field CPP resistance $R_{ZZ}(0)$ and optical images of transferred MLG. (a) Zero field resistance R_{ZZ} (0) vs. MLG thickness. R_{ZZ} (0) increases with increasing MLG thickness. This indicates that the overall resistance of the device is dominated by the "bulk", not the interfaces, and the contacts. The inset shows device schematic and an equivalent circuit model of the device. As discussed in text, the combination of contact resistance and defective region resistance (R_{cont} + R_{def}) of all three sets of samples is < 10Ω, and shows metallic temperature dependence. The overall device, however, shows semiconducting temperature dependence. This proves that R_{cont} + R_{def} does not play a dominant role in the CPP measurements. Optical images of the three transferred MLG samples are presented in Figures (b) 60 nm (batch S1), (c) 200 nm (batch S2) and (d) 300 nm (batch S3). *Insets* show typical thickness variations in these samples.

resistance values in the low field range. Also, in this low field range, due to inter Landau level mixing, a positive MR effect is present, which offsets the negative MR and results in a weak overall MR. As the magnetic field is increased, inter Landau level spacings increase resulting in reduced inter Landau level mixing and around $B = B_{sw}$ the negative MR dominates the positive MR. We note that complete separation of the Landau levels is not necessary for observation of the negative MR. The negative MR should manifest whenever n -> n tunneling dominates n -> n' ($n \neq n$') tunneling. From the locations of the consecutive valleys in the MR oscillations in Figure 5.3(a), Landau level $n \sim 4$ is estimated to be occupied at field value $B \sim$ 0.5T [140]. The inter Landau level spacings $E_5 - E_4$ and $E_4 - E_3$ are computed as 69.8K and 79K respectively and spacings between the lower order Landau levels are even higher. Clearly, MR oscillations are expected to occur at 50K (assuming thermal broadening to be $\sim k_B T$) and are expected to gradually disappear as temperature is increased beyond 80K. At these higher temperatures, increased thermal broadening makes the Landau levels indistinguishable.

Figure 5.3(b) displays the typical CPP MR of a thicker (~ 200 nm) MLG sample at three different temperatures. The zero field resistance of this sample is 480Ω at 50K which gradually decreases to 190Ω at 220K. Clearly, this sample also shows insulating temperature dependence at zero field. Also noteworthy is the increase in zero field resistance as compared to the thinner samples described above (both have nominally identical contact area). This implies that the CPP resistance originates from the graphene layers in the MLG "bulk" and not from the contacts or the interfaces. Unlike thinner MLG sample in Figure 5.3(a), the negative MR in this case is larger, ~ 92% at 50K, and the negative MR clearly persists even at higher temperatures (~ 220K). As before, signs of high field oscillations have been observed in this sample for field values exceeding 4kG. From the oscillations, we estimate Landau level $n \sim 3$ to be partially occupied at $B \sim 0.5$ T. At 50K and $B \sim$ 0.5 T, Landau levels $n = 0 - 3$ are completely separated and hence such oscillations are expected. However, at ~ 150K and higher, thermal broadening is larger than the inter Landau level spacings and oscillations are washed away.

As noted above, in figures 5.3(a) and 5.3(b), MR effect is weak in the low field regime (~ 0–3kG range) and the sharp negative MR manifests outside this range. This is attributed to a positive MR effect that is strong at the low field range and offsets the negative MR mechanism. As described earlier in Chapter 4, the positive MR can originate from two sources: (1) at low field, inter Landau level separation is smaller than Landau level broadening and significant inter Landau level mixing takes place. It has been shown in ref. [61] that such inter Landau level mixing can produce positive MR effect in the low field range. (2) Carriers undergo in-plane motion during interlayer transport. The in-plane component of charge transport exhibits positive MR [8]. Clearly, these effects become stronger with increasing temperature and widens the negative MR (or, increases B_{sw}).

The negative MR effect in the $B \parallel I$ geometry is even more dramatic for the samples with larger thickness, ~ 300 nm (Figure 5.3(c)). These samples exhibit very high zero field interlayer resistance (≈100MΩ or higher) often exceeding the upper limit of our measurement system (100MΩ). Again, we note that such increase in zero-field interlayer resistance (with the same contact area) is correlated with the increase in MLG stack thickness. Interestingly, as shown in Figure 5.3(c), a relatively small perpendicular magnetic field of ~3kG reduces the interlayer resistance by several orders of magnitude, leading to a giant MR with a switching ratio ($R_{zz}(0)$ / $R_{zz}(B)$) of ~ 10^7. Discontinuity in the vicinity of the zero field represents the range where the device resistance exceeds our instrumental limit. Unlike thinner specimens, this effect persists at room temperature and has been recorded up to ~ 320K. To our knowledge, such strong negative MR has not been reported before in graphitic or any other system at comparable temperature and field range. At the lowest measurement temperature (10K), strong MR oscillations have been observed, and Landau level n ~ 2 is estimated to be occupied. Under these conditions inter Landau level separation is larger than thermal broadening and hence oscillations are expected. The *inset* of Figure 5.3(c) shows the *I-V* characteristics of these thicker samples at two different field values, which clearly demonstrates a giant field dependent resistance switching.

5.3 Discussion

A qualitative understanding of the thickness dependence of MR can be obtained as follows. MR ratio is primarily determined by the quantity $R_{zz}(0)/R_{zz}(B)$. The quantity $R_{zz}(0)$ depends strongly on the number of layers in the stack and also on the strength of the interlayer coupling. Weaker interlayer coupling is expected to increase the value of $R_{zz}(0)$. As consistent with our experimental data presented above, thicker MLG stack results in larger $R_{zz}(0)$. On the other hand, the quantity $R_{zz}(B)$ depends on the number of carriers generated per unit volume in presence of a perpendicular magnetic field. Larger number of graphene layers in the MLG stack should result in an abundance of charge carriers and available states for interlayer tunneling and thereby smaller $R_{zz}(B)$ compared to the thinner layers. Combining these observations, stronger negative MR is expected in thicker MLGs.

Figure 5.3(d), *top inset*, shows B_{sw} as a function of temperature for all three thicknesses considered in this study. We observe that for a given temperature, B_{sw} decreases with increasing thickness. This trend is linked to the Landau level index n (at the Fermi level) that participates in the interlayer transport. As discussed above, in this study, n has been found to decrease with increasing thickness. Thus for thicker samples smaller magnetic field will be needed to overcome Landau level mixing (and resulting positive MR) and trigger the negative MR. Lower n for thicker layers may result from the gradual decay in the charge density profile through the MLG stack from the doped (defective) interfacial layers.

We also note that for 200 nm and 300 nm thick samples, B_{sw} tends to decrease with increasing temperature, especially in the higher temperature range (>150K). We note that this feature is qualitatively different from what is expected in the quantum limit, in which case B_{sw} increases quadratically with temperature [38]. A possible reason for this anomaly could be the temperature dependence of the Fermi level, which is known to move at lower energy values as temperature is increased [144].

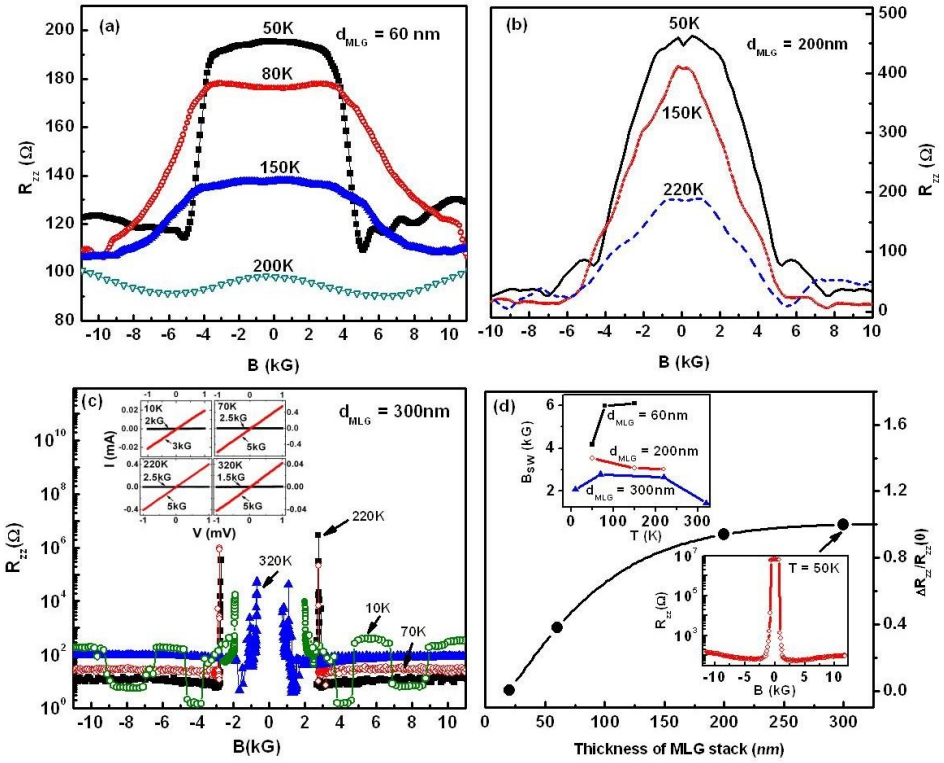

Figure 5.3 Interlayer magnetoresistance observed in weakly coupled MLG samples with various thicknesses. Data from (a) ~ 60 nm (S1), (b) ~ 200 nm (S2) and (c) ~ 300 nm (S3) thick samples are shown. At 50K (Figure 5.3(a)), CPP resistance sharply drops with increasing magnetic field above B_{SW} ~ 4kG and exhibits negative MR of ~ 40%. The negative MR effect becomes weaker as temperature is increased. For thicker MLG sample (Figure 5.3(b)), the negative MR is stronger, ~ 92% at 50K. For samples with even larger thickness (Figure 5.3(c)), $R_{ZZ}(0)$ often exceeds the upper limit (100 MΩ) of the measurement apparatus, behaving as a virtual open circuit. However as the perpendicular magnetic field is increased, resistance drops drastically by several orders of magnitude, resulting in a giant magnetoresistance that reaches theoretical maximum of ~ 100%. For all three set of samples, average of both scan directions is presented at each temperature and no hysteresis has been observed. Each resistance value is the average of 50 readings. A constant DC current of 1mA is applied to perform all MR measurements. The top inset in Figure 5.3(c) shows magnetic field dependent switching of the *I-V* characteristics at various temperatures for the 300 nm sample. (d) MR ratio ($\Delta R_{ZZ}/R_{ZZ}(0) = |R_{ZZ}(B) - R_{ZZ}(0)| / R_{ZZ}(0)$) as a function of MLG thickness of as-grown MLG on Ni samples at 50K. The magnetoresistance ratio increases with the thickness of MLG stack and almost reaches theoretical maximum (~1) for thickness larger than 300 nm. Bottom inset shows data from a 300 nm thick sample which exhibits measurable finite $R_{ZZ}(0)$ of ~10^7Ω. The MR data point corresponding to 300 nm thickness value in the main image is taken from this plot. The top inset shows B_{SW} vs T for the three batches.

The critical parameter is the Fermi temperature $T_F = E_F/k_B$, and Fermi level decreases drastically (by a factor of ~ 2) in the range $T/T_F \sim 0.35–0.9$ [144]. As the Fermi level decreases with increasing temperature, lower order Landau levels will participate in the interlayer charge transport at higher temperatures. For lower order Landau levels, smaller B will be needed to reduce the effect of inter Landau level mixing and trigger the negative MR. This will lead to a reduction in B_{sw} (for a given sample) as temperature is increased.

Reduction of the Fermi level with temperature is more pronounced at higher temperature [144], and this is presumably the reason why the reduction of B_{sw} with T is not significant in the low T regime and has not been observed at all for the 60 nm sample, in which case negative MR disappears at a much lower temperature. For example, in the case of 300 nm samples, from the oscillations at 10K we had estimated Landau level ~2 to be occupied at 0.4T (see previous discussions). This translates to $E_F \sim 32.4$ meV and $T_F \sim 374$K. Thus over the measurement range of 10K – 320K, T/T_F varies from 0.026 to 0.85, thus implying a large change (by factor of ~ 2) in the location of the Fermi level over the temperature range of 10–320K and a resulting significant decrease in B_{sw}. We note that at 320K, thermal broadening (estimated as k_BT) is ~ 27 meV and above-mentioned twofold drop in the Fermi level will push it below the thermally broadened range of its low-temperature value. After this twofold drop, the Fermi level will be located ~ 16.2 meV, and this energy range is primarily dominated by (thermally broadened) Landau levels 0 and 1 in the field range considered. Clearly, lower Landau levels are participating in transport at higher temperatures and smaller B_{sw} is expected.

Performing similar estimates for the other two batches, we find that T/T_F varies in the (narrower) range 0.09–0.43 for 200 nm samples and 0.08–0.33 for 60 nm samples. Thus, change in the Fermi level is less drastic in these batches (by a factor of ~ 1.2–1.4). Further, as discussed above, in these samples Fermi levels are located at higher energy values at low temperatures. Thus, resulting reduction in B_{sw} is relatively less compared to the 300 nm batch. We note that no theoretical model

exists at this point that addresses such scenarios and further theoretical studies are required to obtain a quantitative understanding of this effect.

5.4 Conclusion

In this chapter, we demonstrate ILMR effect in MLG stacks of various thicknesses. It has been found that the ILMR effect persists and becomes stronger as thickness is increased. Also, for larger thickness samples, magnitude of the MR effect is relatively insensitive to temperature. This is consistent with our prior observations (Figure 3.2, Chapter 3). This is in significant contrast with spintronic based MR devices such as GMR or spin valves. In these devices, thickness of the "active" spin transport layer needs to be smaller than typical "spin relaxation length" of the material that constitutes the active region [145], [146]. This imposes significant limitation on the device geometry and requires stringent control over the fabrication steps. Larger thickness of the "active" layer generally reduces the MR signal and smaller thickness leads to reliability issues such as formation of pinhole shorts between the electrodes. Also, for spintronic devices signal strength tends to decrease with increasing temperature. Due to these factors, ILMR effect in MLG appears to be a more robust MR mechanism for practical applications. Further, intrinsic compatibility of MLG with flexible electronics and sensorics makes ILMR an exciting platform for future magnetic sensing and data storage technologies.

In the next chapter, we will present a detailed study of magnetoresistance effects in Ni/MLG/Ni systems and its implications for spin filtering.

6 CPP MR STUDIES ON NI/MLG/NI SPIN VALVES[8]

So far in this thesis, we have thoroughly studied current perpendicular to plane (CPP) magnetoresistance (MR) effects in CVD grown MLG on Ni. We observed large magnetoresistance values that are consistent with interlayer magnetoresistance (ILMR) model. In these studies, by using non-magnetic silver (Ag) as top electrode, we intentionally muted any spin related effect. This is because Ag contact is non-magnetic and cannot distinguish between up and down spins. However, in principle, MLG/Ni systems are also capable of exhibiting large spin-related magnetoresistance effects due to perfect spin filtering at graphene/Ni interface as predicted in ref.s [33], [92]. This line of research is relatively underexplored to date, and in this chapter we report on experimental studies in this area and its implications for graphene spin filters. These studies have been performed by using MLG-based spin valve device configurations, as described later in this chapter. In this section, we will give an overview of spin filtering effect at graphene/Ni (Co) interface.

Spin filters are solid-state systems that preferentially transmit spins of one particular orientation. Spin filters are an essential component of all-electrical spintronic devices such as magnetic tunnel junctions (MTJs) [147], spin field-effect transistors (spin-FETs) [148] and many others [149] where they are employed as spin injectors and detectors. An ideal spin filter transmits only one particular spin orientation and blocks all other spin orientations. In recent years, possibility of ideal spin filtering has been explored by using nonconventional composite electrodes such as organic layers adsorbed on metallic surfaces [150]. It has been theoretically predicted that multilayer graphene (MLG) on (111) Ni or Co can potentially exhibit "perfect" spin filtering effect [33], [92]. According to this work, energy band alignment at nickel (or cobalt)-graphene interface promotes transmission of only

[8] Parts of this chapter have been published in a conference paper [100] and a detailed journal paper on this topic is under preparation.

minority spins and presence of multiple graphene layers (~3−4 or more) quenches majority spin conductance and leads to "perfect" spin filtering with almost 100% efficiency [33], [92].

In spintronics transition metal ferromagnets and half-metals are generally used as spin filters [147]. But transition metal ferromagnets typically have poor spin filtering efficiency (~ 50% or less) and half metals offer perfect spin filtering at zero K only and their efficiencies deteriorate significantly as temperature is increased [147]. Thus multilayer graphene (MLG) as grown on Ni (or Co) appears to be a promising candidate for realizing efficient spin filters. In addition, multilayer graphene (MLG) grown on catalytic Ni substrate using chemical vapor deposition (CVD) exhibits intriguing charge and magnetotransport properties that are very similar to a single layer graphene due to existence of weak interlayer coupling [28], [37]. As demonstrated in previous chapters, the out-of-plane charge transport in this system mainly occurs via interlayer tunneling between consecutive graphene layers. Such weakly coupled multilayer graphene is especially interesting for out-of-plane spin transport, as the spin-flip mechanisms are mostly suppressed in the tunneling process [151].

However, there are still many challenges in this area. For example, as discussed in the previous chapters, there exists a strong overlap between out-of-plane 3*d* states of nickel (and cobalt) and $2p_z$ states of interfacial carbon atoms [85] and such hybridization results in destruction of linear energy dispersion of interfacial graphene layers, elimination of Dirac point, creation of a band gap and new electronic "defect" states in the band gap. These effects were not considered in the spin filtering models [33], [92]. Formation of such "chemisorption interfaces" can potentially quench spin-filtering effect at graphene/Ni (Co) interface by introducing additional spin flip processes. These effects should be eliminated in order to maximize spin filtering effect at MLG/Ni (Co) interface. In this chapter, we report our studies on CPP magnetoresistance effects in as-grown MLG/Ni system with

two different device structures, (1) Ni/MLG/Ni and (2) Ni/Al_2O_3/MLG/Ni. In the next section, fabrication and characterization of these devices are presented.

6.1 Fabrication and Characterization

As mentioned above, in our previous studies, in order to mute any spin filtering effect we considered Ni/MLG/Ag trilayered structure, in which MLG is CVD grown on Ni (Co). Since the top electrode (Ag) is non-magnetic, no spin-dependent effect is expected in the MR data. However in the present study, we have prepared two sets of devices with as-grown MLG samples, (1) Ni/MLG/Ni and (2) Ni/Al_2O_3/MLG/Ni in which both contacts are ferromagnetic and clearly these samples have a spin valve structure. First, multilayer graphene (MLG) of thickness ~ 200 nm is synthesized in CVD process using nickel foil (25μm thick, $2cm \times 2cm$) as a catalytic substrate. The details of this CVD process and characterization steps of as-grown MLG stacks have been presented previously in sections 2.1.1 and 2.2.1 (Chapter 2). From our previous studies, we understand that the as-grown MLG on Ni consists of weakly coupled graphene layers and the out-of-plane charge transport mainly occurs by interlayer tunneling between consecutive graphene layers. As explained above, the spin filtering effect that is expected in graphene/Ni interface can be suppressed due to strong interfacial hybridization between 3*d* orbitals of Ni and $2p_z$ orbitals of carbon [85]. In addition, as explained in section 4.2 (Chapter 4), few layers at the hybridized graphene/Ni interface are discontinuous and therefore they are defective as well. However, we demonstrated that the graphene layers away from this interface are free from any structural defects [96]. Therefore, no further spin flip is expected from these defect-free layers.

To prepare device-1 (Ni/MLG/Ni), ~ 80 nm Ni thinfilm is e-beam evaporated ($0.5\ Å/sec$, beam voltage of 7.5kV) on Ni-grown MLG using a mechanical mask with an opening of $1mm^2$. Figure 6.1(a) shows the schematic of device-1. Raman spectroscopy has been used to verify the quality of the MLG stack. We used Raman spectroscopy with a laser wavelength of 532 nm with 100% beam power. Raman spectra of as-grown MLG on Ni show strong *G* peak and symmetric *2D* band (black

line in Figure 6.1(b)) which are typical Raman signatures of a weakly coupled MLG [28], [96]. The intensity of defect peak at 1350 cm^{-1} is extremely weak, implies negligible density of defects. Whereas, after e-beam evaporation of ~ 80 nm Ni thinfilm, a strong *D*-peak appeared in the Raman spectra (top red line in Figure 6.1(b)) in the vicinity of Ni deposited area. Except the appearance of strong *D* peak, the shape and positions of *G* and *2D* peaks are mostly identical to as-grown MLG on Ni. In Figure 6.1(b) *inset*, X-ray diffraction (XRD) spectra of bottom Ni foil and top e-beam evaporated Ni thinfilm are displayed. Both XRD spectra are identical and mainly dominated by Ni(111) grains with a very low population of Ni (100) grains. This is consistent with our previous observation in Figure 2.1 (Chapter 2). Therefore not much structural differences are present between bottom Ni foil and top Ni thinfilm.

For device-2, a thin alumina (Al_2O_3) capping layer of ~ 10 nm is e-beam evaporated ($0.5Å/sec$, 6.5kV) prior to Ni thinfilm deposition. The schematic of device-2 ($Ni/Al_2O_3/MLG/Ni$) is displayed in Figure 6.1(c). Top Ni electrode is deposited under the same conditions ($0.5Å/sec$, 7.5kV) as in device-1. Figure 6.1(d) shows the Raman spectra of as-grown MLG on Ni after alumina deposition (bottom black line) followed by Ni deposition (top red line). Unlike device-1, no defect peak or any change in position and width of Raman peaks are observed (Figure 6.1(d)). In the next section, CPP MR measurements from both devices are presented.

6.2 CPP MR Measurements

Figure 6.2(a) shows normalized CPP resistance[9] (*r*) vs. out-of-plane magnetic field (*B*) of device-1 in the temperature range 10 – 250K. CPP MR[10] of the device at 10K exhibit negative MR effects at both low field regime (0 – 3k*G*) as well as at high field regime (4 – 8 kG). At 10K, the low field negative MR is ~ 4% whereas slightly higher (~ 12%) negative MR is observed in the high-field regime. Both of these negative MR values gradually decrease with increase in temperature.

[9] $r = {R_{zz}(B)}/{R_{zz}(B = 0)}$

[10] $MR = {[R_{zz}(B) - R_{zz}(B = 0)]}/{R_{zz}(B)}$

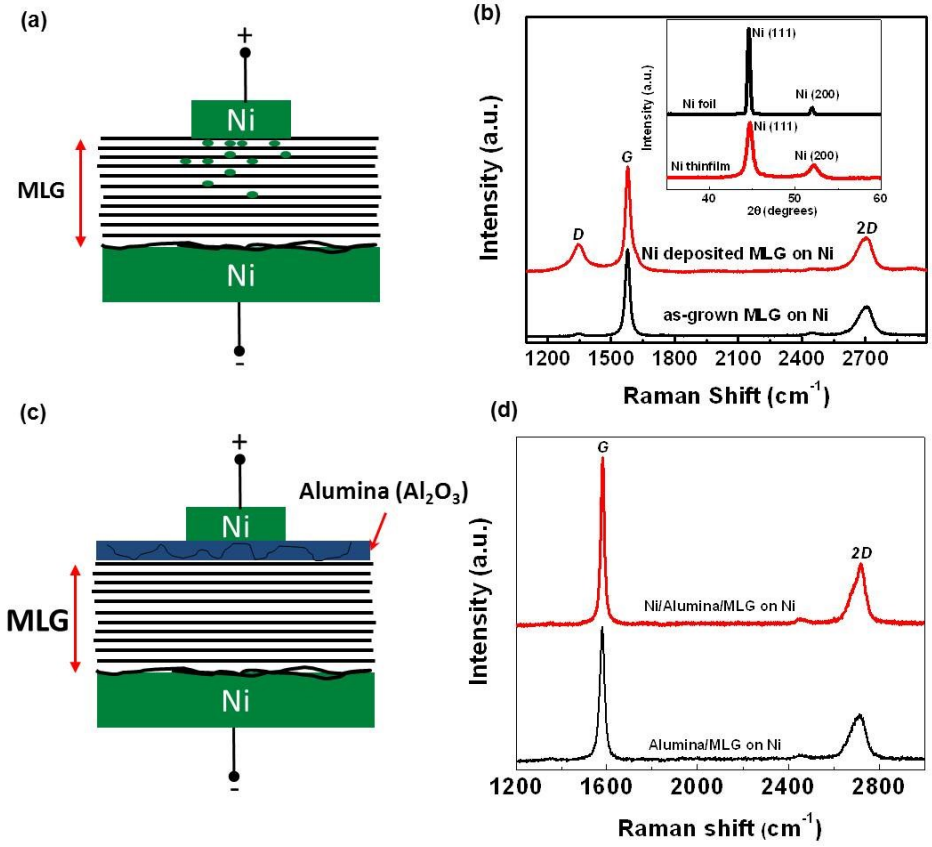

Figure 6.1 (a) Device schematic of e-beam evaporated Ni thinfilm (~ 80 nm) on as-grown MLG (~ 200 nm) on Ni. The deposited Ni particles penetrate in to MLG stack and modify the band structure of graphene layers. These penetrated Ni particles reduce the effective thickness of the weakly coupled MLG stack. (b) Raman spectra of before (bottom black line) and after (top red line) Ni thinfilm deposition on as-grown MLG. The as-grown MLG shows almost negligible defect peak (*D*-peak). Defects induced by Ni deposition are manifested as a strong defect peak (*D*-peak) at 1350 cm^{-1} in the Raman spectra (top red line). Except strong *D*-peak, shape and positions of *G* and 2*D* bands are almost identical to the pre-deposition sample. Figure 1(b) inset shows XRD of bottom Ni foil (top black line) and Ni thinfilm (bottom red line). The XRD features are identical and are mainly dominated by Ni(111) grains with very low population of Ni(100) grains. (c) Device geometry of Ni/Al_2O_3/MLG/Ni structure. Polycrystalline Alumina (Al_2O_3) is deposited using e-beam evaporation (0.5Å/sec, 6.5kV) followed by Ni thinfilm deposition (0.5Å/sec, 7.5kV) on as-grown MLG on Ni. (d) Raman spectrum of as-grown MLG on Ni is unchanged even after alumina (Al_2O_3) deposition (bottom black line). No defect peak at 1350cm^{-1} is observed even after e-beam evaporation of Ni on alumina coated MLG surface (top red line).

Above 150K, positive MR of ~ 7% (4 – 8kG) is observed. In addition, noise-like fluctuations are observed in the low-field negative MR data at 10K and 20K (*inset* Figure 6.2(a)) which disappeared at higher temperatures. Figure 6.2 (b) shows CPP resistance (R_{zz}) in the temperature range 10 – 250K of device-1 measured at three different field values (0kG, 5kG and 10kG). $R_{zz}(T)$ shows insulator-like temperature dependence at all field values up to 150K, up to which both negative MR effects are prominent. Figure 6.2(b) *inset* displays inverse normalized CPP resistance (r^{-1}) as a function of out-of-plane magnetic field (B) in the high-field range ($4 - 8kG$). Clear linear fits are observed and the slopes of $r^{-1}(B)$ curves decrease with increase in temperature, which are consistent with the ILMR model [38]. The low-field MR feature most likely originates from weak localization effect.

Figure 6.2(c) displays $r(B)$ of device-2 for 15 – 125K. We observe large negative MR of ~ 10^3 % in the field range $0 - 3kG$. At low temperatures, for field values higher than ~ 3kG, a sharp positive MR is observed that persists upto 70K (Figure 6.2(c)). Figure 6.2(c) *inset* shows clear linear fitting for lnR_{zz} *vs.* $1/kT$ at a fixed out of plane magnetic field (6kG) where R_{zz} shows plateau-like field dependence. Figure 6.2(d) plots inverse normalized CPP resistance (r^{-1}) in the field range, $0 - 3kG$. Clear linear fittings are observed and the slope of $r^{-1}(B)$ decreases with increase in temperature which is consistent with the ILMR model [38]. Thus, the low field MR feature is due to ILMR effect. In the next section, we will discuss possible explanation for the observed MR data.

6.3 Discussion and Conclusion

From the Raman spectra (Figure 6.1(b)) of device-1, it is clear that defects have been introduced in the MLG stack during e-beam evaporation of Ni thinfilm. The low field negative MR observed in this sample is significantly different from the Ag/MLG/Ni structures studied previously (Figure 3.2, Chapter 3). These differences in MR response are clearly due to top Ni thinfilm deposition. E-beam evaporation at room temperature cannot completely intercalate all deposited Ni atoms in thick MLG stack (~ 200 nm) [152], [153]. Intercalation of a monolayers of Ni atoms require large temperatures (> 650℃) and therefore not possible in the

present case [153]. The value of I_D/I_G ~ 0.3 from Raman spectra also implies low density of defects in Ni deposited area of MLG stack [154]. Therefore, we can only expect few deposited Ni atoms penetrated into MLG stack. These penetrated Ni atoms experience strong hybridization with $2p_z$ orbitals of graphene layers and locally modify the band structure of graphene [152], [155]. In addition, Ni deposition can also damage *C*-*C* bonds in graphene structure which can also contribute to the observed *D* peak in the Raman spectra. Both hybridized and damaged graphene layers result defect peak (*D* peak) in the Raman spectra and this observation is consistent with previous studies in defect-induced graphene layers fabricated by different methods [156]–[159].

The defective graphene layers and intercalated Ni atoms act like strong scattering centres during out-of-plane charge transport in device-1. In CPP geometry, some of the charge carriers experience scattering at defects and Ni atoms. The interference of these scattered paths localize charge carriers due to increase in back scattering probability [157]. Application of an out-of-plane magnetic field minimizes this back scattering probability and gradually decreases the resistance of the system. This effect explains negative MR at low field range and is known as weak localization effect [5].

The existence of universal conductance fluctuations (UCF) at low temperatures (10K and 20K in Figure 6.2 (a) *inset*) is an additional proof that the observed negative MR indeed originates from weak localization effect. Qualitatively similar magnetoresistance responses have been observed in other strongly localized graphene systems such as, hydrogenated [156], ozone-damaged [160], fluorinated [157] and metal-decorated [159] graphene. At higher field values, weak localization effect is not effective and ILMR is more dominant due to well-separated Landau levels. Therefore, clear negative MR due to ILMR effect is observed at high-field range (Figure 6.2(b)). However, the magnitude of negative MR due to ILMR is comparatively smaller than that observed in Ag/MLG/Ni samples. This is expected as the penetrated Ni atoms minimizes the effective thickness of weakly coupled

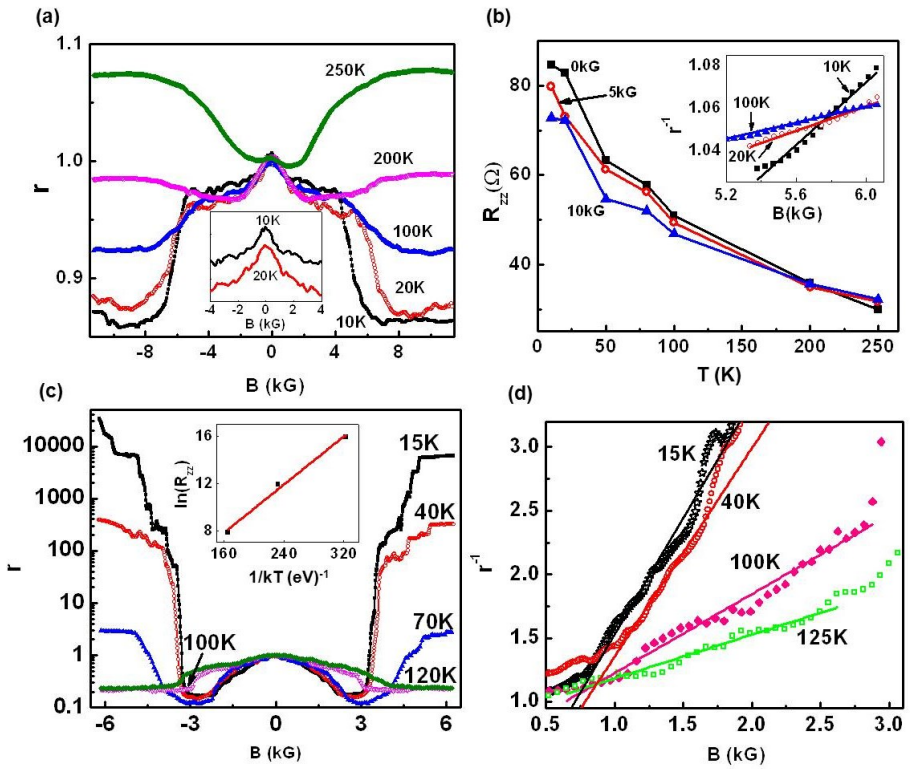

Figure 6.2 (a) Normalized CPP MR ($r = R_{zz}(B)/R_{zz}(0)$) of Ni/MLG/Ni for 10 – 250K. MR response is symmetric with field direction and no hysteresis has been observed. At 10K, low-field negative MR of ~ 4% and universal conductance fluctuations (UCF) are observed in the field range 0 – 3kG and a high-field negative MR of ~ 12% is observed between 4 – 8kG. These effects get weaker with increase in temperature and a positive MR of ~ 7% is detected above 150K in the field range 4 – 8kG. (b) R_{zz}(T) at three different field values (0kG, 5kG and 10kG) for 10 – 250*K*. R_{zz} *(T)* shows insulator-like temperature dependence upto 200*K*. *Inset* shows the inverse normalized CPP resistance (r^{-1}) as a function of out-of-plane magnetic field (*B*) in the field range 4 – 8kG. The slope of $r^{-1}(B)$ curves clearly decreases with increase in temperature and this is consistent with the interlayer magnetoresistance (ILMR) model. Constant DC current bias of 1mA is used for all MR measurements. (c) Normalized CPP MR of Ni/Al_2O_3/MLG/Ni structure for 15 – 125K. A large negative MR of ~ 10^3% is observed in the low-field range (< 3kG). Above 3kG, a strong and sharp positive MR (~10^9%) is observed upto 70K. This strong positive MR gradually decreases with increase in temperature and is completely suppressed above 70K. MR response is symmetric with field direction and no hysteresis has been observed. Figure 6.2(c) *inset* displays a linear fitting for lnR_{zz} *vs. 1/kT* at a fixed field (6kG) where R_{zz} becomes constant and shows plateau-like field dependence. (d) Inverse normalized CPP MR (r^{-1}) is fitted with a straight line in the low-field range at different temperatures. The decrease in slope of $r^{-1}(B)$ curve with increasing temperature clearly suggests that the low-field negative MR is due to interlayer magnetoresistance (ILMR) effect. Constant DC current bias of 1mA is used for all MR measurements.

MLG stack and thinner MLG stack exhibits weaker ILMR as demonstrated in Chapter 4 (Figure 4.4 (b)).

In device-2, to avoid penetration of e-beam evaporated Ni atoms in the MLG stack, we first covered the entire MLG surface with alumina layer prior to Ni deposition. Alumina (Al_2O_3) film deposition using e-beam evaporation generally forms a polycrystalline film and is not free from pin-holes even at thicknesses close to 10nm. The absence of defect peak (*D* peak) in the Raman spectra implies that the alumina deposition does not introduce any defects in the MLG stack. The lower deposition voltage (6.5kV) and larger particle size of alumina might be the reason for defect-free deposition of alumina on the MLG stack. Here, the alumina layer acts like a protective capping layer over the MLG surface and therefore no Raman defect peak has been observed even after Ni thinfilm deposition (Figure 6.1(d)).

CPP MR of the Ni/Al_2O_3/MLG/Ni structure (device-2) clearly displays large negative ILMR at low field range (Figure 6.2(c)). Similar CPP MR response has been observed previously (Figure 3.2, Chapter 3) in as-grown MLG samples with similar thickness (~ 200 nm) and is consistent with the interlayer magnetoresistance (ILMR) model [38]. At high field (> 3kG), sharp positive MR with plateau-like structures are observed that gradually weakens with increase in temperature. The origin of this sharp positive MR effect is related to the location of the Fermi level with respect to the zero mode Landau level (or the Dirac point). If the Fermi level is located above the Dirac point, in presence of out-of-plane magnetic field, the interlayer tunneling occurs between higher order Landau levels ($n \rightarrow n \; and \; n \neq 0$). As discussed in section 4.2 (Chapter 4) and based on ref.[61], interlayer tunneling between same orders of Landau levels ($n \rightarrow n$) exhibits negative interlayer magnetoresistance (ILMR). However, the Landau level separation (ΔE^{11}) [40] increases with increase in magnetic field strength and therefore, the gap between Fermi level (E_F) and E_n get separated as B is varied. For a certain value of B, E_F will lie between two consecutive Landau levels and at this point, since there

[11] $\Delta E = 36.25 \left(\sqrt{nB} - \sqrt{(n-1)B}\right) meV$

are no states available near the Fermi level, the interlayer current is completely suppressed and sharp positive MR with plateau-like field dependence is observed (Figure 6.2(c)). This effect gradually weakens with increase in temperature as the Landau level broadening increases with temperature. To verify this, we have plotted $ln(R_{zz})$ vs. $1/kT$ which show clear linear trend in low temperature range implying thermally activated transport. The value of energy gap (E_F-E_n) as estimated from the slope of this linear fit is ~ 50meV. This value is within the theoretical limit of Landau level separation between $n = 0$ (zero-mode) and $n = 1$ Landau levels in graphene at 6kG [40]. Therefore, the sharp positive MR observed in device-2 is due to field-induced increase in Landau level separation.

In conclusion, to realize theoretically predicted spin filtering effect in Ni/MLG/Ni systems, ideal graphene/Ni interfaces are required that are difficult to achieve with CVD grown MLG on Ni and e-beam evaporated Ni. These devices only show weak localization and/or ILMR but no spin filtering. However, combination of low field and high field magnetoresistance effects observed in this study offer new possibilities to create tailored magnetoresistance responses in as-grown MLG stacks. In addition, we also observed sharp positive MR effect in case of Ni/Al_2O_3/MLG/Ni sample along with ILMR effect in as-grown MLG stack that has never been reported before in graphitic systems at comparable field and temperature range. Future work in this research direction will be presented in the next chapter.

7 RECOMMENDATIONS FOR THE FUTURE

Based on our previous results, we are planning to explore the following subprojects in the future: (1) CPP-MR effects in as-grown MLG on cobalt, (2) MR effects in functionalized graphene/Ni(111) and exploring spin filtering effect in this system, and (3) MR effects in MLG transferred on flexible substrates. The first subproject aims to study the CPP-MR effects in as-grown MLG on Co, which in principle is very similar to the MLG on Ni system. Thus, strong CPP-MR effects can be expected in as-grown MLG on Co samples as well. In the second subproject, we are planning to reduce the degree of hybridization at graphene/Ni interface by functionalizing with potassium (K) ions [101]. Then a detailed MR study will be performed on the functionalized MLG/Ni system. The CPP-MR effect may be tunable by such functionalization process. This technique will also allow us to study spin filtering effect in graphene based magnetic tunnel junctions (MTJs) [92]. In the final subproject, we are planning to study MR effects in MLG transferred on flexible substrates. Further details on these proposed subprojects are provided below.

7.1 Subproject 1: CPP-MR Effects in As-Grown MLG on Cobalt

As discussed before, we have observed large CPP-MR effects in MLG CVD-grown on Ni and these effects persist even at room temperature (Figure 3.2, Chapter 3). To explore if such features are common in MLGs, CVD-grown on other ferromagnetic substrates, we plan to explore CPP-MR effects on MLG as grown on cobalt substrate. MLG can be grown on Co (0001) substrate under similar CVD conditions as MLG on Ni (Chapter 2, Section 2.1.1). The lattice mismatch of graphene/Co (0001) interface is very low (1.8%), which is very close to the lattice mismatch between graphene and Ni (1.3%) [155]. This feature may allow continuous growth of large area MLG over the entire Co surface during the CVD process. Next, similar device fabrication and measurement steps will be followed

for MLG on Co samples. We have performed some preliminary experiments and initial results are presented here.

7.1.1 Preliminary Results

We have synthesized MLG on polycrystalline Co substrate using similar CVD process parameters as our MLG on Ni samples (section 2.1.1, Chapter 2). Similar device fabrication and measurement steps have been repeated for MLG on Co samples. Raman spectra of MLG grown on Co are shown in Figure 7.1 (a). In some regions of MLG, we have observed symmetric 2*D* Raman peak that indicates weak interlayer coupling. In other regions, Raman 2D peak shows "shoulder" in lower frequency side that implies strong interlayer coupling. CPP MR measurements performed over weakly coupled MLG are displayed in Figure 7.1 (b). These preliminary CPP MR measurements also indicate presence of negative MR effect, which most likely originates due to ILMR. Next, we are planning to improve the quality of MLG on Co and then systematically study ILMR effect as a function of temperature, field direction and the thickness of MLG. Proposed fabrication methodology for these experiments are given below.

7.1.2 Proposed Methodology

To perform above-mentioned studies, different thicknesses of as-grown MLG on Co samples are required. Growth of high quality monolayer to multilayer graphene (MLG) have been reported previously in polycrystalline thin films of Co [161], [162]. Single crystal Co film on sapphire substrate showed monolayer growth [162]. Metal-catalyzed (Co or Ni thin films of 100 – 300 nm) crystallization of amorphous carbon (a-C) have also shown growth of graphene layers depending on the film thickness [163]. Similar to our previous studies in MLG on Ni, MLG stacks with different thicknesses can be achieved by controlling carbon species concentration in CVD process. These techniques will be explored for the proposed studies.

7.2 Subproject 2: MR in Functionalized MLG/Ni Interface and Studies on Spin Filtering

Strong hybridization at the graphene/Ni interface modifies electronic structure of CVD-grown graphene at the interface [32], [155]. The hybridized interface is characterized by (1) large overlap of $2p_z$ orbitals of graphene and $3d$ orbitals of Ni, and (2) smaller graphene-Ni inter-plane distance compared to graphene-graphene interlayer distance [164], [165]. Such interfacial hybridization is presumably the reason for non-observation of predicted high degree of spin filtering. It has been shown that the degree of hybridization at graphene/Ni interface can be controlled or tuned by intercalating alkali metals (e.g. Na, K, etc.), also known as "ionic functionalization of graphene" [101]. It has been observed that potassium (K) atoms deposited on graphene surface penetrate into graphene/Ni interface and re-establish the pristine graphene band structure [97], [140], [141]. The goal of this subproject is to explore effect of such functionalization on the ILMR effect and the spin filtering effect. The intercalated potassium atoms minimize overlap between $2p_z$ orbitals of graphene and $3d$ orbitals of Ni and weaken the effect of hybridization at graphene/Ni interface [164], [165]. Such modified graphene/Ni interface will be used to realize graphene based MTJs and to explore spin filtering.

7.2.1 Proposed Methodology

First, we plan to grow thinner MLG on Ni catalyst using the CVD process described in section 2.1. After that, potassium will be evaporated on MLG under ultra-high vacuum (UHV) conditions to avoid any possible oxidation of potassium atoms [166]. The deposited potassium atoms penetrate into MLG and reach graphene/Ni interface [164], [165]. Finally, potassium intercalated MLG/Ni samples will be prepared for MR measurements as described in Chapter 2 (section 2.1.1). Magnetoresistance (MR) of these samples can potentially give clearer idea on MR effects observed in as-grown MLG on Ni (Figure 3.2) and may also help to realize theoretically predicted spin filtering effect in Ni/MLG/Ni structure [92]. Typical sample fabrication includes a sequence of the following steps: (a) CVD growth of MLG on Ni(111) surface [28], [30], [65] (after removal of native surface oxide,

which can potentially quench surface spin polarization of nickel [167]), (b) functionalization of MLG/Ni interface, (c) growth of (amorphous) alumina tunnel barrier (~1 nm) on MLG using atomic layer deposition (ALD), and (c) deposition of (polycrystalline) nickel contact on top of the tunnel barrier using e-beam evaporation.

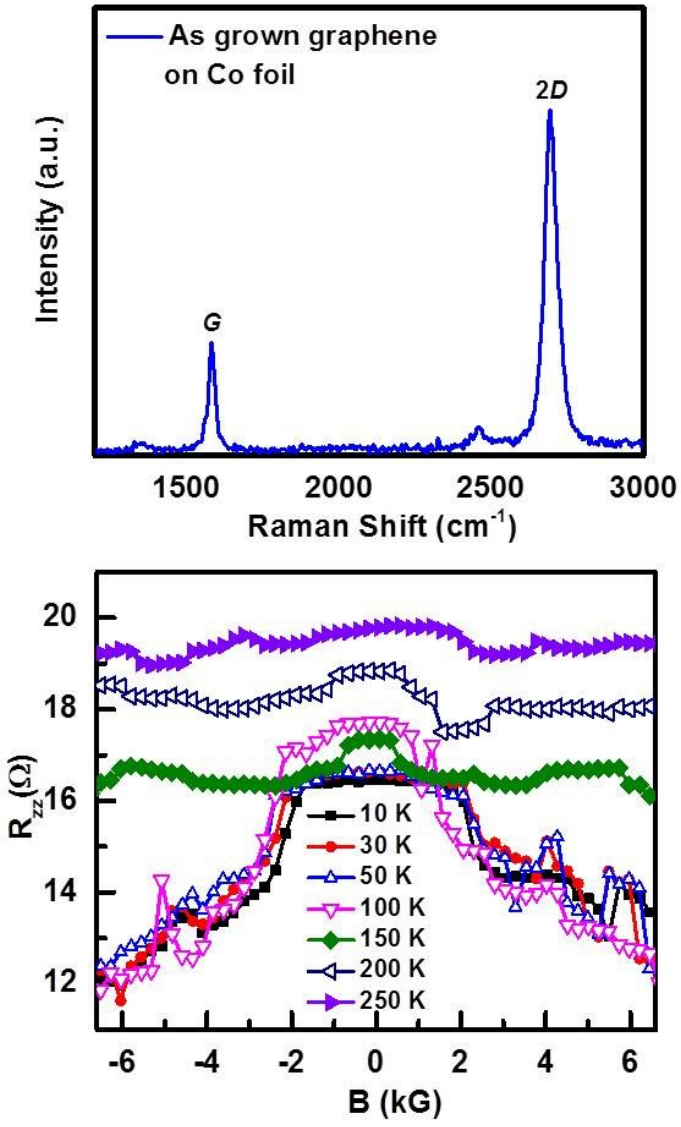

Figure 7.1 Raman Spectrum and CPP MR Characteristics of MLG Samples As Grown on Co. In this sample MLG thickness is ~ 30 nm. Raman 2*D* peak is symmetric and does not show any HOPG-like shoulder peak (top image). No defect (*D*) peak has been observed in this case. Negative CPP MR has been observed in these samples for certain temperatures (bottom image).

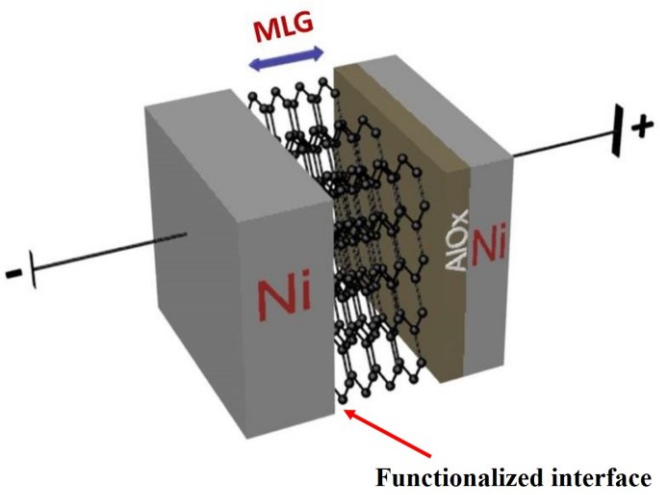

Figure 7.2 Schematic description of the graphene-based MTJ, which can potentially show spin filtering. The MLG is grown on the left Ni contact by CVD.

According to previous theoretical studies, transmitted spin polarization through four monolayers of graphene is within a percent of 100% and for higher number of graphene layers, spin polarization is virtually complete [33], [92]. As a result, large change in device resistance is expected as the nickel contacts are switched between mutually parallel to mutually antiparallel configurations. At this point we also note two other inherent advantages of this sample geometry. First, graphene passivates nickel surface against oxygen exposure and preserves surface spin polarization [167], which is desirable for MTJs. Second, the presence of the tunnel barrier protects underlying graphene from any structural damage during deposition of the top metal contact. This lowers the probability of any defect-induced spin-flip process as the carriers traverse through the junction.

7.3 Subproject 3: MR effects in MLG Transferred on Flexible Substrates

Commercialization of flexible electronics is rapidly expanding into many areas of electronics such as displays, solar cells and sensors [168], [169]. Such increasing growth of commercial market for flexible electronics has created an increasing need to develop flexible logic and memory devices that can be seamlessly integrated with the existing flexible technologies. However not much progress has taken place in

this line of research. Graphene based flexible magnetic sensors have strong potential to fill this gap and open new possibilities to realize flexible magnetic random access memory (MRAM) circuits. In this subproject, we are planning to study MR effects in MLG transferred on flexible substrates. This study will provide an understanding on allowable bending radius range, influence of substrate induced strain on MR and the quality of MLG required to realize flexible graphene based magnetic sensors. Below, we provide our preliminary results and proposed methodology for this subproject.

7.3.1 Preliminary Results

We performed some preliminary measurements in this direction using few layer graphene (~ 8L) grown on Cu and graphene transfer tape as flexible substrate. As shown before in Figure 3.10 (Chapter 3), 8-layer as-grown graphene on Cu show negative in-plane MR due to weak localization (WL) effect. In this study, we investigate how this negative MR will be affected by the strain introduced by the flexible substrate. We systematically introduced strain in transferred graphene layers by bending the flexible substrate (graphene transfer tape) and performed in-plane MR measurements. Preliminary results of this study are shown in Figure 7.3. A clear difference in in-plane MR response is observed between 0% strained (Figure 7.3(a)) and 16% strained (Figure 7.3 (b)) transferred MLG on flexible substrate. The value of the strain in graphene layers is estimated by using the bending radius of the substrate as described in ref. [170]. The magnitude of the negative MR observed in MLG on strained substrate (16% strain) is almost identical to that observed on the flat substrate (0% strain). However, in case of strained substrate, the negative MR is superimposed by a strong background noise (Figure 7.3(b)).

7.3.2 Proposed Methodology

Both CIP and CPP MR effects will be studied on various types of MLG samples transferred on flexible substrates. Various types of flexible substrates, such as PMMA, polydimethylsiloxane (PDMS) and polyimide will be tested in this study.

Sample fabrication for this study involves following steps. (a) CVD growth of MLG on Cu and Ni, (b) Transferring as-grown MLG on flexible substrates, (c) Top metal electrode deposition using a mechanical mask. These steps have already been described in detail in the previous chapters.

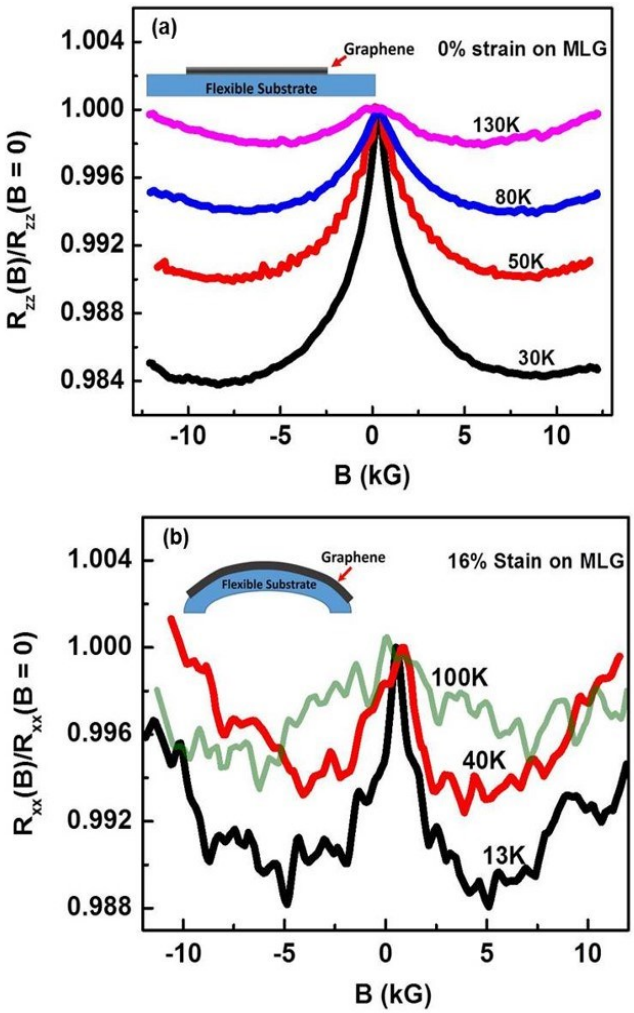

Figure 7.3 Magnetoresistance (MR) Study of Transferred MLG (~ 8L) on Flexible Substrates. (a) In-plane MR in transferred MLG on flexible substrate (Graphene thermal tape) with no strain introduced by substrate bending as shown in top left *inset*. Negative MR of ~1.6% is observed up to 130K. This is consistent with weak localization (WL) effect and also similar to WL effect observed in as-grown MLG (8L) displayed in Figure 3.10 (Chapter 3). (b) In-plane MR in transferred MLG with ~ 6.1mm bending radius as displayed in top left *inset*. According to ref.[170], strain introduced on graphene layers at this bending radius is ~ 16% and a negative MR of ~ 1.2% is observed at 13K.

References

[1] N. W. Ashcroft and N. D. Mermin, *Solid state physics*. Fort Worth: Harcourt college publishers, 1976.

[2] C. Chappert, A. Fert, and F. N. Van Dau, "The emergence of spin electronics in data storage," *Nat. Mater.*, vol. 6, no. 11, pp. 813–823, Nov. 2007.

[3] J. Nickel, "Magnetoresistance Overview," *Hewlett-Packard Lab. Tech. Publ. Dep. 1995*.

[4] T. R. McGuire and R. I. Potter, "Anisotropic magnetoresistance in ferromagnetic 3d alloys," *IEEE Trans. Magn.*, vol. 11, no. 4, pp. 1018–1038, 1975.

[5] G. Bergmann, "Weak Localization in Thin Films," *Phys. Scr.*, vol. 1986, no. T14, p. 99, Jan. 1986.

[6] A. P. Ramirez, "Colossal magnetoresistance," *J. Phys. Condens. Matter*, vol. 9, no. 39, p. 8171, Sep. 1997.

[7] T. L. Francis, Ö. Mermer, G. Veeraraghavan, and M. Wohlgenannt, "Large magnetoresistance at room temperature in semiconducting polymer sandwich devices," *New J. Phys.*, vol. 6, no. 1, p. 185, Nov. 2004.

[8] Z.-M. Liao, H.-C. Wu, S. Kumar, G. S. Duesberg, Y.-B. Zhou, G. L. W. Cross, I. V. Shvets, and D.-P. Yu, "Large Magnetoresistance in Few Layer Graphene Stacks with Current Perpendicular to Plane Geometry," *Adv. Mater.*, vol. 24, no. 14, pp. 1862–1866, 2012.

[9] H. Kempa, P. Esquinazi, and Y. Kopelevich, "Field-induced metal-insulator transition in the c-axis resistivity of graphite," *Phys Rev B*, vol. 65, no. 24, p. 241101, May 2002.

[10] Y. Liu, W. S. Lew, and L. Sun, "Enhanced weak localization effect in few-layer graphene," *Phys Chem Chem Phys*, vol. 13, no. 45, pp. 20208–20214, Nov. 2011.

[11] Y. Kopelevich, R. R. da Silva, J. C. M. Pantoja, and A. M. Bratkovsky, "Negative c-axis magnetoresistance in graphite," vol. 374, no. 45, pp. 4629–4632, Oct. 2010.

[12] X. Wu, X. Li, Z. Song, C. Berger, and W. A. de Heer, "Weak Antilocalization in Epitaxial Graphene: Evidence for Chiral Electrons," *Phys Rev Lett*, vol. 98, no. 13, p. 136801, Mar. 2007.

[13] F. V. Tikhonenko, A. A. Kozikov, A. K. Savchenko, and R. V. Gorbachev, "Transition between Electron Localization and Antilocalization in Graphene," *Phys Rev Lett*, vol. 103, no. 22, p. 226801, Nov. 2009.

[14] H. Kempa, P. Esquinazi, and Y. Kopelevich, "Integer quantum Hall effect in graphite," *Solid State Commun.*, vol. 138, no. 3, pp. 118–122, Apr. 2006.

[15] K. S. Novoselov, A. K. Geim, S. V. Morozov, D. Jiang, M. I. Katsnelson, I. V. Grigorieva, S. V. Dubonos, and A. A. Firsov, "Two-dimensional gas of massless Dirac fermions in graphene," *Nature*, vol. 438, no. 7065, pp. 197–200, Nov. 2005.

[16] K. S. Novoselov, A. K. Geim, S. V. Morozov, D. Jiang, Y. Zhang, S. V. Dubonos, I. V. Grigorieva, and A. A. Firsov, "Electric Field Effect in Atomically Thin Carbon Films," *Science*, vol. 306, no. 5696, pp. 666–669, Oct. 2004.
[17] Y. Hernandez, V. Nicolosi, M. Lotya, F. M. Blighe, Z. Sun, S. De, I. T. McGovern, B. Holland, M. Byrne, Y. K. Gun'Ko, J. J. Boland, P. Niraj, G. Duesberg, S. Krishnamurthy, R. Goodhue, J. Hutchison, V. Scardaci, A. C. Ferrari, and J. N. Coleman, "High-yield production of graphene by liquid-phase exfoliation of graphite," *Nat. Nanotechnol.*, vol. 3, no. 9, pp. 563–568, Sep. 2008.
[18] W. A. de Heer, C. Berger, X. Wu, P. N. First, E. H. Conrad, X. Li, T. Li, M. Sprinkle, J. Hass, M. L. Sadowski, M. Potemski, and G. Martinez, "Epitaxial graphene," *Solid State Commun.*, vol. 143, no. 1–2, pp. 92–100, Jul. 2007.
[19] J. Hass, R. Feng, J. E. Millán-Otoya, X. Li, M. Sprinkle, P. N. First, W. A. de Heer, E. H. Conrad, and C. Berger, "Structural properties of the multilayer graphene/4H-SiC(0001) system as determined by surface x-ray diffraction," *Phys. Rev. B*, vol. 75, no. 21, p. 214109, Jun. 2007.
[20] L. B. Biedermann, M. L. Bolen, M. A. Capano, D. Zemlyanov, and R. G. Reifenberger, "Insights into few-layer epitaxial graphene growth on 4H-SiC(0001) substrates from STM studies," *Phys. Rev. B*, vol. 79, no. 12, p. 125411, Mar. 2009.
[21] F. Mittendorfer, A. Garhofer, J. Redinger, J. Klimes, J. Harl, and G. Kresse, "Graphene on Ni(111): Strong interaction and weak adsorption," *Phys. Rev. B*, vol. 84, no. 20, Nov. 2011.
[22] P. Sutter, J. T. Sadowski, and E. Sutter, "Graphene on Pt(111): Growth and substrate interaction," *Phys. Rev. B*, vol. 80, no. 24, p. 245411, Dec. 2009.
[23] E. N. Voloshina, Y. S. Dedkov, S. Torbruegge, A. Thissen, and M. Fonin, "Graphene on Rh(111): Scanning tunneling and atomic force microscopies studies," *Appl. Phys. Lett.*, vol. 100, no. 24, Jun. 2012.
[24] Z.-Y. Juang, C.-Y. Wu, A.-Y. Lu, C.-Y. Su, K.-C. Leou, F.-R. Chen, and C.-H. Tsai, "Graphene synthesis by chemical vapor deposition and transfer by a roll-to-roll process," *Carbon*, vol. 48, no. 11, pp. 3169–3174, Sep. 2010.
[25] P. W. Sutter, P. M. Albrecht, and E. A. Sutter, "Graphene growth on epitaxial Ru thin films on sapphire," *Appl. Phys. Lett.*, vol. 97, no. 21, Nov. 2010.
[26] K. Yan, H. Peng, Y. Zhou, H. Li, and Z. Liu, "Formation of Bilayer Bernal Graphene: Layer-by-Layer Epitaxy via Chemical Vapor Deposition," *Nano Lett.*, vol. 11, no. 3, pp. 1106–1110, Mar. 2011.
[27] X. Li, W. Cai, L. Colombo, and R. S. Ruoff, "Evolution of Graphene Growth on Ni and Cu by Carbon Isotope Labeling," *Nano Lett.*, vol. 9, no. 12, pp. 4268–4272, Dec. 2009.
[28] A. Reina, X. Jia, J. Ho, D. Nezich, H. Son, V. Bulovic, M. S. Dresselhaus, and J. Kong, "Large Area, Few-Layer Graphene Films on Arbitrary Substrates by Chemical Vapor Deposition," *Nano Lett*, vol. 9, no. 1, pp. 30–35, Jan. 2009.
[29] X. Li, W. Cai, J. An, S. Kim, J. Nah, D. Yang, R. Piner, A. Velamakanni, I. Jung, E. Tutuc, S. K. Banerjee, L. Colombo, and R. S. Ruoff, "Large-Area

Synthesis of High-Quality and Uniform Graphene Films on Copper Foils," *Science*, vol. 324, no. 5932, pp. 1312–1314, Jun. 2009.
[30] Q. Yu, J. Lian, S. Siriponglert, H. Li, Y. P. Chen, and S.-S. Pei, "Graphene segregated on Ni surfaces and transferred to insulators," *Appl. Phys. Lett.*, vol. 93, no. 11, pp. 113103–113103–3, Sep. 2008.
[31] V. M. Karpan, P. A. Khomyakov, G. Giovannetti, A. A. Starikov, and P. J. Kelly, "Ni(111)vertical bar graphene vertical bar h-BN junctions as ideal spin injectors," *Phys. Rev. B*, vol. 84, no. 15, Oct. 2011.
[32] Y. S. Dedkov, M. Fonin, U. Rüdiger, and C. Laubschat, "Rashba Effect in the Graphene/Ni(111) System," *Phys. Rev. Lett.*, vol. 100, no. 10, p. 107602, Mar. 2008.
[33] V. M. Karpan, G. Giovannetti, P. A. Khomyakov, M. Talanana, A. A. Starikov, M. Zwierzycki, J. van den Brink, G. Brocks, and P. J. Kelly, "Graphite and Graphene as Perfect Spin Filters," *Phys. Rev. Lett.*, vol. 99, no. 17, p. 176602, Oct. 2007.
[34] L. M. Malard, M. A. Pimenta, G. Dresselhaus, and M. S. Dresselhaus, "Raman spectroscopy in graphene," vol. 473, no. 5–6, pp. 51–87, Apr. 2009.
[35] C. Faugeras, A. Nerrière, M. Potemski, A. Mahmood, E. Dujardin, C. Berger, and W. A. de Heer, "Few-layer graphene on SiC, pyrolitic graphite, and graphene: A Raman scattering study," *Appl. Phys. Lett.*, vol. 92, no. 1, p. 011914, 2008.
[36] D. R. Lenski and M. S. Fuhrer, "Raman and optical characterization of multilayer turbostratic graphene grown via chemical vapor deposition," vol. 110, no. 1, pp. 013720–013720–4, Jul. 2011.
[37] A. Luican, G. Li, A. Reina, J. Kong, R. R. Nair, K. S. Novoselov, A. K. Geim, and E. Y. Andrei, "Single-Layer Behavior and Its Breakdown in Twisted Graphene Layers," *Phys. Rev. Lett.*, vol. 106, no. 12, p. 126802, Mar. 2011.
[38] T. Osada, "Negative Interlayer Magnetoresistance and Zero-Mode Landau Level in Multilayer Dirac Electron Systems," vol. 77, no. 8, p. 084711, 2008.
[39] N. Tajima, S. Sugawara, R. Kato, Y. Nishio, and K. Kajita, "Effect of the Zero-Mode Landau Level on Interlayer Magnetoresistance in Multilayer Massless Dirac Fermion Systems," *Phys Rev Lett*, vol. 102, no. 17, p. 176403, Apr. 2009.
[40] S. Das Sarma, S. Adam, E. H. Hwang, and E. Rossi, "Electronic transport in two-dimensional graphene," *Rev. Mod. Phys.*, vol. 83, no. 2, pp. 407–470, May 2011.
[41] J.-C. Charlier and S. Roche, "Electronic and transport properties of nanotubes," *Rev. Mod. Phys.*, vol. 79, no. 2, pp. 677–732, May 2007.
[42] P. R. Wallace, "The Band Theory of Graphite," *Phys. Rev.*, vol. 71, no. 9, pp. 622–634, May 1947.
[43] K. S. Novoselov, Z. Jiang, Y. Zhang, S. V. Morozov, H. L. Stormer, U. Zeitler, J. C. Maan, G. S. Boebinger, P. Kim, and A. K. Geim, "Room-Temperature Quantum Hall Effect in Graphene," *Science*, vol. 315, no. 5817, pp. 1379–1379, Mar. 2007.

[44] A. H. Castro Neto, F. Guinea, N. M. R. Peres, K. S. Novoselov, and A. K. Geim, "The electronic properties of graphene," *Rev. Mod. Phys.*, vol. 81, no. 1, p. 109, Jan. 2009.
[45] S. Bandyopadhyay, *Physics of nanostructured solid state devices*. New York, N.Y: Springer, 2012.
[46] A. Yacoby, "Graphene: Tri and tri again," *Nat. Phys.*, vol. 7, no. 12, pp. 925–926, Dec. 2011.
[47] C. H. Lui, Z. Li, Z. Chen, P. V. Klimov, L. E. Brus, and T. F. Heinz, "Imaging Stacking Order in Few-Layer Graphene," *Nano Lett.*, vol. 11, no. 1, pp. 164–169, Jan. 2011.
[48] Z. Liu, K. Suenaga, P. J. F. Harris, and S. Iijima, "Open and Closed Edges of Graphene Layers," *Phys. Rev. Lett.*, vol. 102, no. 1, p. 015501, Jan. 2009.
[49] J. Hass, F. Varchon, J. E. Millán-Otoya, M. Sprinkle, N. Sharma, W. A. de Heer, C. Berger, P. N. First, L. Magaud, and E. H. Conrad, "Why Multilayer Graphene on 4H-SiC(0001) Behaves Like a Single Sheet of Graphene," *Phys. Rev. Lett.*, vol. 100, no. 12, p. 125504, Mar. 2008.
[50] S. Shallcross, S. Sharma, E. Kandelaki, and O. A. Pankratov, "Electronic structure of turbostratic graphene," *Phys. Rev. B*, vol. 81, no. 16, p. 165105, Apr. 2010.
[51] J.-J. Chen, J. Meng, Y.-B. Zhou, H.-C. Wu, Y.-Q. Bie, Z.-M. Liao, and D.-P. Yu, "Layer-by-layer assembly of vertically conducting graphene devices," *Nat. Commun.*, vol. 4, May 2013.
[52] A. L. Friedman, J. L. Tedesco, P. M. Campbell, J. C. Culbertson, E. Aifer, F. K. Perkins, R. L. Myers-Ward, J. K. Hite, C. R. Eddy, G. G. Jernigan, and D. K. Gaskill, "Quantum Linear Magnetoresistance in Multilayer Epitaxial Graphene," *Nano Lett*, vol. 10, no. 10, pp. 3962–3965, Oct. 2010.
[53] A. A. Abrikosov, "Quantum linear magnetoresistance," *EPL Europhys. Lett.*, vol. 49, no. 6, p. 789, Mar. 2000.
[54] D. V. Khveshchenko, "Ghost Excitonic Insulator Transition in Layered Graphite," *Phys. Rev. Lett.*, vol. 87, no. 24, p. 246802, Nov. 2001.
[55] E. McCann, K. Kechedzhi, V. I. Fal'ko, H. Suzuura, T. Ando, and B. L. Altshuler, "Weak-Localization Magnetoresistance and Valley Symmetry in Graphene," *Phys. Rev. Lett.*, vol. 97, no. 14, p. 146805, Oct. 2006.
[56] Q. Yu, L. A. Jauregui, W. Wu, R. Colby, J. Tian, Z. Su, H. Cao, Z. Liu, D. Pandey, D. Wei, T. F. Chung, P. Peng, N. P. Guisinger, E. A. Stach, J. Bao, S.-S. Pei, and Y. P. Chen, "Control and characterization of individual grains and grain boundaries in graphene grown by chemical vapour deposition," *Nat. Mater.*, vol. 10, no. 6, pp. 443–449, Jun. 2011.
[57] J. Hu and T. F. Rosenbaum, "Classical and quantum routes to linear magnetoresistance," *Nat. Mater.*, vol. 7, no. 9, pp. 697–700, 2008.
[58] M. M. Parish and P. B. Littlewood, "Non-saturating magnetoresistance in heavily disordered semiconductors," *Nature*, vol. 426, no. 6963, pp. 162–165, Nov. 2003.
[59] A. A. Abrikosov, "Quantum magnetoresistance of layered semimetals," *Phys. Rev. B*, vol. 60, no. 6, pp. 4231–4234, Aug. 1999.

[60] D. V. Khveshchenko, “Magnetic-Field-Induced Insulating Behavior in Highly Oriented Pyrolitic Graphite,” *Phys. Rev. Lett.*, vol. 87, no. 20, p. 206401, Oct. 2001.
[61] T. Morinari and T. Tohyama, “Crossover from Positive to Negative Interlayer Magnetoresistance in Multilayer Massless Dirac Fermion System with Non-Vertical Interlayer Tunneling,” vol. 79, no. 4, p. 044708, 2010.
[62] N. Tajima, M. Sato, S. Sugawara, R. Kato, Y. Nishio, and K. Kajita, “Spin and valley splittings in multilayered massless Dirac fermion system,” *Phys Rev B*, vol. 82, no. 12, p. 121420, Sep. 2010.
[63] A. A. Bright, “Negative magnetoresistance in pregraphitic carbons,” *Carbon*, vol. 17, no. 3, pp. 259–263, 1979.
[64] A. K. Geim and K. S. Novoselov, “The rise of graphene,” *Nat Mater*, vol. 6, no. 3, pp. 183–191, Mar. 2007.
[65] K. S. Kim, Y. Zhao, H. Jang, S. Y. Lee, J. M. Kim, K. S. Kim, J.-H. Ahn, P. Kim, J.-Y. Choi, and B. H. Hong, “Large-scale pattern growth of graphene films for stretchable transparent electrodes,” *Nature*, vol. 457, no. 7230, pp. 706–710, Feb. 2009.
[66] Y. Zhang, L. Gomez, F. N. Ishikawa, A. Madaria, K. Ryu, C. Wang, A. Badmaev, and C. Zhou, “Comparison of Graphene Growth on Single-Crystalline and Polycrystalline Ni by Chemical Vapor Deposition,” *J. Phys. Chem. Lett.*, vol. 1, no. 20, pp. 3101–3107, Oct. 2010.
[67] C. Berger, Z. Song, T. Li, X. Li, A. Y. Ogbazghi, R. Feng, Z. Dai, A. N. Marchenkov, E. H. Conrad, P. N. First, and W. A. de Heer, “Ultrathin Epitaxial Graphite: 2D Electron Gas Properties and a Route toward Graphene-based Nanoelectronics,” *J. Phys. Chem. B*, vol. 108, no. 52, pp. 19912–19916, Dec. 2004.
[68] Y.-M. Lin, C. Dimitrakopoulos, K. A. Jenkins, D. B. Farmer, H.-Y. Chiu, A. Grill, and P. Avouris, “100-GHz Transistors from Wafer-Scale Epitaxial Graphene,” *Science*, vol. 327, no. 5966, p. 662, Feb. 2010.
[69] Y. Gamo, A. Nagashima, M. Wakabayashi, M. Terai, and C. Oshima, “Atomic structure of monolayer graphite formed on Ni(111),” *Surf. Sci.*, vol. 374, no. 1–3, pp. 61–64, Mar. 1997.
[70] R. Addou, A. Dahal, P. Sutter, and M. Batzill, “Monolayer graphene growth on Ni(111) by low temperature chemical vapor deposition,” *Appl. Phys. Lett.*, vol. 100, no. 2, Jan. 2012.
[71] G. A. López and E. J. Mittemeijer, “The solubility of C in solid Cu,” *Scr. Mater.*, vol. 51, no. 1, pp. 1–5, Jul. 2004.
[72] C. V. Raman and K. S. Krishnan, “A new type of secondary radiation,” *Nature*, vol. 121, pp. 501–502, Jun. 1928.
[73] M. A. Pimenta, G. Dresselhaus, M. S. Dresselhaus, L. G. Cancado, A. Jorio, and R. Saito, “Studying disorder in graphite-based systems by Raman spectroscopy,” *Phys. Chem. Chem. Phys.*, vol. 9, no. 11, pp. 1276–1290, Mar. 2007.
[74] A. C. Ferrari and D. M. Basko, “Raman spectroscopy as a versatile tool for studying the properties of graphene,” *Nat. Nanotechnol.*, vol. 8, no. 4, pp. 235–246, Apr. 2013.

[75] J. R. Ferraro, K. Nakamoto, and C. W. Brown, “Chapter 1 - Basic Theory,” in *Introductory Raman Spectroscopy (Second Edition)*, J. R. Ferraro, K. Nakamoto, and C. W. Brown, Eds. San Diego: Academic Press, 2003, pp. 1–94.
[76] C. Casiraghi, A. Hartschuh, E. Lidorikis, H. Qian, H. Harutyunyan, T. Gokus, K. S. Novoselov, and A. C. Ferrari, “Rayleigh Imaging of Graphene and Graphene Layers,” *Nano Lett.*, vol. 7, no. 9, pp. 2711–2717, Sep. 2007.
[77] J. W. Suk, W. H. Lee, J. Lee, H. Chou, R. D. Piner, Y. Hao, D. Akinwande, and R. S. Ruoff, “Enhancement of the Electrical Properties of Graphene Grown by Chemical Vapor Deposition via Controlling the Effects of Polymer Residue,” *Nano Lett.*, vol. 13, no. 4, pp. 1462–1467, Apr. 2013.
[78] M. Her, R. Beams, and L. Novotny, “Graphene transfer with reduced residue,” *Phys. Lett. A*, vol. 377, no. 21–22, pp. 1455–1458, Sep. 2013.
[79] K. Sato, J. S. Park, R. Saito, C. Cong, T. Yu, C. H. Lui, T. F. Heinz, G. Dresselhaus, and M. S. Dresselhaus, “Raman spectra of out-of-plane phonons in bilayer graphene,” *Phys. Rev. B*, vol. 84, no. 3, p. 035419, Jul. 2011.
[80] R. Rao, R. Podila, R. Tsuchikawa, J. Katoch, D. Tishler, A. M. Rao, and M. Ishigami, “Effects of Layer Stacking on the Combination Raman Modes in Graphene,” *ACS Nano*, vol. 5, no. 3, pp. 1594–1599, Mar. 2011.
[81] R. Saito, M. Hofmann, G. Dresselhaus, A. Jorio, and M. S. Dresselhaus, “Raman spectroscopy of graphene and carbon nanotubes,” *Adv. Phys.*, vol. 60, no. 3, pp. 413–550, 2011.
[82] C. Thomsen and S. Reich, “Double Resonant Raman Scattering in Graphite,” *Phys. Rev. Lett.*, vol. 85, no. 24, pp. 5214–5217, Dec. 2000.
[83] A. C. Ferrari, J. C. Meyer, V. Scardaci, C. Casiraghi, M. Lazzeri, F. Mauri, S. Piscanec, D. Jiang, K. S. Novoselov, S. Roth, and A. K. Geim, “Raman Spectrum of Graphene and Graphene Layers,” *Phys. Rev. Lett.*, vol. 97, no. 18, p. 187401, Oct. 2006.
[84] Z. Ni, Y. Wang, T. Yu, and Z. Shen, “Raman spectroscopy and imaging of graphene,” *Nano Res.*, vol. 1, no. 4, pp. 273–291, Oct. 2008.
[85] J. Wintterlin and M.-L. Bocquet, “Graphene on metal surfaces,” vol. 603, no. 10–12, pp. 1841–1852, Jun. 2009.
[86] C. Gong, G. Lee, B. Shan, E. M. Vogel, R. M. Wallace, and K. Cho, “First-principles study of metal–graphene interfaces,” *J. Appl. Phys.*, vol. 108, no. 12, pp. 123711–123711–8, Dec. 2010.
[87] G. Giovannetti, P. A. Khomyakov, G. Brocks, V. M. Karpan, J. van den Brink, and P. J. Kelly, “Doping Graphene with Metal Contacts,” *Phys. Rev. Lett.*, vol. 101, no. 2, p. 026803, Jul. 2008.
[88] Z. Xu and M. J. Buehler, “Interface structure and mechanics between graphene and metal substrates: a first-principles study,” *J. Phys. Condens. Matter*, vol. 22, no. 48, p. 485301, Dec. 2010.
[89] R. Nouchi, M. Shiraishi, and Y. Suzuki, “Transfer characteristics in graphene field-effect transistors with Co contacts,” *Appl. Phys. Lett.*, vol. 93, no. 15, pp. 152104–152104–3, 2008.
[90] N. Park, B.-K. Kim, J.-O. Lee, and J.-J. Kim, “Influence of metal work function on the position of the Dirac point of graphene field-effect

transistors," *Appl. Phys. Lett.*, vol. 95, no. 24, pp. 243105–243105–3, Dec. 2009.
[91] L. V. Dzemiantsova, M. Karolak, F. Lofink, A. Kubetzka, B. Sachs, K. von Bergmann, S. Hankemeier, T. O. Wehling, R. Frömter, H. P. Oepen, A. I. Lichtenstein, and R. Wiesendanger, "Multiscale magnetic study of Ni(111) and graphene on Ni(111)," *Phys. Rev. B*, vol. 84, no. 20, p. 205431, Nov. 2011.
[92] V. M. Karpan, P. A. Khomyakov, A. A. Starikov, G. Giovannetti, M. Zwierzycki, M. Talanana, G. Brocks, J. van den Brink, and P. J. Kelly, "Theoretical prediction of perfect spin filtering at interfaces between close-packed surfaces of Ni or Co and graphite or graphene," *Phys. Rev. B*, vol. 78, no. 19, p. 195419, Nov. 2008.
[93] S. J. Gong, Z. Y. Li, Z. Q. Yang, C. Gong, C.-G. Duan, and J. H. Chu, "Spintronic properties of graphene films grown on Ni(111) substrate," *J. Appl. Phys.*, vol. 110, no. 4, p. 043704, Aug. 2011.
[94] B. R. Matis, F. A. Bulat, A. L. Friedman, B. H. Houston, and J. W. Baldwin, "Giant negative magnetoresistance and a transition from strong to weak localization in hydrogenated graphene," *Phys. Rev. B*, vol. 85, no. 19, p. 195437, May 2012.
[95] S. J. Chae, F. Güneş, K. K. Kim, E. S. Kim, G. H. Han, S. M. Kim, H.-J. Shin, S.-M. Yoon, J.-Y. Choi, M. H. Park, C. W. Yang, D. Pribat, and Y. H. Lee, "Synthesis of Large-Area Graphene Layers on Poly-Nickel Substrate by Chemical Vapor Deposition: Wrinkle Formation," *Adv. Mater.*, vol. 21, no. 22, pp. 2328–2333, 2009.
[96] S. C. Bodepudi, A. P. Singh, and S. Pramanik, "Giant Current-Perpendicular-to-Plane Magnetoresistance in Multilayer-Graphene As-Grown on Nickel," *Nano Lett.*, Apr. 2014.
[97] S. C. Bodepudi, A. P. Singh, and S. Pramanik, "Current-Perpendicular-to-Plane Magnetoresistance in Chemical Vapor Deposition-Grown Multilayer Graphene," *Electronics*, vol. 2, no. 3, pp. 315–331, Sep. 2013.
[98] S. C. Bodepudi, X. Wang, and S. Pramanik, "Angle dependent interlayer magnetoresistance in multilayer graphene stacks," *J. Appl. Phys.*, vol. 118, no. 16, p. 164303, Oct. 2015.
[99] S. C. Bodepudi, X. Wang, A. P. Singh, and S. Pramanik, "Thickness Dependent Interlayer Magnetoresistance (ILMR) in Multilayer Graphene Stacks," *Submitt. Carbon CARBON--15-02297*.
[100] S. C. Bodepudi, Abhay Singh, and S. Pramanik, "Magnetoresistance Effects in Multilayer Graphene As Grown on Ferromagnetic Substrates and Implications for Spin Filtering," in *Proceedings of the 14th IEEE International Conference on Nanotechnology*, Toronto, 2014, vol. 14th IEEE-Nano.
[101] A. Grüneis, "Synthesis and electronic properties of chemically functionalized graphene on metal surfaces," *J. Phys. Condens. Matter*, vol. 25, no. 4, p. 043001, Jan. 2013.
[102] A. Charrier, A. Coati, T. Argunova, F. Thibaudau, Y. Garreau, R. Pinchaux, I. Forbeaux, J.-M. Debever, M. Sauvage-Simkin, and J.-M. Themlin, "Solid-

state decomposition of silicon carbide for growing ultra-thin heteroepitaxial graphite films," *J. Appl. Phys.*, vol. 92, no. 5, pp. 2479–2484, Aug. 2002.
[103] A. N. Hattori, T. Okamoto, S. Sadakuni, J. Murata, K. Arima, Y. Sano, K. Hattori, H. Daimon, K. Endo, and K. Yamauchi, "Formation of wide and atomically flat graphene layers on ultraprecision-figured 4H-SiC(0001) surfaces," *Surf. Sci.*, vol. 605, no. 5–6, pp. 597–605, Mar. 2011.
[104] S. Unarunotai, Y. Murata, C. E. Chialvo, H. Kim, S. MacLaren, N. Mason, I. Petrov, and J. A. Rogers, "Transfer of graphene layers grown on SiC wafers to other substrates and their integration into field effect transistors," *Appl. Phys. Lett.*, vol. 95, no. 20, p. 202101, Nov. 2009.
[105] D. S. Lee, C. Riedl, B. Krauss, K. von Klitzing, U. Starke, and J. H. Smet, "Raman Spectra of Epitaxial Graphene on SiC and of Epitaxial Graphene Transferred to SiO2," *Nano Lett.*, vol. 8, no. 12, pp. 4320–4325, Dec. 2008.
[106] J. D. Caldwell, T. J. Anderson, J. C. Culbertson, G. G. Jernigan, K. D. Hobart, F. J. Kub, M. J. Tadjer, J. L. Tedesco, J. K. Hite, M. A. Mastro, R. L. Myers-Ward, C. R. Eddy, P. M. Campbell, and D. K. Gaskill, "Technique for the Dry Transfer of Epitaxial Graphene onto Arbitrary Substrates," *ACS Nano*, vol. 4, no. 2, pp. 1108–1114, Feb. 2010.
[107] M. Acik and Y. J. Chabal, "Nature of Graphene Edges: A Review," *Jpn. J. Appl. Phys.*, vol. 50, no. 7, p. 070101, 2011.
[108] J. Lahiri, Y. Lin, P. Bozkurt, I. I. Oleynik, and M. Batzill, "An extended defect in graphene as a metallic wire," *Nat. Nanotechnol.*, vol. 5, no. 5, pp. 326–329, May 2010.
[109] A. Pirkle, J. Chan, A. Venugopal, D. Hinojos, C. W. Magnuson, S. McDonnell, L. Colombo, E. M. Vogel, R. S. Ruoff, and R. M. Wallace, "The effect of chemical residues on the physical and electrical properties of chemical vapor deposited graphene transferred to SiO2," *Appl. Phys. Lett.*, vol. 99, no. 12, p. 122108, Sep. 2011.
[110] Z. Cheng, Q. Zhou, C. Wang, Q. Li, C. Wang, and Y. Fang, "Toward Intrinsic Graphene Surfaces: A Systematic Study on Thermal Annealing and Wet-Chemical Treatment of SiO2-Supported Graphene Devices," *Nano Lett.*, vol. 11, no. 2, pp. 767–771, Feb. 2011.
[111] Y.-C. Lin, C.-C. Lu, C.-H. Yeh, C. Jin, K. Suenaga, and P.-W. Chiu, "Graphene Annealing: How Clean Can It Be?," *Nano Lett.*, vol. 12, no. 1, pp. 414–419, Jan. 2012.
[112] M. R. Ammar, J. N. Rouzaud, C. E. Vaudey, N. Toulhoat, and N. Moncoffre, "Characterization of graphite implanted with chlorine ions using combined Raman microspectrometry and transmission electron microscopy on thin sections prepared by focused ion beam," *Carbon*, vol. 48, no. 4, pp. 1244–1251, Apr. 2010.
[113] P. Blake, E. W. Hill, A. H. C. Neto, K. S. Novoselov, D. Jiang, R. Yang, T. J. Booth, and A. K. Geim, "Making graphene visible," *Appl. Phys. Lett.*, vol. 91, no. 6, p. 063124, Aug. 2007.
[114] X. Wang, Y. P. Chen, and D. D. Nolte, "Strong anomalous optical dispersion of graphene: complex refractive index measured by Picometrology," *Opt. Express*, vol. 16, no. 26, pp. 22105–22112, Dec. 2008.

[115] L. G. Cançado, K. Takai, T. Enoki, M. Endo, Y. A. Kim, H. Mizusaki, N. L. Speziali, A. Jorio, and M. A. Pimenta, "Measuring the degree of stacking order in graphite by Raman spectroscopy," *Carbon*, vol. 46, no. 2, pp. 272–275, Feb. 2008.
[116] K. Matsubara, K. Sugihara, and T. Tsuzuku, "Electrical resistance in the c direction of graphite," *Phys Rev B*, vol. 41, no. 2, pp. 969–974, Jan. 1990.
[117] G. Venugopal, M.-H. Jung, M. Suemitsu, and S.-J. Kim, "Fabrication of nanoscale three-dimensional graphite stacked-junctions by focused-ion-beam and observation of anomalous transport characteristics," *Carbon*, vol. 49, no. 8, pp. 2766–2772, Jul. 2011.
[118] J. Heo, H. J. Chung, S.-H. Lee, H. Yang, D. H. Seo, J. K. Shin, U.-I. Chung, S. Seo, E. H. Hwang, and S. Das Sarma, "Nonmonotonic temperature dependent transport in graphene grown by chemical vapor deposition," *Phys. Rev. B*, vol. 84, no. 3, p. 035421, Jul. 2011.
[119] J. B. Oostinga, B. Sacépé, M. F. Craciun, and A. F. Morpurgo, "Magnetotransport through graphene nanoribbons," *Phys. Rev. B*, vol. 81, no. 19, p. 193408, May 2010.
[120] J.-M. Poumirol, A. Cresti, S. Roche, W. Escoffier, M. Goiran, X. Wang, X. Li, H. Dai, and B. Raquet, "Edge magnetotransport fingerprints in disordered graphene nanoribbons," *Phys. Rev. B*, vol. 82, no. 4, p. 041413, Jul. 2010.
[121] J. Bai, R. Cheng, F. Xiu, L. Liao, M. Wang, A. Shailos, K. L. Wang, Y. Huang, and X. Duan, "Very large magnetoresistance in graphene nanoribbons," *Nat Nano*, vol. 5, no. 9, pp. 655–659, 2010.
[122] Z. Wang, Z. Zhang, H. Xu, L. Ding, S. Wang, and L.-M. Peng, "A high-performance top-gate graphene field-effect transistor based frequency doubler," *Appl. Phys. Lett.*, vol. 96, no. 17, p. 173104, 2010.
[123] "Flexible graphene-based chemical sensors on paper substrates - Physical Chemistry Chemical Physics (RSC Publishing)," *Phys. Chem. Chem. Phys.*
[124] T. Shen, W. Wu, Q. Yu, C. A. Richter, R. Elmquist, D. Newell, and Y. P. Chen, "Quantum Hall effect on centimeter scale chemical vapor deposited graphene films," *Appl. Phys. Lett.*, vol. 99, no. 23, p. 232110, Dec. 2011.
[125] A. J. M. Giesbers, L. A. Ponomarenko, K. S. Novoselov, A. K. Geim, M. I. Katsnelson, J. C. Maan, and U. Zeitler, "Gap opening in the zeroth Landau level of graphene," *Phys. Rev. B*, vol. 80, no. 20, p. 201403, Nov. 2009.
[126] R. R. Haering and P. R. Wallace, "The electric and magnetic properties of graphite," vol. 3, no. 3–4, pp. 253–274, 1957.
[127] N. Levy, S. A. Burke, K. L. Meaker, M. Panlasigui, A. Zettl, F. Guinea, A. H. C. Neto, and M. F. Crommie, "Strain-Induced Pseudo–Magnetic Fields Greater Than 300 Tesla in Graphene Nanobubbles," *Science*, vol. 329, no. 5991, pp. 544 –547, Jul. 2010.
[128] W.-Y. He, Y. Su, M. Yang, and L. He, "Creating in-plane pseudomagnetic fields in excess of 1000 T by misoriented stacking in a graphene bilayer," *Phys. Rev. B*, vol. 89, no. 12, p. 125418, Mar. 2014.
[129] F. Guinea, A. H. Castro Neto, and N. M. R. Peres, "Electronic states and Landau levels in graphene stacks," *Phys. Rev. B*, vol. 73, no. 24, p. 245426, Jun. 2006.

[130] K. S. Novoselov, D. Jiang, F. Schedin, T. J. Booth, V. V. Khotkevich, S. V. Morozov, and A. K. Geim, "Two-dimensional atomic crystals," *Proc. Natl. Acad. Sci. U. S. A.*, vol. 102, no. 30, pp. 10451–10453, Jul. 2005.
[131] Y. Zhang, Y.-W. Tan, H. L. Stormer, and P. Kim, "Experimental observation of the quantum Hall effect and Berry's phase in graphene," *Nature*, vol. 438, no. 7065, pp. 201–204, Nov. 2005.
[132] M. L. Sadowski, G. Martinez, M. Potemski, C. Berger, and W. A. de Heer, "Landau Level Spectroscopy of Ultrathin Graphite Layers," *Phys. Rev. Lett.*, vol. 97, no. 26, p. 266405, Dec. 2006.
[133] S. Latil, V. Meunier, and L. Henrard, "Massless fermions in multilayer graphitic systems with misoriented layers: Ab initio calculations and experimental fingerprints," *Phys. Rev. B*, vol. 76, no. 20, p. 201402, Nov. 2007.
[134] K. Kanzaki, H. Hibino, and T. Makimoto, "Graphene Layer Formation on Polycrystalline Nickel Grown by Chemical Vapor Deposition," *Jpn. J. Appl. Phys.*, vol. 52, no. 3R, p. 035103, Mar. 2013.
[135] L. Baraton, Z. B. He, C. S. Lee, C. S. Cojocaru, M. Châtelet, J.-L. Maurice, Y. H. Lee, and D. Pribat, "On the mechanisms of precipitation of graphene on nickel thin films," *EPL Europhys. Lett.*, vol. 96, no. 4, p. 46003, Nov. 2011.
[136] E. O. Polat, O. Balcı, and C. Kocabas, "Graphene based flexible electrochromic devices," *Sci. Rep.*, vol. 4, Oct. 2014.
[137] L. Gomez De Arco, Y. Zhang, C. W. Schlenker, K. Ryu, M. E. Thompson, and C. Zhou, "Continuous, Highly Flexible, and Transparent Graphene Films by Chemical Vapor Deposition for Organic Photovoltaics," *ACS Nano*, vol. 4, no. 5, pp. 2865–2873, May 2010.
[138] G. Lupina, J. Kitzmann, I. Costina, M. Lukosius, C. Wenger, A. Wolff, S. Vaziri, M. Östling, I. Pasternak, A. Krajewska, W. Strupinski, S. Kataria, A. Gahoi, M. C. Lemme, G. Ruhl, G. Zoth, O. Luxenhofer, and W. Mehr, "Residual metallic contamination of transferred chemical vapor deposited graphene," *ACS Nano*, vol. 9, no. 5, pp. 4776–4785, May 2015.
[139] N. US Department of Commerce, "Hall Effect Measurements Resistivity." [Online]. Available: http://www.nist.gov/pml/div683/hall_resistivity.cfm. [Accessed: 28-Sep-2015].
[140] S. Datta, *Electronic Transport in Mesoscopic Systems*. Cambridge: Cambridge University Press, 1995.
[141] D. E. Soule, J. W. McClure, and L. B. Smith, "Study of the Shubnikov-de Haas Effect. Determination of the Fermi Surfaces in Graphite," *Phys. Rev.*, vol. 134, no. 2A, pp. A453–A470, Apr. 1964.
[142] R. F. Pires, P. Pureur, M. Behar, J. L. P. Jr, J. Schaf, and Y. Kopelevich, "Magnetism, magnetoresistance, and Shubnikov-de Haas oscillations in Na-implanted highly oriented pyrolitic graphite," *J. Appl. Phys.*, vol. 111, no. 9, p. 093922, May 2012.
[143] X. C. Yang, H. M. Wang, T. R. Wu, F. Q. Huang, J. Chen, X. X. Kang, Z. Jin, X. M. Xie, and M. H. Jiang, "Magnetotransport of polycrystalline graphene: Shubnikov-de Haas oscillation and weak localization study," *Appl. Phys. Lett.*, vol. 102, no. 23, p. 233503, Jun. 2013.

[144] E. H. Hwang and S. Das Sarma, "Screening-induced temperature-dependent transport in two-dimensional graphene," *Phys. Rev. B*, vol. 79, no. 16, p. 165404, Apr. 2009.
[145] J. E. Lenz, "A review of magnetic sensors," *Proc. IEEE*, vol. 78, no. 6, pp. 973–989, Jun. 1990.
[146] G. A. Prinz, "Magnetoelectronics," *Science*, vol. 282, no. 5394, pp. 1660–1663, Nov. 1998.
[147] E. Y. Tsymbal, O. N. Mryasov, and P. R. LeClair, "Spin-dependent tunnelling in magnetic tunnel junctions," *J. Phys. Condens. Matter*, vol. 15, no. 4, p. R109, Feb. 2003.
[148] S. Bandyopadhyay and M. Cahay, "Electron spin for classical information processing: a brief survey of spin-based logic devices, gates and circuits," *Nanotechnology*, vol. 20, no. 41, p. 412001, Oct. 2009.
[149] Tomoyasu Taniyama, Eiji Wada, Mitsuru Itoh, and Masahito Yamaguchi, "Electrical and optical spin injection in ferromagnet/semiconductor heterostructures," *NPG Asia Mater.*, vol. 3, no. 7, pp. 65–73, Jul. 2011.
[150] S. Schmaus, A. Bagrets, Y. Nahas, T. K. Yamada, A. Bork, M. Bowen, E. Beaurepaire, F. Evers, and W. Wulfhekel, "Giant magnetoresistance through a single molecule," *Nat. Nanotechnol.*, vol. 6, no. 3, pp. 185–189, 2011.
[151] T. Banerjee, W. G. van der Wiel, and R. Jansen, "Spin injection and perpendicular spin transport in graphite nanostructures," *Phys. Rev. B*, vol. 81, no. 21, p. 214409, Jun. 2010.
[152] D. Pacilé, P. Leicht, M. Papagno, P. M. Sheverdyaeva, P. Moras, C. Carbone, K. Krausert, L. Zielke, M. Fonin, Y. S. Dedkov, F. Mittendorfer, J. Doppler, A. Garhofer, and J. Redinger, "Artificially lattice-mismatched graphene/metal interface: Graphene/Ni/Ir(111)," *Phys. Rev. B*, vol. 87, no. 3, p. 035420, Jan. 2013.
[153] N. R. Gall, E. V. Rut'kov, and A. Y. Tontegode, "Intercalation of nickel atoms under two-dimensional graphene film on (111)Ir," *Carbon*, vol. 38, no. 5, pp. 663–667, 2000.
[154] M. M. Lucchese, F. Stavale, E. H. M. Ferreira, C. Vilani, M. V. O. Moutinho, R. B. Capaz, C. A. Achete, and A. Jorio, "Quantifying ion-induced defects and Raman relaxation length in graphene," *Carbon*, vol. 48, no. 5, pp. 1592–1597, Apr. 2010.
[155] Y. S. Dedkov and M. Fonin, "Electronic and magnetic properties of the graphene-ferromagnet interface," *New J. Phys.*, vol. 12, Dec. 2010.
[156] D. C. Elias, R. R. Nair, T. M. G. Mohiuddin, S. V. Morozov, P. Blake, M. P. Halsall, A. C. Ferrari, D. W. Boukhvalov, M. I. Katsnelson, A. K. Geim, and K. S. Novoselov, "Control of Graphene's Properties by Reversible Hydrogenation: Evidence for Graphane," *Science*, vol. 323, no. 5914, pp. 610–613, Jan. 2009.
[157] X. Hong, S.-H. Cheng, C. Herding, and J. Zhu, "Colossal negative magnetoresistance in dilute fluorinated graphene," *Phys. Rev. B*, vol. 83, no. 8, p. 085410, Feb. 2011.
[158] M. Papagno, P. Moras, P. M. Sheverdyaeva, J. Doppler, A. Garhofer, F. Mittendorfer, J. Redinger, and C. Carbone, "Hybridization of graphene and a

Ag monolayer supported on Re(0001)," *Phys. Rev. B*, vol. 88, no. 23, p. 235430, Dec. 2013.
[159] W. Li, Y. He, L. Wang, G. Ding, Z.-Q. Zhang, R. W. Lortz, P. Sheng, and N. Wang, "Electron localization in metal-decorated graphene," *Phys. Rev. B*, vol. 84, no. 4, p. 045431, Jul. 2011.
[160] J. Moser, H. Tao, S. Roche, F. Alzina, C. M. Sotomayor Torres, and A. Bachtold, "Magnetotransport in disordered graphene exposed to ozone: From weak to strong localization," *Phys. Rev. B*, vol. 81, no. 20, p. 205445, May 2010.
[161] N. K. Memon, S. D. Tse, M. Chhowalla, and B. H. Kear, "Role of substrate, temperature, and hydrogen on the flame synthesis of graphene films," *Proc. Combust. Inst.*, vol. 34, no. 2, pp. 2163–2170, 2013.
[162] R. S. Edwards and K. S. Coleman, "Graphene Film Growth on Polycrystalline Metals," *Acc. Chem. Res.*, vol. 46, no. 1, pp. 23–30, Jan. 2013.
[163] M. Zheng, K. Takei, B. Hsia, H. Fang, X. Zhang, N. Ferralis, H. Ko, Y.-L. Chueh, Y. Zhang, R. Maboudian, and A. Javey, "Metal-catalyzed crystallization of amorphous carbon to graphene," *Appl. Phys. Lett.*, vol. 96, no. 6, p. 063110, Feb. 2010.
[164] A. Grüneis and D. V. Vyalikh, "Tunable hybridization between electronic states of graphene and a metal surface," *Phys. Rev. B*, vol. 77, no. 19, p. 193401, May 2008.
[165] M. Gao, Y. Pan, C. Zhang, H. Hu, R. Yang, H. Lu, J. Cai, S. Du, F. Liu, and H.-J. Gao, "Tunable interfacial properties of epitaxial graphene on metal substrates," *Appl. Phys. Lett.*, vol. 96, no. 5, pp. 053109–053109–3, Feb. 2010.
[166] M. T. Johnson, H. I. Starnberg, and H. P. Hughes, "Electronic structure of alkali metal overlayers on graphite," *Surf. Sci.*, vol. 178, no. 1–3, pp. 290–299, Dec. 1986.
[167] Y. S. Dedkov, M. Fonin, and C. Laubschat, "A possible source of spin-polarized electrons: The inert graphene/Ni(111) system," *Appl. Phys. Lett.*, vol. 92, no. 5, p. 052506, Feb. 2008.
[168] D.-H. Kim and J. A. Rogers, "Stretchable Electronics: Materials Strategies and Devices," *Adv. Mater.*, vol. 20, no. 24, pp. 4887–4892, Dec. 2008.
[169] J. A. Rogers and Y. Huang, "A curvy, stretchy future for electronics," *Proc. Natl. Acad. Sci.*, vol. 106, no. 27, pp. 10875–10876, Jul. 2009.
[170] T. M. G. Mohiuddin, A. Lombardo, R. R. Nair, A. Bonetti, G. Savini, R. Jalil, N. Bonini, D. M. Basko, C. Galiotis, N. Marzari, K. S. Novoselov, A. K. Geim, and A. C. Ferrari, "Uniaxial strain in graphene by Raman spectroscopy: G peak splitting, Gruneisen parameters, and sample orientation," *Phys. Rev. B*, vol. 79, no. 20, p. 205433, May 2009.